BAlGaN-BASED VERTICAL CAVITY SURFACE-EMITTING LASERS OPERATING IN DEEP UV REGION

A Dissertation
Presented to
The Academic Faculty

By

Xin Li

In Partial Fulfillment
of the Requirements for the Degree
Doctor of Philosophy
in
Electrical and Computer Engineering

School of Electrical and Computer Engineering
Georgia Institute of Technology
August, 2016

BAlGaN-BASED VERTICAL CAVITY SURFACE-EMITTING LASERS OPERATING IN DEEP UV REGION

Approved by:

Dr. Abdallah Ougazzaden, Advisor
Professor, School of Electrical and Computer Engineering
Georgia Institute of Technology

Dr. David S Citrin
Professor, School of Electrical and Computer Engineering
Georgia Institute of Technology

Dr. Russell D Dupuis
Professor, School of Electrical and Computer Engineering
Georgia Institute of Technology

Dr. Surya R Kalidindi
Professor, The Georgia W. Woodruff School of Mechanical Engineering
Georgia Institute of Technology

Dr. Paul Douglas Yoder
Associate Professor, School of Electrical and Computer Engineering
Georgia Institute of Technology

Date Approved: April 6th, 2016

To my parents

To my husband

To my future kids

ACKNOWLEDGMENTS

I would like to begin by expressing my most sincere gratitude to my Ph.D. advisor, Prof. Abdallah Ougazzaden who brought me to this wonderful world of III nitrides. His patient guidance, enthusiasm for the research and encouraging support have led me to go through all the tough times during these years and to grow as a researcher. I am deeply grateful for him to give me the chance to participate in various projects, which enabled me to explore a wide range of topics in this field and to be more prepared for my future career.

I would like to thank Prof. Jean-Paul Salvestrini, Prof. Paul Voss and and Dr. Frédéric Genty for their kind support whenever I needed and for all the insightful discussions and suggestions they provided for my research work.

I would like to express my gratitude to the committee members for taking the time to read this thesis and for offering helpful comments and suggestions.

Financial support for this research was provided by ANR (Agence Nationale de la Recherche) in the framework of VESUVE project (ANR-11-BS03-0012). I would like to acknowledge all the partners involved in this project: Dr. Pierre Disseix, Dr. François Réveret, Dr. Joel Leymarie and Dr. Gaëlle LE GAC from Institut Pascal - Université Blaise-Pascal (LASMEA), Dr. Sophie Bouchoule and Dr. Gilles Patriarche from Laboratories de Photonique et de Nanostructures (LPN). I am very grateful for their contributions to this work and for their kind help and patient explanation whenever I have any doubts or questions. Special thanks are given to Prof. Russell D. Dupuis and his student Xiao-Hang Li from School of Electrical and Computer Engineering in Atlanta campus of Georgia Institute of Technology for their support on this project.

Sincere appreciation is extended to Dr. Suresh Sundaram, my colleague who spent almost every day with me in the growth lab. All the difficulties we have encountered and overcome, all those long days when we were sitting in front of the reactors and all the discussions which inspired me would be an unforgettable experience and a good memory.

I am also thankful for Dr. Tarik Moudakir who gave me a lot of help at the beginning of my PhD work. I would like to record my gratitude to the members in our lovely group: Youssef, Chris, Patrick, Jérémy, Yacine, Saiful, Taha, Matt, Muhammad, Peter, Renaud, Mélanie, and all other colleagues and friends in Georgia Tech Lorraine. It has been a real pleasure working with them. My thanks also go to my friends, Junliang Dong, Yang Wu and Xiaolong Wu for sharing my joy and sadness no matter for the life or for the research, and offering helps and supports whenever needed.

Lastly, I would like to give my most special thanks to my parents and my husband for their unconditional love and support. I would like to thank them for always believing in me and giving me a retreat and resting place, a haven against the tempest.

As the end, I would like to quote a sentence from the thesis of my husband who is a brilliant scientist and always inspires me with his passion for research:

"After all the confusion or epiphany, depression or inspiration, sadness or happiness, finally it comes to the stage when we are modest and grateful, as the last thing that I learned from my doctoral studies."

TABLE OF CONTENTS

LIST OF TABLES

LIST OF FIGURES

SUMMARY

The context of this thesis falls in the wide range of potential applications of UV light sources, such as high-density optical storage systems, sterilization and purification, UV spectroscopy, environmental control system and medical applications. However, the primary limitation of current UV light applications is the existing UV sources. The conventionally used sources include excimer lasers, Nd: YAG lasers or mercury lamps, but they are expensive, and have problems in efficiency, reliability and toxicity. In comparison, the semiconductor light-emitting devices are an ideal choice due to their reliability, compactness, high efficiency, minimum environmental effects and tunable operation wavelengths by changing the compositions. On the material aspect, III-nitride (BAlGaInN) semiconductors are promising candidates since they are chemically and physically stable with direct bandgaps covering from visible to deep UV (DUV) spectrum. On the structure aspect, vertical-cavity surface-emitting laser (VCSEL) is one of the most attractive configurations of semiconductor light-emitting devices considering its low threshold and high efficiency, and the possibility for the integration of 2D arrays and for the wafer-level tests as well. It constitutes a multiple-quantum-well (MQW) active region sandwiched by a top and a bottom distributed Bragg reflector (DBR). However, no VCSELs operating below 300 nm have been reported until now. The major challenges lie in the two main blocks of VCSEL structure: the emission efficiency of MQWs and the reflectivity of DBRs, which are limited by the quality of the substrates and epitaxial layers, optical-polarization properties of the MQW emission, small refractive index contrast of the layers used for DBRs at short wavelengths, doping difficulties and others.

The objective of this thesis is to address this need by studying metal-organic vapor phase epitaxy (MOVPE) growth of BAlGaN materials especially the novel BAlN material, developing AlGaN MQWs with enhanced TE-polarization (E$\perp$c) emission and exploring BAlN/AlGaN DBRs, for the future development of optical-pumped VCSELs operating in

the DUV region. The target wavelength is 280 nm here since it's widely used in the UV applications such as sterilization and water purification.

The thesis is outlined as follows.

Chapter 1 introduces the project background. The motivation including possible applications is stated. The research problems regarding different aspects are described. The state-of-the-art of semiconductor light-emitting devices and DBRs for DUV wavelengths is also summarized in this chapter.

Chapter 2 presents the basic properties of III-nitride materials as well as a brief introduction of the techniques and equipments used for the growth and characterizations. The growth is performed in home-built T-shape reactor unless specified. The new Aixtron 3×2 inch, close coupled showerhead (CCS) MOVPE system has also been brought into operation, and the substrate temperature can reach 1300 °C. The growth of AlN/sapphire templates has been initiated by using this reactor.

Chapter 3 goes into the MOVPE growth and studies of AlGaN and BAlN grown on AlN/sapphire templates. The first task is to have a careful control of the composition and the strain relaxation of AlGaN single layers to prepare for the MQW realization in the next step. The relationship between composition and strain state (composition pulling effect) is discussed. Different models are brought in to predict the range of critical thickness of AlGaN grown on AlN. The method to calculate screw/edge threading dislocation density of AlGaN and AlN layers from XRD measurements is also established. The second task is to explore novel BAlN material. MOVPE grown BAlN alloys with high boron incorporation (11~12%) have been achieved. The characteristics of BAlN with high boron content are analyzed. In order to improve the crystalline quality of BAlN, a method of low-temperature growth with annealing is proposed. The influences of growth temperature and TEB concentration in the precursors of III elements (TEB/III ratio) on the boron incorporation and on the crystalline quality are investigated. It is found that low temperature can alleviate

boron-rich phase poisoning during growth under high TEB/III ratio and improve the crystallinity. Very original results have been obtained showing that wurtzite BAlN layers grown by MOVPE have clear XRD peaks relating to 12% boron. The studies of the growth and characteristics of BAlN material can advance the application of MOVPE-grown boron alloys in bandgap, strain and refractive index engineering. The AlN/sapphire templates used for the experiments are from the group of Prof. Dupuis. In this chapter, additionally, the last section presents the preliminary results of AlN/sapphire template optimization in our new CCS reactor.

Chapter 4 is addressed to the AlGaN MQWs emitting at 280 nm. Firstly, 4-period $Al_{0.57}Ga_{0.43}N$ / $Al_{0.38}Ga_{0.62}N$ MQW structure has been grown on a relaxed $Al_{0.58}Ga_{0.42}N$ buffer on AlN/sapphire template. The compositions of the quantum wells have been optimized so that the strain present in wells is sufficient to enhance TE-polarized emission. The relaxed AlGaN buffer on AlN/sapphire template serves as pseudo-substrate, and in this way the barriers are almost strain-free which limits the formation of strain-related defects in the quantum wells. Transmission measurements confirm a sufficient oscillator strength leading to a high optical absorption coefficient in the wells. The results represent an important step towards the development of DUV light sources, especially for surface-emitting LEDs and lasers. Based on the results of 4-period MQWs, 10- and 20-period MQWs have been grown and characterized, which will be processed for devices by depositing dielectric DBR on the top side and the bottom side. Besides, the typical defects including the threading dislocations and V-pits in the QW samples have been characterized to help to understand their origin, propagation and influences on the structural and optical properties, which may lead to further improvement of the performance of DUV devices.

Chapter 5 is devoted to the theoretical simulations and the experimental realization of BAlN/Al(Ga)N DBRs. The simulations have been established based on transfer-matrix method in our group before to give the theoretical reflection spectra. In this work, different quality factors such as surface roughness, interface roughness and strain in the layers have

been introduced into the simulation and their effects on the performance of DBRs have been analyzed. For the experiments, the growth conditions for BAlGaN DBRs have been discussed. 70% reflection has been achieved at 260 nm and 280 nm by using 18-pair BAlN/Al(Ga)N structures. The experimental data have been compared with the simulations considering quality factors. Although it still needs more efforts to improve structural quality and surface roughness, the progress achieved can help to develop final DBRs with reflection more than 90% and to apply novel BAlN/AlGaN DBRs for DUV resonant-cavity LEDs (RC-LEDs) and VCSELs.

Chapter 6 presents the preliminary results of the device processing, including the time-resolved cathodoluminescence of the active region, the alternative designs of the VCSEL devices, the dielectric DBR properties and the progress for the device structure realization.

In the end, chapter 7 summarizes the results, perspective, publications, communications and awards obtained in this work. The research perspective includes device processing and experiment plans in the new Aixtron 3×2 inch close coupled showerhead (CCS) MOVPE system. The temperatures higher than 1100 °C are expected to favor the growth of AlN, AlGaN with more than 70% Al and BAlN with less than 5% B, which would be applied to improve the quality and hence the performance of BAlN/AlGaN DBRs.

CHAPTER 1

INTRODUCTION

1.1 Motivation

The general objective of this work is to make progress for deep UV (DUV) vertical-cavity surface-emitting lasers (VCSELs) based on BAlGaN material system.

UV and DUV light sources are in high demand in daily life, industrial and research area, as shown in Fig. 1. The UV light at sufficiently short wavelengths can be used as a disinfection method (ultraviolet germicidal irradiation, UVGI) to kill or inactivate microorganisms or pathogens, since it can destroy the nucleic acids in these organisms so that their DNA is disrupted [11]. Therefore it is useful for sterilization and water/air purification. UV light can accelerate the decomposition of organic compounds, which provides better solutions for environmental pollution and plastic recycling. UV radiation is helpful in the treatment of skin conditions such as psoriasis and vitiligo (UV light therapy) [12]. Photography by reflected UV radiation is useful for medical, scientific, and forensic investigations, for the applications of detecting bruising of skin, alterations of documents, or restoration work on paintings. UV photography can also be used in astronomy to identify the chemical compositions of the interstellar medium, the temperature and the compositions of stars [13]. The fluorescence produced by UV illumination can be used in mineralogy, gemology, chemical sensors, fluorescent labelling, biological detectors and so on [14]. High-power UV light can be used for a speed curing process by photochemical reaction that instantly cures inks, adhesives and coatings [15]. UV light can have immediate applications to largely enhance optical storage density, since recording density in the compact disk is proportional to the inverse of the wavelength [16]. UV spectroscopy, along with visible and IR spectroscopy, is routinely used to qualitatively determine the presence of elements and organic compounds by using absorption or transparency of the sample [17].

However, the primary limitation of current applications are the existing UV and DUV

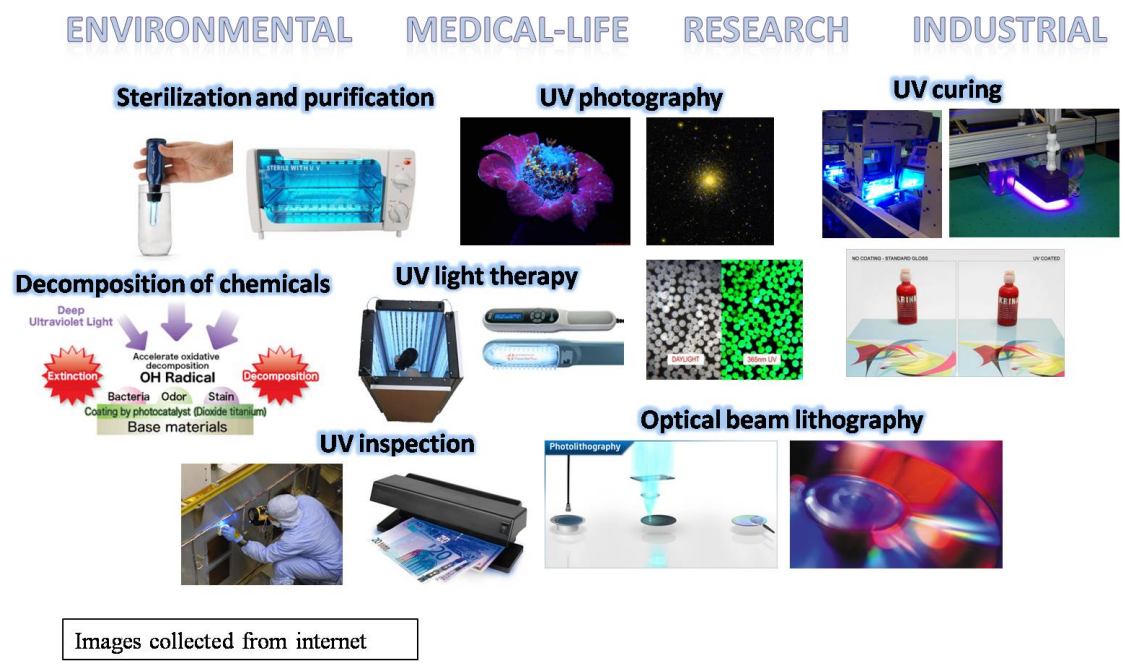

Figure 1: Applications of UV light.

sources. The conventional UV light sources are mercury lamps, Nd: YAG (solid-state) lasers or excimer lasers (for example ArF and Ar_2 lasers). These sources suffer from low level of performance, low reliability, significant size, and the emission of toxic substances. Compared with conventional light sources, the semiconductor light-emitting devices are an ideal choice due to their reliability, compactness and high efficiency. Besides, the wavelength could be tuned by changing the compositions of the active region. UV semiconductor light sources are of great technological interest in our daily lives.

Semiconductor light emitting devices have three configurations: light-emitting diodes (LEDs), laser diodes (LDs) with edge emission, and vertical-cavity surface-emitting lasers (VCSEL). Compared with other two configurations shown in Fig. 2, VCSELs have various advantages. Figure 3 presents the schematic of an optically-pumped VCSEL, which consists of top distributed Bragg reflector (DBR), active region containing MQWs and bottom DBR mirror. The emission light from VCSEL is perpendicular to the surface, so it could be integrated into two dimensional arrays. 10000 devices could be integrated on one wafer to give high output. Circular beam makes it easy to be coupled into the fiber.

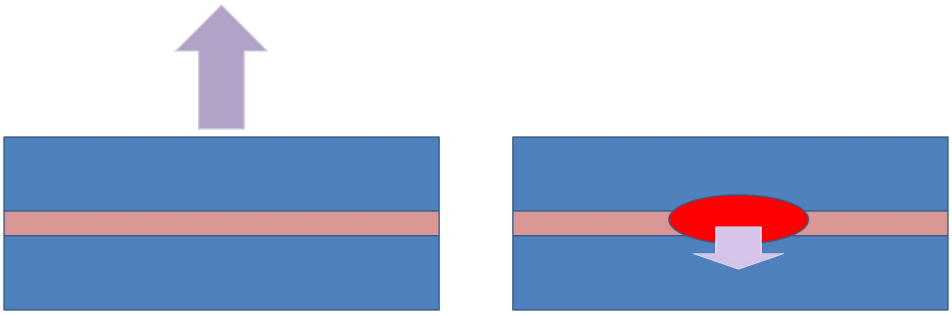

Figure 2: Simple schematic of semiconductor LEDs and laser diodes.

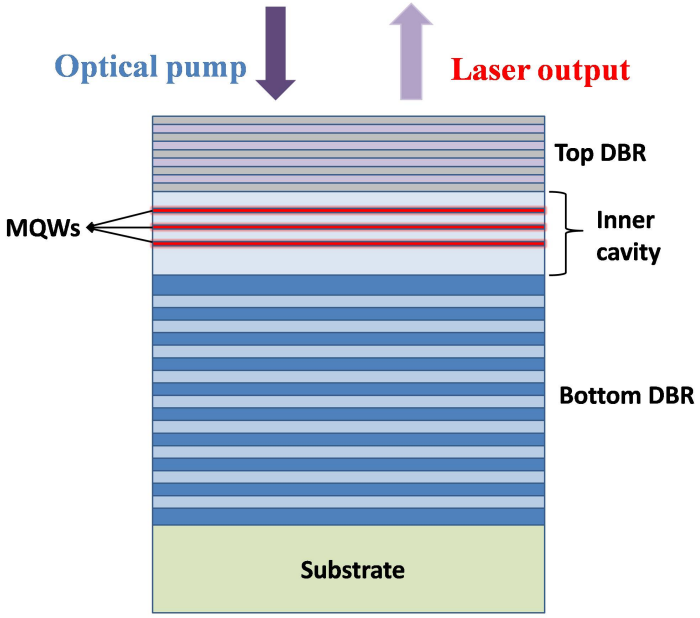

Figure 3: Schematic of optically-pumped VCSEL.

High reflectivity DBR mirrors enable low threshold and high output. Besides, it could be tested on the wafer level during processing which greatly decreases the manufacturing cost. Compared to edge-emitting lasers (EELs), it has low temperature sensitivity due to its single-longitudinal-mode cavity.

AlGaInN-based wide bandgap semiconductors with chemical and thermal stability have brought innovative changes in photonic devices, which enable the operating wavelengths of LEDs and lasers to reach a spectral range spanning from blue to DUV. However, the III-nitride VCSELs demonstrated so far operate in the wavelengths of visible violet and blue spectral range, while no efficient VCSELs operating below 300 nm have been reported. The

general objective of this thesis is to develop the VCSELs operating below 300 nm based on the BAlGaN material system.

1.2 Research problems

To extend VCSEL emission to the ultraviolet region, the challenges lie in many aspects. The first important issue is the active region, which is the basis no matter for the LEDs, laser diodes or VCSELs. For the DUV wavelengths, AlGaN which has high energy bandgap has to be used. But there is a large lattice-mismatch between the layers and commercial substrates such as sapphire and SiC. The structures grown on foreign substrates always have high dislocation density that leads to low internal quantum efficiency (IQE). Bulk AlN substrates with low dislocation density (below 10^8 cm^{-2}) can be used, but they suffer from high impurity absorption, high cost and limited availability. Epitaxial lateral overgrowth (ELO) on sapphire can be used to reduce dislocations [18–21], but it requires complex processing steps such as cleanroom fabrication (lithography and etching) and regrowth of thick layers, which would increase material and time costs.

Besides the quality of substrates, there is also a degradation of the structural quality of epitaxial AlGaN layers with increasing Al molar ratio. The impurity effect is greater in AlN than GaN since Al atoms have small diffusion length (higher sticking coefficient) and increased affinity to oxidize than Ga atoms, which cause rather high density of defects in AlGaN layers with Al content higher than 50% [22, 23].

Thirdly, c-plane nitrides exhibit piezoelectric and spontaneous polarization, which might be useful for piezo-devices but leads to strong quantum-confined Stark effect (QCSE) separating electrons and holes in the MQWs. This phenomenon can significantly reduce the emission efficiency. C-plane AlGaN alloys also exhibit optical polarization anisotropy: E-field $\perp$ c polarized emission (which will be referred to as TE polarization) decreases when compared to the emission polarized along the c axis (E-field || c) as the Al composition increases for the DUV wavelengths, which is detrimental to surface emission.

For current-injected DUV devices, effective doping is difficult to achieve, especially for Al(Ga)N with wide energy bandgap. Si is commonly used as n-dopant. However, Si-doped $Al_xGa_{1-x}N$ layers typically show dramatically increasing resistivity for x>0.70 [24–27] and it's also crucial to obtain effective p-type conductive AlGaN with high Al content. These are due to high donor/acceptor activation energy and compensation effects [27, 28]. So in this work, optical pumping is used to avoid electrical issues.

For the VCSEL structure, another big challenge is the DBRs. In the DUV range, the conventionally used AlGaN/AlN DBRs have smaller refractive index contrast leading to low reflectivity and narrow stopband. The large lattice mismatch between the epitaxial structures and the substrates would give rise to strain-related defects. So, high-reflectivity DBR structures with large stopband width for the UV and DUV spectra need to be further developed.

In the framework of developing DUV VCSELs, this work has be divided into several tasks regarding the different challenges mentioned above that include the realization of AlGaN MQW structures for 280 nm with enhanced oscillator strength of surface emission, MOVPE growth study of new BAlN material, as well as simulation and realization of DUV BAlN/Al(Ga)N DBRs. These tasks are for the processing of final light-emitting devices such as resonant-cavity LEDs (RC-LEDs) and VCSELs.

1.3 State-of-the-art

Visible and UV lasers based upon the wide bandgap semiconductors including ZnSe- and GaN-based material systems have been extensively explored for the potential applications of high density optical storage systems, laser printer engines, full color display systems, and large-area projector systems. The ZnSe-based materials were the first material system to provide continuous wave operation of blue-green edge-emitting lasers (EELs) [29]. However, serious reliability problems possibly arising from its chemically and structurally

unstable material system have hindered the application of ZnSe lasers in the real-world systems. Later, AlGaInN-based wide bandgap semiconductor materials [30, 31] have brought innovative changes in photonic devices, since their strong chemical bonds bring in outstanding chemical and thermal stability, and their direct bandgaps can cover from visible to DUV spectra [32], as shown in Fig. 4. Especially in 2014, the Nobel Prize in physics was awarded to Professor Akasaki, Professor Amano, and Professor Nakamura for their important contributions to bright blue LEDs in the early 1990s [33].

For UV devices, the first nitride-based injection laser centered at around 390 nm was demonstrated in 1995 by the group of Professor Akasaki [34]. AlGaN-based UV LEDs for wavelengths shorter than 360 nm were initiated in 1998 [35]; then UV and DUV light devices based on AlGaInN have undergone tremendous evolution through rapid progress in material growth, device fabrication and packaging. In the DUV range, the LEDs and EELs have been widely reported. The group of Sensor Electric Technology has reported high external quantum efficiency (EQE) of 10.4% at 20 mA continuous current with output power up to 9.3 mW for encapsulated AlGaN LEDs emitting at 278 nm in 2012 [36]. UV Craftory has developed commercial production of 50 mW AlGaN LEDs with wavelength ranging from 255 nm to 355 nm which have more than 10% EQE and over 10000 hour life time [37]. The reported EQE of UV LEDs as a function of the emission wavelength is shown in Fig. 5. Compared with blue LEDs, the EQE decreases rapidly when going towards shorter wavelengths due to high defect density, low extraction efficiency and other problems mentioned in the section 1.2.

For laser diodes or EELs, electrically-injected devices were mostly operating at 320~400 nm. The Palo Alto Research Center obtained lasering at 368 nm with a threshold of 13 kA/cm^2 and maximum output of 300 mW (6.7% for efficiency) [38]. Meijo University demonstrated a threshold of 12.2 kA/cm^2 at 356 nm [39]. The group CRHEA-CNRS reported laser diode at 394 nm with a threshold of 6.7 kA/cm^2 [40]. Hamamatsu Photonics reported laser diodes at 342 nm and 336 nm with threshold of 9 and 18 kA/cm^2 [41]. The

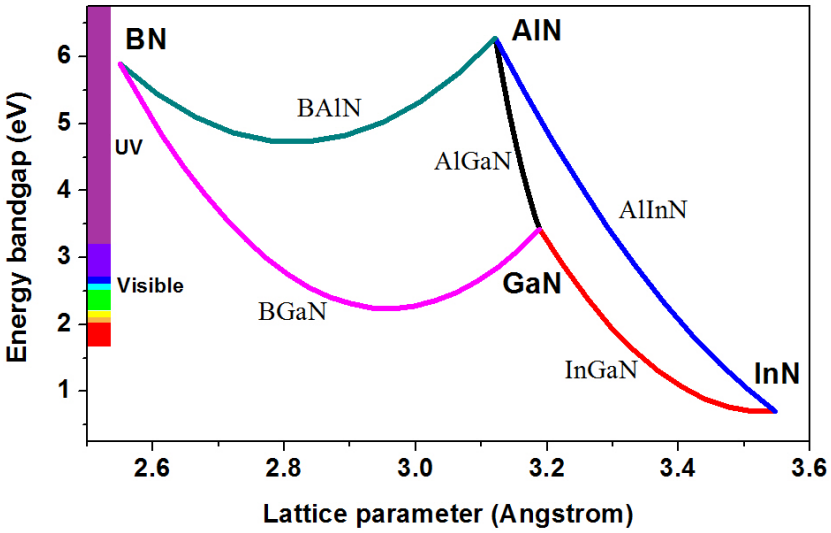

Figure 4: Bandgap energy versus in-plane lattice parameter diagram for III-nitrides.

progress of shorter wavelength devices has been limited by the large dislocation densities and residual strain leading to quality degradation and high optical cavity loss [42].

In DUV region, most of the laser diodes reported are under optical pumping. The group from Technische Universität Berlin has reported the laser grown on the AlN bulk substrate emitting at 279 nm with a threshold of 50 mJ/cm^2 (IQE 20~30%), and the laser grown on ELO (epitaxially laterally overgrown) AlN/sapphire templates emitting at 272 nm with a threshold of 65 mJ/cm^2 (IQE 10~20%). Both are TE-polarization dominant [21]. The Hexatech group reported low threshold power of 84 kW/cm^2 for lasing at 280.8 nm [43] and Palo Alto Research Center demonstrated lasing at 266 nm with a threshold of 41 kW/cm^2 [44]. Both devices are based on the AlGaN MQWs grown on single crystal AlN bulk substrates. To achieve internal quantum efficieny (IQE) higher than 60%, AlN bulk single crystal can be used since its threading dislocation density is below 5×10^8 cm^{-2} [45], but it suffers from high impurity absorption, high cost and limited availability. RIKEN group has used ammonia pulsed-flow multilayer growth to fabricate AlN templates on sapphire to obtain IQE of 60% from AlGaN QWs [45, 46]. Recently, for the devices grown on AlN templates on sapphire, simulated emission was observed at wavelengths of 256 nm and

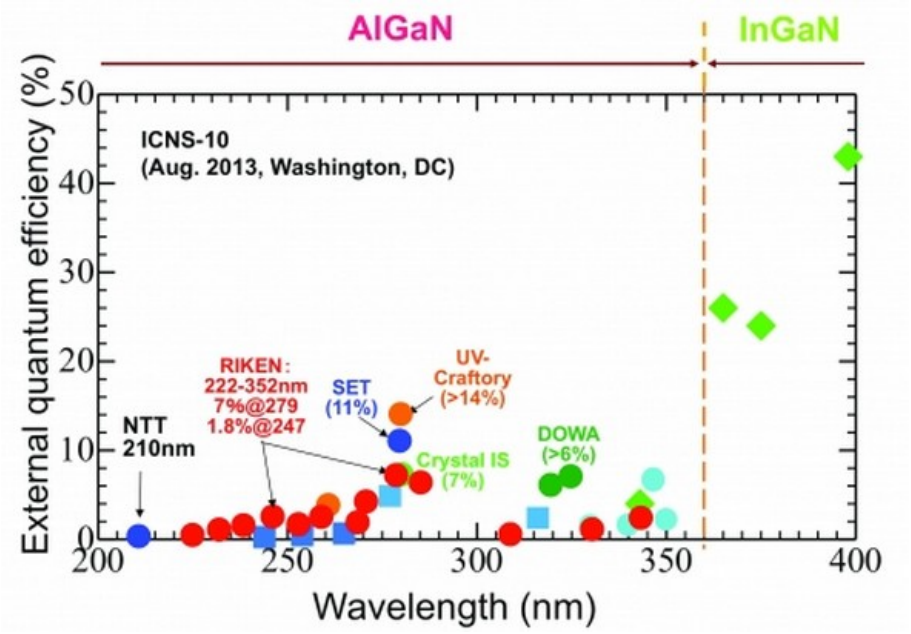

Figure 5: External quantum efficiency as function of wavelength reported at the International Workshop on Nitride Semiconductors in 2012 and ICNS 2013 [2].

249 nm with thresholds of 61 kW/cm^2 and 95 kW/cm^2 at room temperature, as reported by the group of Prof. Dupuis from Georgia Institute of Technology. [47]. It is also reported by Institute of Semiconductors (Chinese Academy of Sciences) that silicon doping could effectively reduce the lasing threshold of UV lasers, and the stimulated emission at 288 nm for the structure grown on AlN/sapphire was obtained at the optical-pumping threshold energy density of 64 mJ/cm^2 (IQE = 42%) [48]. The state-of-the-art optically-pumped AlGaN DUV lasers have been summarized in Fig. 6.

It is worth noting that very recently a breakthrough has been achieved by McGill university. They reported the first 210 nm emitting AlN nanowire LEDs on Si substrates with a turn on voltage of about 6 V, which is significantly lower than the commonly observed 20~40 V due to efficient Mg doping [49]. They reported the first electrically-injected AlGaN lasers on Si operating at 320~340 nm with ultra-low threshold (tens of A/cm^2) [42] by using AlGaN core-shell nanowires. Then, the electrically-injected AlGaN nanowire lasers grown directly on Si substrates were achieved, which operates at 262.1 nm at 77 K with a

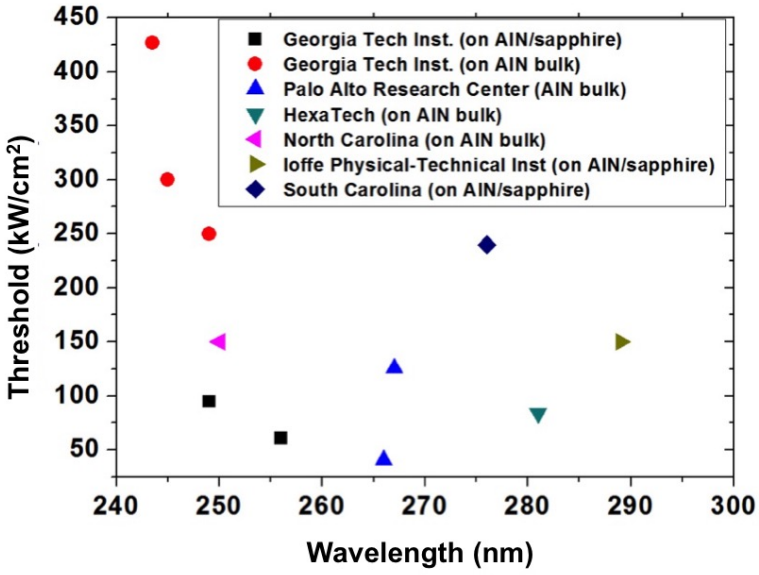

Figure 6: State-of-the-art optically-pumped AlGaN DUV lasers.

threshold of 200 A/cm^2 [50]. The nanowire structure provides an avenue for electrically-injected DUV lasers.

The development of III-nitride-based VCSELs includes optically-pumped devices at blue wavelengths [51, 52] and room temperature (RT) current-injected VCSELs at blue/violet wavelengths [53–55]. Redwing et al. from Advanced Technology Materials [51] developed an optically-pumped VCSEL based on GaN active region sandwiched between 30-period $Al_{0.4}Ga_{0.6}N/Al_{0.12}Ga_{0.88}N$ DBRs. A narrow laser mode appeared at 363 nm and the threshold was around 2 MW/cm^2 at room temperature. Krestnikov et al. from A.F. Ioffe Physico-Technical Institute (Russian Academy of Science) reported photopumped InGaN/GaN/AlGaN VCSEL at the wavelength of 401 nm and 415 nm with thresholds of 400 kw/cm^2 and 550 kw/cm^2. A 2λ vertical cavity included twelvefold stacked InGaN insertions in a GaN matrix grown on top of 37-period $Al_{0.15}Ga_{0.85}N$/GaN DBR [52] and GaN/air interface acted as top mirror. Higuchi et al. from Nitride Semiconductor Research Laboratory in Japan demonstrated continuous wave (CW) lasing VCSEL at 414 nm with threshold current of 7.0 mA at RT [53]. It was mounted on a Si substrate by a wafer bonding and the

sapphire substrate was removed by laser lift-off. The active region consisted of a 2-pair InGaN/GaN QWs. 7λ GaN cavity was embedded between two SiO_2/Nb_2O_5 DBRs. Recently in 2014, Lin et al. from National Chiao Tung University in Taiwan showed an InGaN VCSEL, in which the application of composition-graded electron blocking layer reduced the threshold from 12.6 to 9.2 kA/cm^2 and enhanced output power by a factor of 3.8 [54]. So far, no efficient VCSELs operating below 300 nm have been reported.

One of the biggest challenges for UV VCSELs lies in the need for high-reflectivity DBRs. Conventional AlGaInN-based DBRs have been explored to give high reflectivity from blue to the near-UV region. For example, 25-pair $Al_{0.18}Ga_{0.82}N/Al_{0.8}Ga_{0.2}N$ with a reflectivity as high as 99% and a stopband width of 26 nm at central wavelength of 347 nm was reported by Mitrofanov et al. from Bell Laboratories [56]. Feltin et al. from Ecole Polytechnique Fédérale de Lausanne also used $Al_{0.2}Ga_{0.8}N/Al_{0.85}In_{0.15}N$ lattice matched system to achieve 99% reflectivity at 340 nm [57]. For the DUV wavelengths, the DBRs based on conventional AlGaInN material system are shown in Tab. 1. Moe et al. from University of California - Santa Barbara demonstrated reflectivity of 66.6% and 82.8% for the wavelengths of 245 nm and 279 nm, using 10-period $Al_{0.63}Ga_{0.37}N$/AlN and 21-period $Al_{0.58}Ga_{0.42}N$/AlN, respectively [58]. Getty et al. from the same group achieved 80% reflection at 254 nm and 280 nm by using 19-period $Al_{0.60}Ga_{0.40}N$/ $Al_{0.95}Ga_{0.05}N$ [59]. Zhang et al. from Nanjing University in China obtained 83.9% reflection at 246 nm by using 13-pair $Al_{0.77}Ga_{0.23}N/Al_{0.98}In_{0.02}N$ [60], and 68.8% reflection at 247 nm by using 11-pair $Al_{0.70}Ga_{0.40}N$/AlN [61]. Very recently, Hoffmann et al. from North Carolina State University reported the highest reflectivity of 97 % at 270 nm by using 24.5-pair $AlN/Al_{0.65}Ga_{0.35}N$ strain-compensated DBRs on $Al_{0.85}Ga_{0.15}N$ relaxed buffer [62].

It is difficult to achieve high reflectivity requirement due to large absorption and small refractive index contrast of the materials in DUV region. Conventionally-used AlGaN layers exhibit lattice mismatch as high as ~2.4% between GaN and AlN to achieve only a small refractive index contrast in the mirror structure. The high reflectivity requiring large

Table 1: State-of-the-art distributed Bragg mirrors based on AlGaInN for wavelengths below 300 nm.

References	Structures	Reflectivity	Stopband width
[58]	10-pair $Al_{0.63}Ga_{0.37}N$ / AlN	66.6% R at 245 nm	~20 nm
[58]	21-pair $Al_{0.58}Ga_{0.42}N$ / AlN	82.8% R at 279 nm	~18 nm
[59]	19-pair $Al_{0.60}Ga_{0.40}N$ / $Al_{0.95}Ga_{0.05}N$	80% R at 254 nm	~10 nm
[59]	19-pair $Al_{0.60}Ga_{0.40}N$ / $Al_{0.95}Ga_{0.05}N$	80% R at 280 nm	~17 nm
[60]	13-pair $Al_{0.77}Ga_{0.23}N$ / $Al_{0.98}In_{0.02}N$	83.9% R at 246 nm	~18 nm
[61]	11-pair $Al_{0.70}Ga_{0.40}N$ / AlN	68.8% R at 247 nm	~18 nm
[62]	24-pair $Al_{0.65}Ga_{0.35}N$ / AlN	97% R at 270 nm	~10 nm

number of pairs was accompanied by the dislocations, cracks or rough interfaces. So the novel system needs to be considered to build efficient DBR structures below 300 nm. In this thesis, BAlGaN materials will be studied. The primary reason for the B incorporation is that a very small amount of B in AlN could introduce a strong refractive index contrast [63, 64]. For example, at the wavelength of 280 nm, the $Al_{0.65}Ga_{0.35}N$/AlN system has refractive index contrast of 0.07 with lattice mismatch as large as 0.8%. Meanwhile, BAlN with only 1.2% B can have a refractive index contrast of 0.17 with AlN and lattice mismatch is as small as 0.2%. Besides, BAlN system exhibits less optical absorption than AlGaN due to its large bandgap. Additionally, strain-compensated structure could be designed by alternating BAlN and AlGaN layers in the DBR so that both the large refractive index contrast and lattice matched structure could be obtained at the same time. By using this material, our group has obtained 60% reflection at 282 nm by 18-pair BAlN/AlN, 82% reflection at 311 nm by 24-pair BAlN/AlN [64] and 92% at 360 nm by replacing AlN with AlGaN. DBRs based on different nitride systems including Al(Ga)N/Al(Ga)N, AlInN/Al(Ga)N, BGaN/GaN and BAlN/Al(Ga)N are summarized in Fig. 7.

The study of boron containing materials can be very helpful for III-nitride devices since boron can bring additional freedom in engineering the bandgap, lattice constant and refractive index of multi-layered structures. For example, besides the enhanced refractive index contrast mentioned earlier, the BAlGaN system can decrease or eliminate lattice mismatch on SiC and AlN substrates [65–67]. However, further investigation of the basic epitaxial

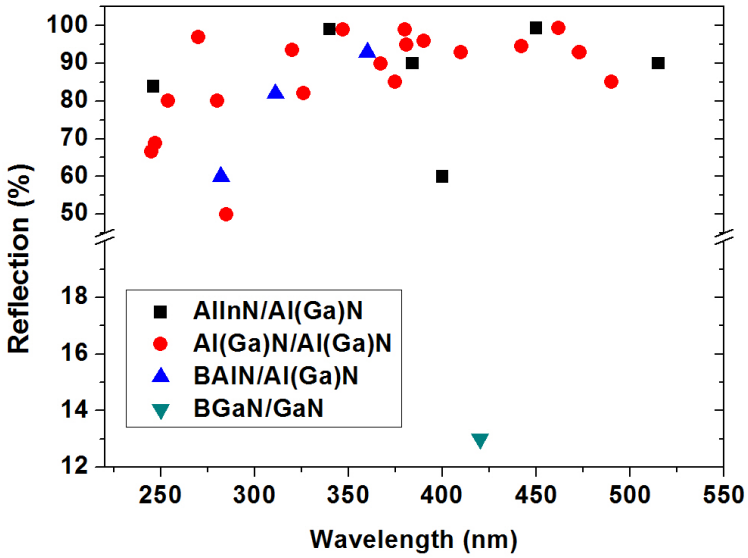

Figure 7: DBR reflectivity for various nitride systems.

growth is required for this new material. BAlN and BGaN have been grown by MOVPE [63, 64, 68–75], MBE [67, 76, 77] and magnetron sputtering [78, 79], but the boron content and crystallinity are limited due to phase separation, short diffusion length of boron and strong parasitic reaction in the gas phase [68, 72, 76, 78, 80]. By magnetron sputtering, Liljeholm et al. from Dev. Solid State Electronics in Sweden achieved high crystalline quality of BAlN with 18% boron [78]. By MOVPE method BAlN materials have normally been grown above 1050 °C [63, 68, 69, 75], or at 1000 °C by using flow-modulate epitaxy (FME) [72, 81] in order to enhance migration of boron and aluminum atoms. But clear XRD peaks of wurtzite-BAlN layers reported are related to only 1~2% boron [63, 68, 72, 75]. Shibata et al. from Kohgakuin University in Japan [69] showed high boron content incorporation by MOVPE, but the related XRD peak intensity was very weak. Further study for BAlN with high boron content has to be established for its big potential in applications such as MQWs, DBRs, and sensors.

1.4 Scope of the thesis

The objective of the project is for making progress on VCSELs operating below 300 nm based on the BAlGaN materials. 280 nm is targeted since it is a common wavelength used in the market for DUV applications such as sterilization or water purification. The VCSEL structure consists of dielectric top mirror, AlGaN active region and bottom DBR, and this work contributes to the two main parts: AlGaN-based active region and BAlGaN-based DBRs.

Chapter 1 introduces the background of the project. The motivation of the project including possible applications is stated. The research problems in different aspects regarding this topic are described. The state-of-the-art of different types of light emission devices, DBRs for DUV wavelengths and progress of BAlN is also summarized in this chapter.

Chapter 2 presents the basic properties of III-nitride material, and a brief introduction of the techniques and equipments used for the growth and characterizations is included.

Chapter 3 is devoted to the MOVPE growth studies of AlGaN and BAlN on AlN/sapphire templates. Firstly, AlGaN single layers with different composition and relaxation are calibrated. Based on these samples, the relationship between composition and strain state is discussed. Different models are brought in to predict the range of critical thickness of AlGaN grown on AlN. The method to calculate screw/edge threading dislocation density of AlGaN and AlN layers based on XRD measurements is also established. Secondly, for the studies of novel BAlN material, the characteristics of BAlN with high boron content (more than 10%) are analyzed. In order to improve the crystalline quality of BAlN, a method of low-temperature growth with annealing is proposed. The influences of growth temperature and TEB/III ratio on the boron composition and on the crystalline quality are investigated. The preliminary results of AlN/sapphire template optimization by using new Aixtron close coupled showerhead (CCS) reactor are also presented.

Chapter 4 is addressed to the AlGaN MQWs emitting at 280 nm. The design of MQWs is to enhance TE-polarized emission. The structural and optical properties of 4-, 10- and

20-period MQWs are studied here.

Chapter 5 focuses on the theoretical simulation and the experimental realization of BAlN/Al(Ga)N DBRs. For the reflector software developed before in our group, different factors leading to degradation of DBR performance such as the surface/interface roughness and the strain are introduced into the simulations, and their influences are discussed. Then a series of BAlN/Al(Ga)N DBRs are grown by MOVPE and analyzed by different characterization methods.

Chapter 6 presents the preliminary processing progress for the light emitting structures consisting of AlGaN DUV MQWs and dielectric DBRs.

Chapter 7 is divided into three sections. Firstly, the conclusion part summarizes the results of this thesis. Secondly, the further possible research directions for optimizing MQWs and DBRs as well as achieving final devices are proposed in the perspective part. The publications and awards achieved during the time of Ph.D study are listed in the end of the chapter.

CHAPTER 2

FUNDAMENTALS OF MATERIALS AND EXPERIMENTS

2.1 Fundamental properties of III nitrides

The III nitrides are excellent wide bandgap semiconductors with outstanding features. They have enabled a revolution in modern electronic and optoelectronic applications. The basic properties of III-nitrides are described in the following sections, which are the fundamentals in the aspect of materials used in this work.

2.1.1 Structural properties of III nitrides

III-nitrides including binary, ternaries and quaternaries of (B, Al, Ga, In)N have two types of crystalline structures: hexagonal and cubic. Under the typical MOVPE growth conditions, they crystallize in the most thermodynamically stable form into wurtzite structure, except that the BN favors hexagonal (graphitic) prototype. As shown in Fig. 8, wurtzite crystallographic structure has nitrogen atoms forming a hexagonal close packed structure while the group III elements occupying half of the tetrahedral sites available in the lattices. Or it can be seen as two interpenetrating hexagonal close packed sub-lattices, and each sub-lattice is shifted along c-axis by 3/8 of the cell height. Each atom in the lattice is tetrahedrally coordinated. Typical crystal orientations and planes of wurtzite III-nitrides are illustrated in Fig. 9.

Since there is a large disparity of electronegativity between III elements and nitrogen atoms with small atomic radius, the III elements and nitrogen are bound by strong covalent bonds. Therefore, III-nitrides are chemically and physically stable. III-nitrides also show high thermal conductivity as seen in Tab. 2. Owing to their structure and thermal stability, III-nitrides are suitable candidates for high temperature and high power applications. The lattice parameters of hexagonal BN, AlN, GaN and InN are summarized in Tab. 2. The

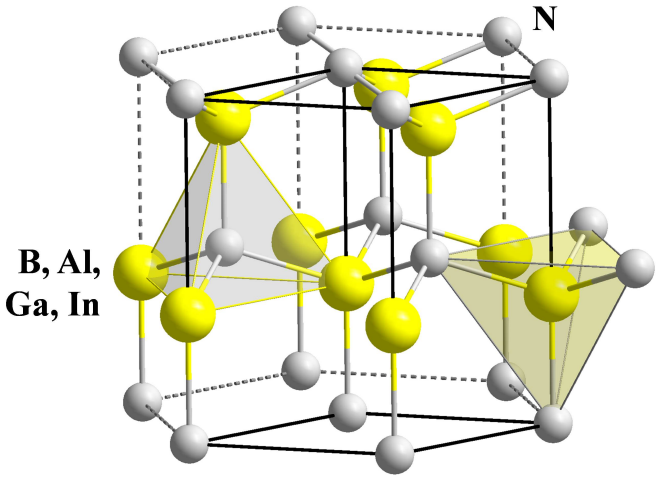

Figure 8: Wurtzite crystal structure of III nitrides [3].

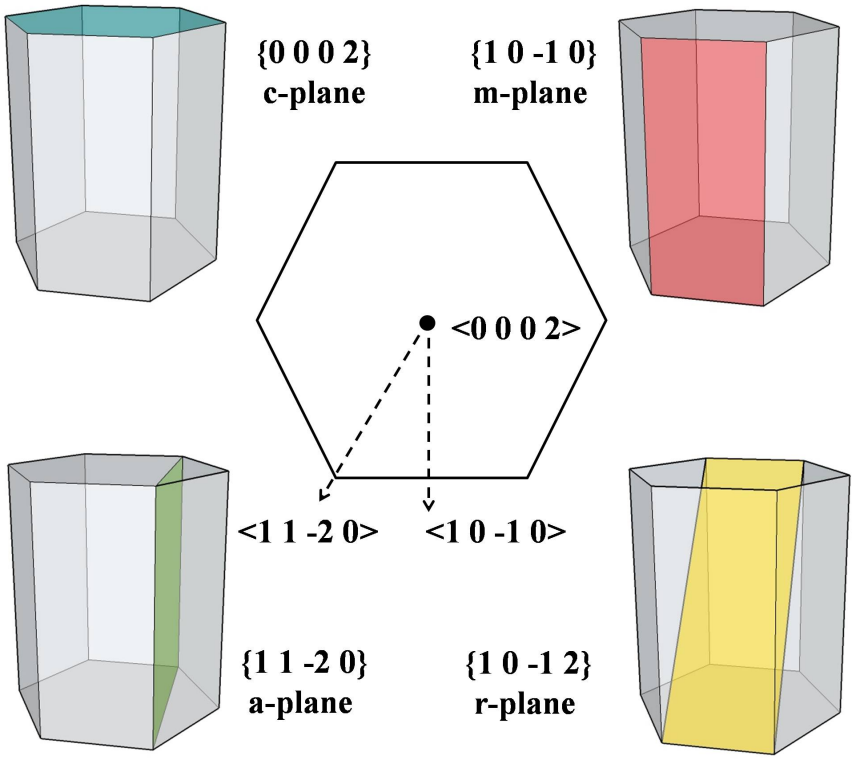

Figure 9: Typical crystal orientations and planes of wurtzite III-nitrides.

Table 2: Properties of III-nitrides binaries [1].

Parameters	BN	AlN	GaN	InN
a(Å)	2.55	3.122	3.189	3.548
c(Å)	4.17	4.982	5.185	5.718
E_g (eV)	5.9	6.28	3.42	0.7
Thermal expansion ($\triangle$a/a) ($10^{-6}k^{-1}$)	-2.7	4.15	5.59	3.8
Thermal expansion ($\triangle$c/c) ($10^{-6}k^{-1}$)	38	5.27	3.17	2.9
Thermal conductivity ($W{\cdot}cm^{-1}k^{-1}$)	6 ($\|$a), 0.3 ($\perp$a)	2.85	1.3	0.45

lattices of ternaries can be calculated by Vegard's law [82]:

$$a, c(A_xB_{1-x}N) = a, c(AN) \cdot x + a, c(BN) \cdot (1 - x) \ . \tag{1}$$

One of the technical challenges of III-nitride applications is the lack of lattice-matched substrates. Commercially available, low-cost and thermal stable sapphire substrates were used in the majority of the research work. Although it has large lattice mismatch with III-nitrides, GaN templates grown on sapphire have already been achieved with the dislocation density down to $\sim 10^8$ cm^{-2} by using low temperature nucleation layer, which was proposed by Nakamura in 1991 [83], and they have been widely used for visible and near-UV light emitting devices. For DUV devices, the high quality AlN substrates are still under investigations now and the method to reduce dislocation densities is an important topic.

2.1.2 Optical properties of III nitrides

2.1.2.1 III nitride bandgaps and band crossover of AlGaN

III-nitrides have wide bandgaps spanning a wide range from 0.7 to 6.2 eV (as shown in Fig. 4 and Tab. 2), especially the BAlGaN covers the UV and DUV region. The energy bandgaps of ternaries can be calculated directly from their binaries:

$$E_g(A_xB_{1-x}N) = E_g(AN) \cdot x + E_g(BN) \cdot (1 - x) - b \cdot x \cdot (1 - x) \ . \tag{2}$$

In this equation, "b" represents the energy bandgap bowing parameter. Tab. 3 summarizes some bowing values of III-nitrdes. In fact, there is a large spread and uncertainty of values for bowing parameters in the literature. For example, the bowing parameter of

Table 3: Bandgap bowing parameters of III-nitrides ternaries.

	BAlN	BGaN	AlGaN	AlInN	InGaN
Bowing (eV)	5.45 [86]	9.2 [74]	1 [87]	2.5 [87]	3 [87]

1 eV is often used in band calculations of AlGaN. Meanwhile, Lee et al. recommended a value of 0.6 eV for intrinsic bandgap bowing of AlGaN. They found that the AlGaN layers directly nucleated or buffered on sapphire at high temperatures usually lead to a strong downward bowing of at least 1.3 eV, and it also tends to jump to strong bowing as Al fraction increases [84]. The apparent strong bowing might be an artifact resulting from defect- or impury- related transitions at energies below the bandgap [85].

Few results have been reported on bowing parameters of boron-based III-nitrides. For BGaN material, the value of 9.2 eV has been experimentally obtained by group of Ougazzaden [74]. For BAlN, there is only theoretical calculations showing that BAlN has strong bowing parameter of 5.45 eV [86]. Since BAlN material is not as well studied as other III-nitrides, it still requires more experimental investigations for its optical properties.

In AlGaN alloys which constitute the active region of DUV light emitting devices, the order of the two upper valence bands is modified with respect to binary GaN. Apart from the modification of the electric band structure, alloying also leads to a modification of the optical polarization properties of the interband transitions, which influences the performance of the devices. In GaN, the crystal field term Δ is positive, so the upper valence band corresponds to the heavy hold band of Γ_9 symmetry, while the second one corresponds to the split-off hole band of symmetry Γ_7. However, the Δ term for AlN is negative with Γ_7 symmetry becoming the upper band. In this case, along with the increase of Al content in AlGaN, the energy order of heavy hold band and split-off hole band reverses at a certain composition (Fig. 10). The crossover point would be influenced by the parameters used in the theoretical calculations as well as the strain state of the layer [88, 89]. For example, Nam et al. reported a crossover point of x_{Al}=0.25 [88] while Leroux et al. obtained a crossover composition of x_{Al}=0.1 [89]. This energy band crossover between AlN

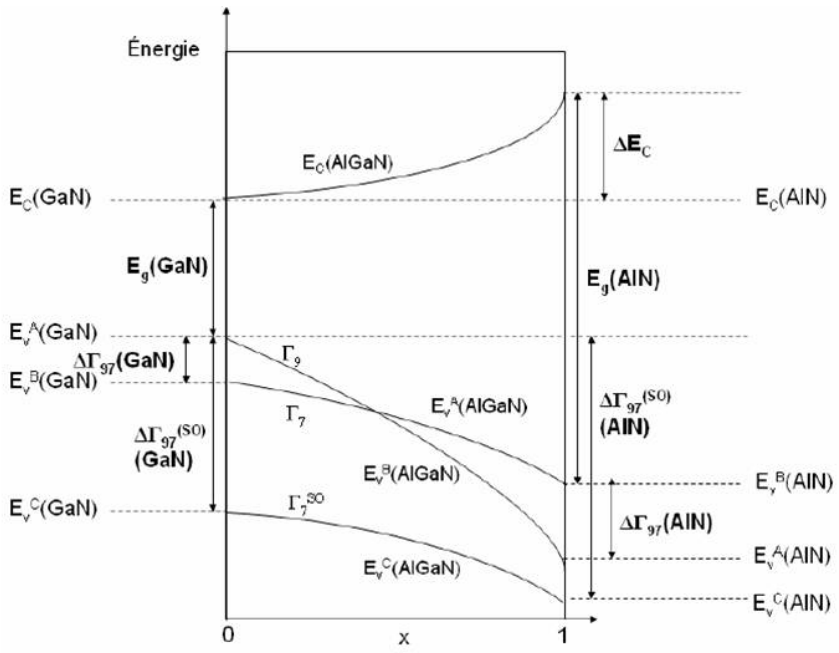

Figure 10: Band alignment of GaN/AlGaN structure [4].

and GaN is also accompanied by a switching of the valence band state symmetry. The topmost Γ_7 valence band is governed by p_z-like state. The following bands (Γ_9 and lower Γ_7) are governed by p_x and p_y-like states. The oscillator strength of the optical transitions is then modified and consequently the interband absorption coefficients (and stimulated-emission coefficients) are changed. In particular, the oscillator strength between the conduction band and the upper Γ_7 valence band, which becomes the fundamental transition, is highly reduced with increasing Al fraction for the configuration where the electric field is perpendicular to the c axis [88–92]. This effect is detrimental to the surface emission of AlGaN-based DUV LEDs and lasers, and it needs to be considered during the design of the devices. The band structure and alignment are detailed in the section 4.1.1.

2.1.2.2 Polarization and quantum-confined Stark effect

III-nitrides display strong spontaneous and piezoelectric polarization due to their wurtzite crystal structure and high degree of ionicity. The polarization-induced electric fields can cause strong quantum-confined Stark effect (QCSE) in the QWs and reduce significantly

Table 4: Polarization elastic parameters from the literature.

	AlN	GaN	InN
P_{sp} [C/m^2]	-0.081 [93]	-0.029 [93]	-0.032 [93]
e_{33} [C/m^2]	1.46 [93]	0.73 [93]	0.97 [93]
e_{31} [C/m^2]	-0.60 [93]	-0.49 [93]	-0.57 [93]
ε	10.7 [97]	10.4 [98]	14.6 [99]
C_{13} [GPa]	94 [100]	68 [100]	70 [100]
C_{33} [GPa]	377 [100]	354 [100]	205 [100]

the internal quantum efficiency.

The total polarization is described as the sum of spontaneous polarization and piezoelectric polarization:

$$P = P_{sp} + P_{pz} \ . \tag{3}$$

Spontaneous and piezoelectric polarization of ternary alloys could be interpolated by two end points (Vegard's law). Taking $Al_xGa_{1-x}N$ as an example, two types of polarization can be expressed as:

$$\begin{aligned} P_{sp}(Al_xGa_{1-x}N) &= xP_{sp}(AlN) + (1-x)P_{sp}(GaN) \\ P_{pz}(Al_xGa_{1-x}N) &= xP_{pz}(AlN) + (1-x)P_{pz}(GaN) \ . \end{aligned} \tag{4}$$

P_{sp} for each binary could be obtained from literatures, and P_{pz} is related to the strain of the layer described as following equations [5, 93–96]:

$$\begin{aligned} P_{pz} &= e_{ij}\epsilon_j \\ P_3 = e_{33} + e_{31}(\epsilon_1 + \epsilon_2) &= 2\frac{a-a_0}{a_0}(e_{31} - e_{33} \cdot \frac{C_{13}}{C_{33}}) \ , \end{aligned} \tag{5}$$

where e_{ij} is piezoelectric coefficients, ϵ_j is strain tensor, e and C are the piezoelectric coefficients and elastic constants, respectively. Parameters a and a_0 are in-plane lattice parameters under the strain and free of strain. The polarization and elastic parameters from the literature are summarized in Tab. 4.

The orientation of spontaneous/piezoelectric polarization is indicated in Fig. 11. The spontaneous polarization field for GaN, AlN and InN (0 0 0 1) films are in the [0 0 0 -1]

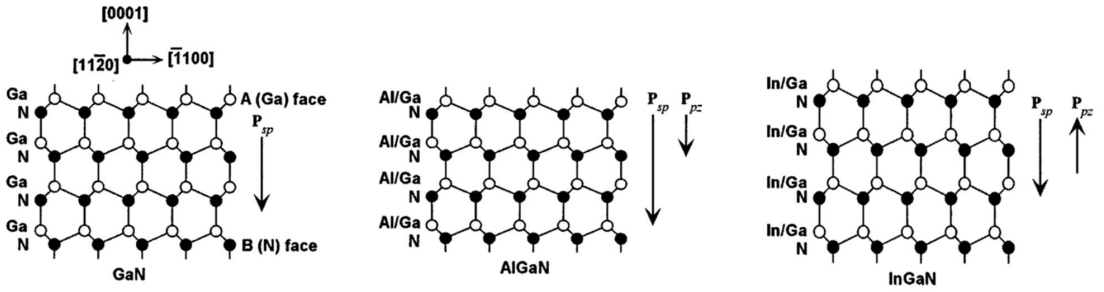

Figure 11: Spontaneous polarization field (P_{sp}) and piezoelectric polarization field (P_{pz}) for GaN, AlGaN and InGaN coherently strained to GaN (0 0 0 1) [5].

direction. The relevant piezoelectric field of (0 0 0 1) films is in the [0 0 0 1] direction under compressive strain and in the [0 0 0 -1] direction under tensile strain [5].

For MQWs, the conservation of the electric displacement vector across the heterostructure leads to:

$$\varepsilon_w E_w - \varepsilon_b E_b = P_b - P_w \ , \tag{6}$$

where ε_w (ε_b) is the dielectric constant of well (barrier), E_w (E_b) is the electric field in the well (barrier), and P_w (P_b) is the zero-field polarization of the well (barrier). After combining the boundary condition:

$$L_w E_w + L_b E_b = 0 \ , \tag{7}$$

where L_w and L_b are the widths of the well and the barrier, the built-in electric field could be deduced from polarizations [95, 101]:

$$E_w = \frac{L_b(P_b - P_w)}{(\varepsilon_b L_w + \varepsilon_w L_b)} \ . \tag{8}$$

The electric field in the QWs leads to the bending of energy bandgap: the electron states shift to lower energies, while the hole states shift to higher energies. The effective energy bandgap is reduced resulting in longer wavelength. Additionally, the electric field shifts electrons and holes to the opposite side of the well, decreasing the overlap of wavefunctions [102]. This effect is called quantum-confined Stark effect (QCSE). In the simplest approximation, the photoluminescence energy E_{PL} can be expressed as:

$$E_{PL} = E_e + E_h + E_g - E_{exc} - eFL \ , \tag{9}$$

where E_g is the energy bandgap, E_{exc} is the exciton binding energy, E_e and E_h are energies of the first quantum levels in the well for electrons and holes, F is the total electric field and L is the thickness of the quantum well. In AlGaN/AlGaN MQWs, the emission wavelength and recombination efficiency are strongly affected by built-in electric field E and the thickness of the wells. By reducing the thickness of the wells, QCSE can be alleviated.

2.2 Experimental methods

2.2.1 Metal-organic vapor-phase epitaxy

Metal-organic vapor-phase epitaxy (MOVPE) is one of the methods utilized to epitaxially grow semiconductor materials. Compared with other techniques such as hydride vapor phase epitaxy (HVPE) or molecular beam epitaxy (MBE), the strengths of MOVPE technique include high growth rate, versatility, high quality, and suitability for large-scale production, which make it become a major process in the manufacture of optoelectronics.

2.2.1.1 Basic principles

MOVPE growth is governed by the diffusion processes, and it is conducted under near thermodynamic equilibrium conditions that rely on the vapor transport of precursors in a heated zone [103]. The sources of group III elements are either liquids (trimethylgallium, trimethylaluminum, thriethylgallium, triethylborane) or solids (trimethylindium). They are stored in bubblers that are maintained at a constant temperature. The carrier gas (nitrogen or hydrogen) flows into the bubblers, saturates with vapor of the sources and transports them into the reactor. The schematic of III-nitride epitaxial growth is illustrated in Fig. 12. The wafer is heated in the reactor chamber to create near equilibrium conditions. The organometallic precursors are mixed with ammonia near the inlet of the reactor and are then transported to the heated zone. The heated organic precursor molecules decompose in the absence of oxygen or any halogen (pyrolysis). The resulting species diffuse through the boundary layer to the growing surface and attach onto the substrate by physisorption. The species can desorb or react with other surface species at this moment. To form a new layer,

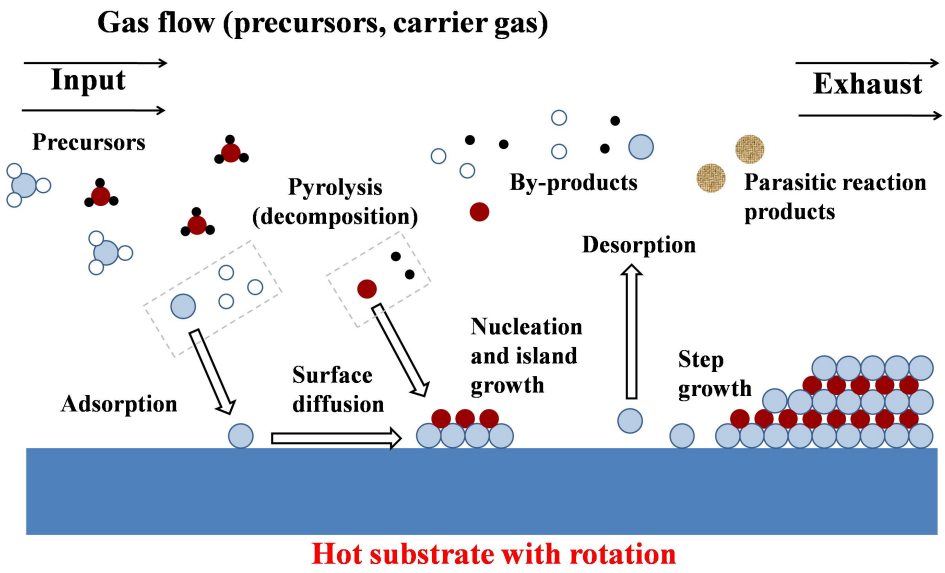

Figure 12: Schematic of III-nitrides epitaxial growth.

the species can diffuse on the surface and bound tightly at the bottom of a growth step, or nucleate at other positions to form islands. The general reaction is described in the Eq. 10:

$$R_3M + NH_3 \leftrightharpoons MN + 3RH \ . \tag{10}$$

The byproducts that form during the deposition reactions diffuse into the carrier gas away from the deposition zone and flow into the reactor exhaust. Parasitic reactions between precursors can also occur in the gas phase which would reduce the incorporation efficiency of sources and degrade the quality of epitaxial layers since the particles of the byproducts may fall on the substrate surface hindering the formation of single crystal.

MOVPE growth is a complex process including thermodynamics, kinetics, hydrodynamics and mass transport. The theoretical details can be found in [103]. Generally speaking, there are several basic growth parameters which can be adjusted to control the growth rate and the quality of epitaxial layers: temperature, pressure, V/III ratio (the ratio of ammonia flow rate to the total flow rate of organometallic precursors), III/III ratio (the concentration of one type organometallic precursor in the total organometallic precursors), carrier gas.

Growth temperature should be optimized for the epitaxy of different alloys. On one

hand, it requires energy for the pyrolysis of precursors, the diffusion of the atoms on the substrate and activation of the reactions, which is important for the growth rate and surface structural property. On the other hand, at very high temperature, the desorption would be dominant and the substrate surface can be decomposed. Additionally, high temperature would lead to strong parasitic reactions between precursors. Furthermore, growth temperature can strongly shift the composition of In in III nitrides such as InGaN and AlInN.

MOVPE growth of III nitrides is normally done under low pressure (10-300 Torr), in order to reduce the parasitic reactions.

V/III ratio is important for the quality of the layers. If the V/III ratio is too low, supply of nitrogen atoms would be inefficient, and nitrogen vacancies and auto background doping would be increased. But if the V/III ratio is too high, parasitic reactions would be aggravated and surface mobility of adsorbed atoms would be impeded. III/III ratio which means the concentration of one precursor in the total precursors for III elements (such as TMAl/III and TMG/III) is the key parameter to adjust the composition of the ternary or quaternary alloys. But under the same gas-phase concentration, the composition can also be shifted due to other parameters including temperature, pressure, or the change of the strain state (composition pulling effect).

The carrier gas used in this work is H_2, since it has beneficial thermal conductivity, faster diffusivity of precursor species and carbon-radical scouring properties compared with N_2. It should be noted that the presence of hydrogen atoms is detrimental to InGaN growth since it enhances the In desorption and it is harmful to Mg-doped layers due to the formation of Mg-H complexes.

2.2.1.2 Equipment and in-situ characterizations

Epitaxial materials and structures studied within this work were grown by low-pressure metal-organic vapor-phase epitaxy (LP-MOVPE) using a home-made system if not specified. This system was designed and installed by Prof. Abdallah Ougazzaden [104], as shown in Fig. 13. The system includes four basic elements: gas handling system, reactor

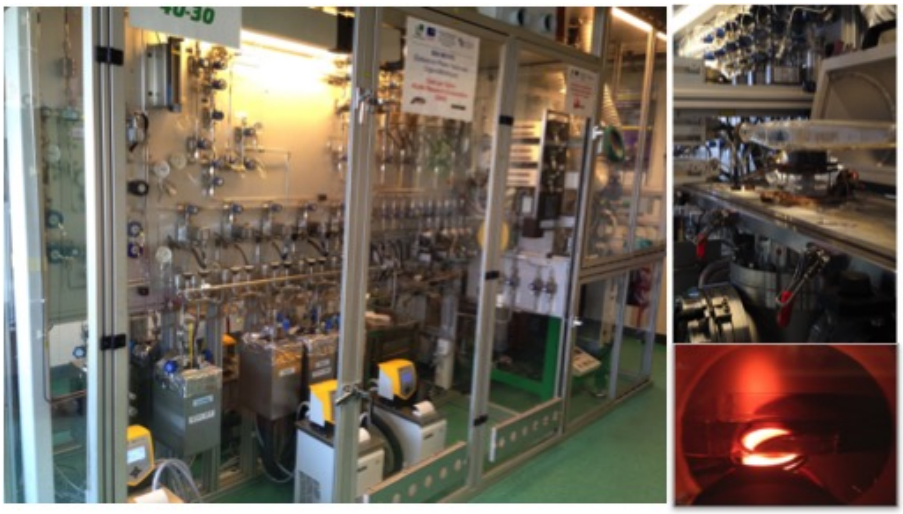

Figure 13: MOVPE system and T-shape reactor chamber.

Figure 14: Aixtron 3×2 inch, close coupled showerhead (CCS) MOVPE system.

chamber, heating system and an exhaust (low pressure) pumping system. The growth was performed in a T-shape reactor [105]. The temperature range is from 400 °C to 1040 °C and the pressure in the reactor can be regulated from 80 to 450 Torr for the growth. Hydrogen or nitrogen can be used as carrier gas. The cold-wall system is applied so that the substrate is much hotter than the other zone and the reactants can be depleted here contributing to the growth. During growth, the substrate is rotated at 60 rpm to enhance the layer homogeneity and to help maintain the laminar flow on the sample surface.

A new Aixtron 3×2 inch, close coupled showerhead (CCS) MOVPE system has also been brought into operation and it is shown in Fig. 14. The surface temperature of substrates in this reactor can reach 1300 °C. This system was used for optimizing AlN/sapphire

templates which require temperature higher than 1100 °C. The future plans for improving the quality of BAlN layers will also be performed in this new reactor.

The MOVPE system is equipped with an in-situ optical reflectance monitor in order to estimate the growth rate and get fist information of the surface quality of the sample.

Laser beam with wavelength of 633 nm is launched at the wafer and detected at normal incidence. Interference between the reflection at the surface of thin films and reflection at the bottom causes oscillations of detected light intensity as the layer is grown. The growth rate can be calculated by the following equation:

$$Growth\,rate = \lambda/(2n\triangle t)\ , \tag{11}$$

where λ is the wavelength of the laser beam, n is refractive index of the layer and $\triangle t$ is the time interval between two maxima or two minima of oscillations.

During the growth of single layer, there would be additional light scattering due to the surface roughness. The reduced reflection intensity of maxima or minima indicates the increase of surface roughness, which can be expressed quantitatively as follows:

$$R = R_0 \cdot e^{-(4\pi\sigma/\lambda)}\ , \tag{12}$$

where R is the mean value of reflectance oscillations, λ is the used wavelength and σ refers to the root mean square of roughness.

2.2.1.3 Precursors and calculations of debit

Trimethylaluminum (TMAl), thrimethylgallium (TMGa), triethylborane (TEB) and NH_3 are used as precursors for aluminum, gallium, boron and nitrogen, respectively. TMG, TMAl and TEB are stored in liquid and TMIn is in solid. The containers, or referred as "bubblers", are maintained in the bath with a set temperature. A certain amount of carrier gas is injected into the bubbler. The vapor phase of the source saturates in the carrier gas, and then it is carried out of the bubbler and delivered into the reactor. So the debit of the sources can be calculated by the following equation:

$$Debit(\mu mol/min) = \frac{N(sccm)}{22400(ml/mol)} \cdot \frac{P_{sat}(Torr)}{P_{bubbler}(Torr)} \cdot 10^6, \tag{13}$$

Table 5: Properties of metal-organic precursors of III elements.

	TEB	TMAl	TMG	TMIn
A/B	$7.413\text{-}\frac{1544.2}{T-27.42}$	8.22/2134	8.07/1703	10.52/3014
Melting temperature (°C)	-93	15	-15	88
Boiling temperature (°C)	95	125	56	134

where N is the flow rate of the carrier gas into the bubblers which is measured and controlled by a mass flow controller in the inlet of each bubbler. $P_{bubbler}$ is the pressure inside the bubbler which is measured and regulated by a pressure regulator. P_{sat} is the equilibrium vapor pressure of the organometallic source, which can be tuned by the bubbler temperature T (K) and has a general form as:

$$P_{sat}(Torr) = 10^{A-B/T}. \tag{14}$$

The parameters used in the calculations and physical properties of precursors are summarized in Tab. 5

The debit of NH_3 flowing into the reactor can be directly calculated from the flow rate:

$$Debit(\mu mol/min) = \frac{N_{NH_3}(slm)}{22.4(l/mol)} \cdot 10^6. \tag{15}$$

Based on the debit of each precursor, the V/III ratio and III/III ratio can be easily obtained.

2.2.2 Characterization techniques

After growth, various kinds of characterization techniques are required for acquiring the properties and the quality of grown materials and devices.

• X-ray Diffraction (XRD)

X-ray diffraction is an effective method to determine composition and provide structural information of single epitaxial layers as well as complex multi-layered structures. The basic principle is the Bragg's law in Eq. 16:

$$2 \cdot d_{hkl} \cdot sin\theta = n \cdot \lambda \ . \tag{16}$$

The incident X-ray would be reflected on a set of crystal planes. If the incident angle θ and the crystal plane distance d_{hkl} satisfy this equation, there would be constructive interference to obtain a diffraction peak. X-ray diffraction allows to analyze accurately the lattice parameters, hence the composition and strain state. The X-ray can also have reflection on top and bottom of each layer, so that it can give an accurate measurement of thickness for thin films or MQWs. Since the dislocations cause small disorientation (tilt or twist) of crystal blocks leading to the broadness of rocking curves, the screw and edge dislocation densities can be estimated by this technique. More details about principles and equations for calculations can be found in Ref. [106].

In this work, high resolution XRD measurements were performed in a Panalytical X'pert Pro MRD system with Cu Kα radiation (Cu Kα1 : 1.5405 Å). The height of X-ray beam from hybrid monochromator is 1.2 mm and the resolution is $\sim$ 12 arcsec.

• Secondary ion mass spectroscopy (SIMS)

Secondary ion mass spectroscopy is a technique used to analyze the composition of solid surface or thin films by sputtering the surface of the specimen with focused primary ion beam, collecting and analyzing ejected secondary ions. The mass/charge ratios of these secondary ions are measured with a mass spectrometer to determine the elemental, isotopic, or molecular compositions [107]. It is a sensitive technique to detect low concentration of atoms such as impurities or dopants. The depth concentration profiles for different elements can be obtained by plotting concentrations versus sputtering depth.

In this work, SIMS was used to determine the content of boron, which is a major element in the alloy. Estimation of major elements composition requires the so-called MCs+ molecular ions (where M is the element to be monitored) technique to minimize the matrix effect. It is necessary to dispose a standard made up of the same alloy whose composition is already known. If the sample to analyze and the standard have very close compositions, the quantification accuracy can be better than one percent [108]. To quantify boron content

in the BAlN layers, the simplified equation can be written as:

$$x/(1+x) = K[B]/[Al] \ , \tag{17}$$

where [B] and [Al] are the Cs+ signals of boron and aluminum, and K is the sensitivity coefficient deduced from the boron implanted standard. The error range by using this method is estimated to be ±5%.

The SIMS measurements in this work have been performed by Probion Analysis located in Bagneux (France).

• Scanning transmission electron microscope (STEM)

A scanning transmission electron microscope is a type of transmission electron microscope (TEM). A beam of electrons is transmitted through an ultra-thin specimen. An image is formed from the interaction of the electrons transmitted through the specimen. Owing to the small de Broglie wavelength of electrons, this technique can examine the lattice of atoms in the crystal. The difference of STEM from conventional TEM is that STEM focuses the electron beam into a narrow spot which is scanned over the the sample in a raster, which makes it suitable for analysis such as energy dispersive X-ray (EDX) mapping, electron energy loss spectroscopy (EELS) and annular dark field imaging (ADF) allowing direct correlation of image and quantitative data [109]. An annular dark field image, which is formed only by very high-angle and incoherently-scattered electrons, is highly sensitive to atomic number variations of the sample (Z-contrast images). By using this high-angle annular dark-field scanning transmission microscopy (HAADF-STEM), the relative intensity variations of the images reflect variations in the compositions of the material. Therefore, HAADF-STEM images can be interpreted into quantitative compositional maps by using EDX as a chemical calibration [110].

To prepare the samples for TEM characterizations, 100 nm carbon were deposited to protect the surface. Then all the thin foils were prepared using focused ion beam (FIB) thinning and ionmilling by Dr. David Troadec in Institut d'Electronique de Microelectronique et de Nanotechnologie (IEMN, Lille, France). Carbon coating and HAADF-STEM

characterizations in this work were performed by Dr. Gilles Partriarche in Laboratoire de Photonique et de Nanostructures (LPN, Marcoussis, France). The equipment for HAADF-STEM is aberration-corrected JEOL 2200FS electron transmission microscope.

• Energy-dispersive X-ray spectroscopy (EDX)

The energy-dispersive X-ray spectroscopy is combined with TEM technique. The X-rays produced when the electron beam impacts the structure are collected and measured by an energy-dispersive spectrometer. As the energies of the X-rays are characteristic of the energy difference between the two shells and of the atomic structure of the emitting element, EDX allows the measurement of elemental compositions of the specimen [111].

• Atomic force microscope (AFM)

Atomic force microscopy is a non-destructive technique to measure the sample surface in nanometer-scale resolution. It consists of a cantilever with a sharp tip typically made of Si_3N_4 or Si. The tip radius of curvature is on the order of nanometers. When the tip is brought into proximity of a sample surface, the interaction forces between the tip and the sample cause a deflection of the cantilever according to Hook's law. This deflection can be measured by the reflection of the laser beam focused on the cantilever [112]. The motion of the probe across the sample surface is controlled by feedback loop and a piezoelectronic scanner moving the sample under the tip.

AFM has three primary modes: tapping mode, contact mode and non-contact mode. The commonly used tapping mode maps topography by lightly tapping the surface with an oscillating probe tip [113]. The oscillation frequency is equal or slightly lower than its resonance frequency. In order to maintain a constant oscillating amplitude, the feedback loop controls vertical position to maintain a constant tip-sample interaction. The vertical position of the scanner is stored to form the topographic image of the sample surface. In contact mode, the spring constant of the cantilever is lower than the effective spring constant holding the atoms of most solid samples together. The contact force on the tip is repulsive. The scanner gently traces the tip across the sample surface. By maintaining a

constant cantilever deflection, an image of the surface is obtained. In non-contact mode, a stiff cantilever vibrates near the surface of the sample with the spacing on the order of tens to hundreds ångstroms. The surface topography can be measured by monitoring changes in the amplitude due to attractive van der Waal forces between the tip and the sample surface. The AFM images in this work were obtained by Veeco 3100 Dimension Atomic Force Microscope.

• Scanning Electron Microscope (SEM)

A scanning electron microscope is a type of electron microscope that produces images of a sample by scanning it with a focused beam of high energy electrons [114]. The electrons interact with atoms in the sample, producing signals of secondary electrons, backscattered electrons, characteristic X-rays, light (cathodoluminescence), Auger electrons, transmitted electrons and phonons (heat). Secondary electrons are low energy electrons emitted by atoms near the surface. The number of secondary electrons depend on the angle at which the beam meets the surface of specimen. By scanning the sample and collecting the secondary electrons with a special detector, the topography of the surface can be displayed. A wide range of magnifications from 10 times to more than 50 k times is possible. High resolution (1 nm at 15 kV) makes it suitable for characterizing nano-structures.

The SEM images in this work were obtained by Zeiss supra^{TM} 55VP. The main elements are: electron source, magnetic focusing lenses, the sample vacuum chamber, imaging system and control panel.

• Cathodoluminescence (CL)

A cathodoluminescence spectroscopy combined with SEM system is used to study optical properties of the sample. The high energy electron bombardment onto a semiconductor will result in the promotion of electrons from the valence band into the conduction band, leaving behind a hole. When an electron and a hole recombine, it is possible for a photon of characteristic wavelength to be emitted [115]. The CL emission is detected via a parabolic mirror collector and analyzed by a spectrometer with a focal length of 320 mm using a 1200

grooves mm^{-1} grating with a spectral resolution of 0.06 nm. The signal is then registered by a liquid N_2-cooled HORIBA JOBIN YVON Instruments Symphony 1024×256 CCD detector.

• Photoluminescence (PL)

The semiconductor sample is excited with a light source that provides photons with an energy higher than the bandgap of the material. The photons will be absorbed and an electron-hole pair will be created. The excited electrons undergo energy and momentum relaxation towards the lowest energy state in the conduction band [116]. Then, the electrons fall back to the valence band and recombine with the holes, emitting photons near the bandgap energy.

The PL experiments are carried out under excitation provided by the third harmonic generation of a Ti-Sapphire femto-seconde pulsed laser (245 nm) or by the second harmonic beam of a continuous laser (266 nm). A continuous-flow cryostat can be used to perform low temperature measurements. The emission was analyzed by a 1 m focal length monochronometer and detected by a CCD camera. The laser beam is focused through a microscope objective to a spot with diameter of approximately 2 μm. These measurements were performed in Institut Pascal - Université Blaise-Pascal (LASMEA, Aubière, France).

• Fourier Transform Infrared Spectroscopy (FTIR) and optical spectrometer

FTIR spectrometer simultaneously collects data over a wide spectral range. An interferometer is applied to encode all the frequencies into a unique type of signal (interferogram) [117]. To interpret and analyze the signal, the individual frequency can be decoded by Fourier transformation. In this work, Fourier transform infrared spectroscopy of Bruker Vertex 80V equipped with a deuterium lamp is used to measure the transmission (absorption) of the MQW structures in visible-DUV range. Absolute reflectance accessory utilizing V-W geometry allows to measure the specular reflectivity of DBR structures. The spectrum obtained by this mode is R^2 (square of the reflectance) versus wavenumber.

The reflectivity and transmission spectrum of MQWs have also be measured by a spectrometer under excitation of a Xenon arc lamp in Institut Pascal UMR 6602 CNRS (LASMEA, Aubère, France). The reflectivity and transmission signals are analyzed through the same monochromator. The size of probed area is around 0.02 mm^2.

CHAPTER 3

MOVPE STUDIES OF BAlGaN MATERIALS

This chapter focuses on the MOVPE growth and characterizations of AlGaN and BAlN materials. The AlGaN material is a promising candidate for UV or DUV devices as well as gas sensors. The novel BAlN exhibits great potentials for lattice, bandgap and refractive index engineering. The studies of basic growth conditions and investigations of material characteristics are required for further growth and fabrication of devices. The thick AlN growth on sapphire in the new Aixtron close-coupled showerhead (CCS) reactor is also presented in this chapter.

The active region of the laser or LED devices consists of AlGaN/AlGaN MQWs for emission at DUV wavelengths. Therefore, a good control over composition and strain state for AlGaN material is the foundation to realize the device design. So the first section of this chapter focuses on the growth of AlGaN layers. The experiments were carried out to establish the relationship between composition - TMAl/III ratio - thickness - relaxation and to investigate the structural quality of the epitaxial layers. The critical thickness of AlGaN on AlN was also calculated by different models.

The second section is concentrated on the growth study of novel BAlN materials, including single layers and BAlN/AlN heterostructures. The BAlN layers with high boron content up to 12% were realized. The influences of growth conditions, the structural features and optical properties were studied.

The AlN/sapphire templates used for the growth of BAlGaN materials and structures were provided by the group of Prof. Dupuis from Center for Compound Semiconductors of Georgia Institute of Technology. The details of the AlN template growth conditions and optimizations can be found in Ref. [118, 119]. The thickness of the AlN layer for the templates used in this work were 900 nm. The quality would be characterized and discussed along with AlGaN layers and MQWs.

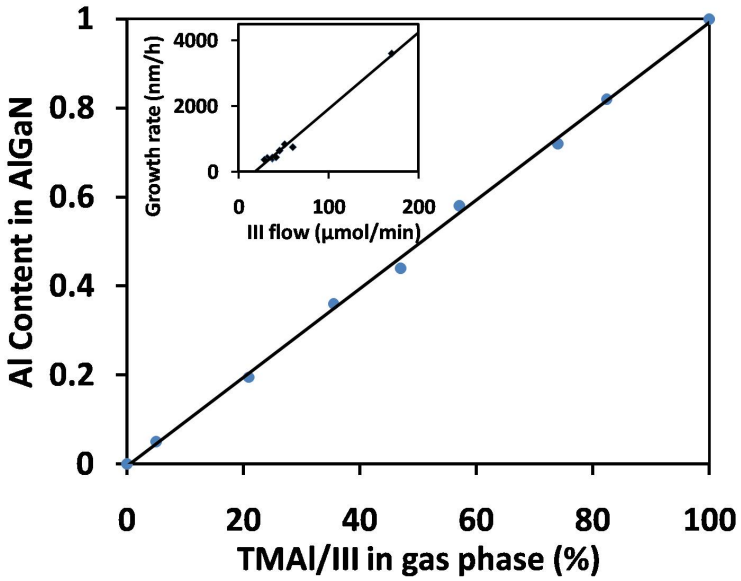

Figure 15: Al composition of AlGaN layers fully-strained on AlN templates versus TMAl/III ratio. The inset shows the growth rate versus total flow rate of (TMAl+TMG).

3.1 MOVPE growth of AlGaN single layers

3.1.1 Control of composition and relaxation

AlGaN single layers were grown on AlN/sapphire templates at 1000 °C under 100 Torr. Hydrogen was used as carrier gas. The composition and strain state (plastic relaxation) were determined by XRD symmetric and asymmetric reciprocal space mappings (RSMs). It was verified for one AlGaN sample from RSM measurements along 6 asymmetric φ reflections of the wurtzite lattice [106], that the tilt disorientation could be neglected in the following XRD spectra analyses. The growth rate was determined from the in-situ reflectance oscillations for thick layers, and by fitting the Pendellosung fringes of $2\theta - \omega$ scans for the thickness of thin layers. The thickness estimation was moreover confirmed by STEM analysis.

For the AlGaN thin layers which are fully-strained on AlN templates, Al composition in the solid phase is almost the same as the TMAl relative concentration in the gas phase (Fig. 15). Additionally, the AlGaN growth rate, shown in the inset, varies linearly with the total III elements flow (TMAl+TMGa) while the V/III ratio remains constant, which indicates that the growth occurs in a mass transport limited regime.

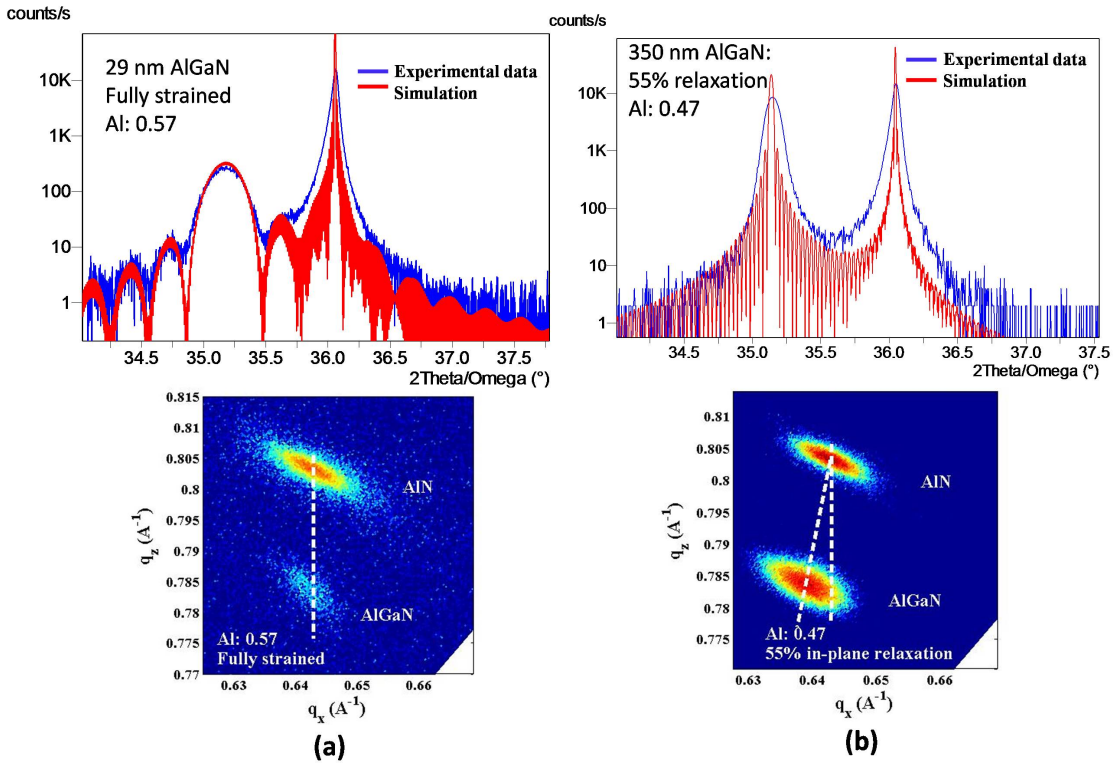

Figure 16: (0 0 0 2) $2\theta-\omega$ scan with simulation and (1 1 -2 4) reciprocal space mapping for (a): 24-nm thick AlGaN fully strained on AlN template and (b): 350-nm AlGaN layer with 55% relaxation on AlN template. Both samples are grown under a fixed TMAl/III ratio of 57%.

However, when the thickness of the single AlGaN layer was increased under the same TMAl/III ratio so that the layer relaxed, it was observed that the average Al content in the layer decreased. As an example, Fig. 16 shows the $2\theta - \omega$ scans and RSMs for the two samples grown under the same TMAl/III of 57% but having different thicknesses: the 29-nm thick AlGaN is fully-strained on AlN template and shows an Al content of 0.57 (± 0.01), while for the 350-nm thick layer, showing a 55% relaxation, the Al content is only 0.47 (± 0.01).

This composition fluctuation during AlGaN relaxation has generally been related to composition pulling effect [120–122]. G.B. Stringfellow et al. explained that the excess lattice mismatch energy would perturb the solid composition towards the composition which

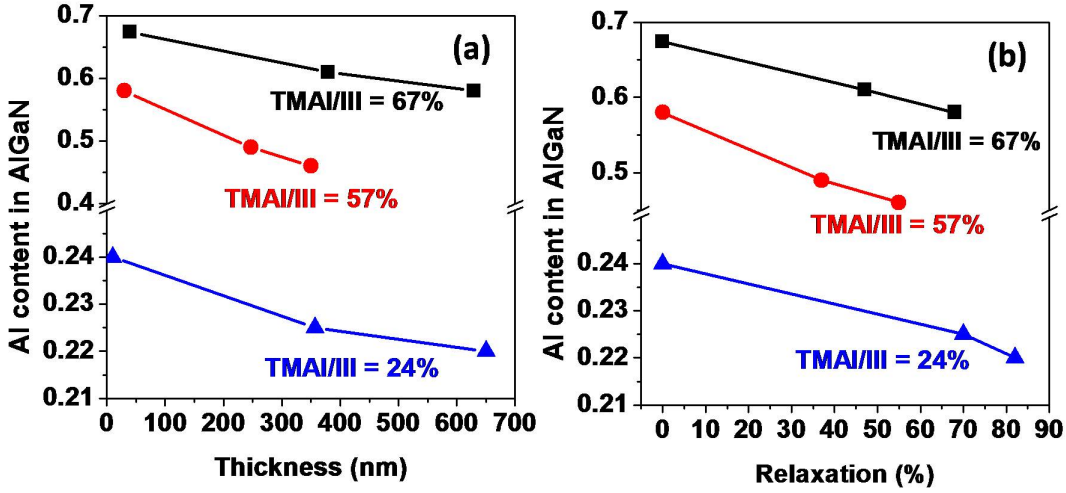

Figure 17: Al content in the AlGaN single layers plotted as a function of (a) layer thickness and (b) corresponding layer relaxation for three different TMAl / (TMAl+TMG) ratios.

minimizes mismatch (composition pulling effect) [123]. The smaller adatoms will be incorporated preferentially at steps having relative compressive strain, and larger adatoms under relatively tensile strain [124, 125]. But very few studies have considered AlGaN layers grown on AlN templates which would be under compressive strain.

In the present investigation, as shown in Fig. 17, a decrease in the Al composition of AlGaN layers is evidenced when the layer thickness (and hence the layer relaxation) is increased. For three different TMAl/III ratios in the gas phase to cover the range of 20% $\sim$ 70% Al, a clear Al content drop can be observed, confirming the composition pulling effect. In our case, AlGaN is under compressive strain on AlN, so in the initial stage when the layer is fully strained, AlGaN has a tendency towards higher Al content so as to minimize mismatch, while for the relaxed layer case, a lower Al content is observed. Since Ga-N has a smaller bond energy than Al-N, Ga incorporation would be more controlled by the strain state than Al incorporation [126, 127], which means that Ga atoms are expelled out for the initial stage under high compressive strain, and Ga incorporation increases when the layer is relaxed with lateral lattice increasing.

This composition pulling phenomenon should be paid attention to, not only for our

application here, but also for all other AlGaN-based devices.

3.1.2 Critical thickness for AlGaN grown on AlN templates

This subsection attempts to predict critical thickness range of AlGaN layers grown on AlN templates by applying different theoretical models reported in the literature.

• **Van der Merwe model (VM)**

The theoretic model of calculating critical thickness of epitaxial layers was first proposed by J.H. van der Merwe [128, 129]. He initially formulated a misfit dislocation theory for critical thickness of strained layers assuming that the crystal would reach thermodynamic equilibrium and settle into the lowest energy state [128]. In brief, the critical relaxation point is where the interfacial energy ϵ_I between the film and the substrate for generating dislocations is equal to the strain energy in the film [6]. The interfacial energy ϵ_I can be expressed by the following equation (for moderate misfit $f \leq 4\%$):

$$\epsilon_I = 9.5 \cdot f \cdot (\frac{Gb}{4\pi^2}) \ , \tag{18}$$

where G is the shear modulus and b is the slip distance (or Burgers vector). The areal strain energy density associated with a film of thickness h is:

$$\epsilon_H = 2G(\frac{1+\nu}{1-\nu})hf^2 \ , \tag{19}$$

where ν is Poisson's ratio. By setting $\epsilon_I = \epsilon_H$, the critical thickness h_c can be obtained:

$$h_c \simeq (\frac{9.5}{8\pi^2})(\frac{1-\nu}{1+\nu})\frac{b}{f} \ , \tag{20}$$

where a_0 is the bulk lattice constant of the substrate.

• **Matthews-Blakeslee mdoel (MB)**

J.W. Matthews and A.E. Blakeslee have proposed Matthews-Blakeslee model for predicting the critical thickness via mechanical equilibrium theory instead of minimizing the total energy of strain and dislocations in a crystal [130].

Figure 18 shows a grown-in threading dislocation in coherent interface (a), critical interface (b) and incoherent interface (c). F_D is the tension in the dislocation line and F_H

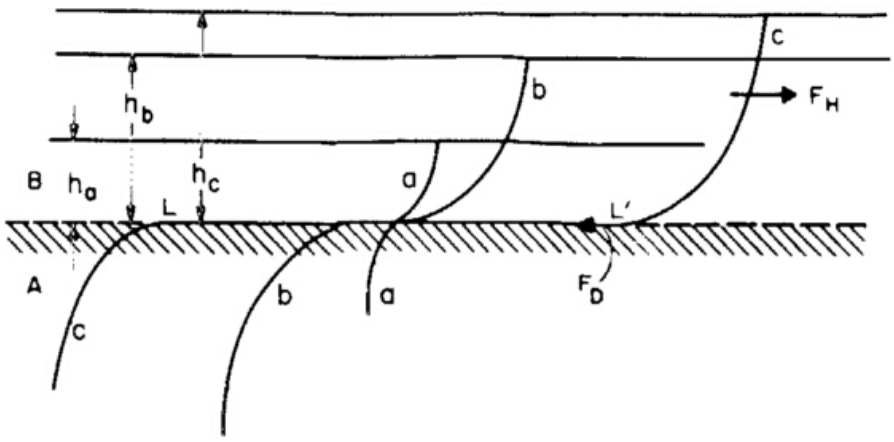

Figure 18: Elongation of a grown-in, threading dislocation to form a length LL' of misfit dislocation line. [6]

is the force exerted on the dislocation line by misfit stress. For the film thickness h_a, the interface is assumed coherent; for the thickness of h_b, the interface is critical ($F_H = F_D$); and for h_c where $F_H > F_D$, the dislocation is elongated in the plane of interface forming a misfit dislocation (MD) line with length LL' [6, 130].

Assuming that the elastic constants of the two media A and B are equal, F_H and F_D are given as:

$$\begin{aligned} F_H &\simeq G(\frac{1+\nu}{1-\nu})bh\epsilon \\ F_D &\simeq \frac{Gb^2}{4\pi(1-\nu)}[ln(\frac{h}{b})+1] \ . \end{aligned} \tag{21}$$

For the critical point: h=h_c and ϵ=f, so the critical thickness can be expressed in the following equation:

$$h_c \simeq (\frac{b}{f})[\frac{1}{4\pi(1+\nu)}][ln(\frac{h_c}{b})+1] \ . \tag{22}$$

By this mechanism, the onset of interfacial misfit dislocations is determined by the mechanical equilibrium of an existing grown-in threading dislocation. It is not expected to be operational when the misfit is small or the substrate has high quality in which case the threading dislocation density is low [6].

- **People and Bean model (PB)**

The PB model is similar to the theory of Van der Merwe in a way that the critical thickness is determined by minimizing total energy in the crystal. It assumes that the growing film is initially free of threading dislocations. The interfacial misfit dislocations will be generated where the strain energy at a certain thickness is equal to the minimum of dislocation energy [6]. Normally screw threading dislocations are considered since they have minimum energy density.

The areal energy density associated with an isolated screw dislocation at a distance h from a free surface is:

$$\epsilon_D \simeq (\frac{Gb^2}{8\pi\sqrt{2}a})ln(\frac{h}{b}) \ . \tag{23}$$

The area strain energy density associated with a film of thickness h is:

$$\epsilon_H = 2G(\frac{1+\nu}{1-\nu})hf^2 \ . \tag{24}$$

The critical point is set to be when $\epsilon_D = \epsilon_H$:

$$h_c \simeq (\frac{1}{16\pi\sqrt{2}})(\frac{1-\nu}{1+\nu})[\frac{b^2}{a}][(\frac{1}{f^2})ln(\frac{h_c}{b})] \ . \tag{25}$$

The critical thickness predicted by PB model can be much higher than the real value in our case, because the AlN template grown on sapphire always has high dislocation density (more than $10^9 cm^{-2}$), which lowers activation energy of relaxation.

• **Fischer model**

The Fischer model considers the elastic interaction between straight misfit dislocations. This method provides an equilibrium theory which predicts the critical thickness of strained layers and describes the strain relief via plastic flow [7]. As shown in Fig. 19, an "image dislocation" is put outside the crystal to satisfy the free surface boundary conditions.

The equation of predicting critical thickness can be described as:

$$h_c \simeq \frac{bcos\lambda}{2f}[1 + \frac{1-\nu/4}{4\pi(1+\nu)cos^2\lambda}ln(\frac{h_c}{b})] \ , \tag{26}$$

where λ is the angle between the Burgers vector and the interface. Here the dominant edge-type dislocations are considered, so the value of λ is assumed to be 0.

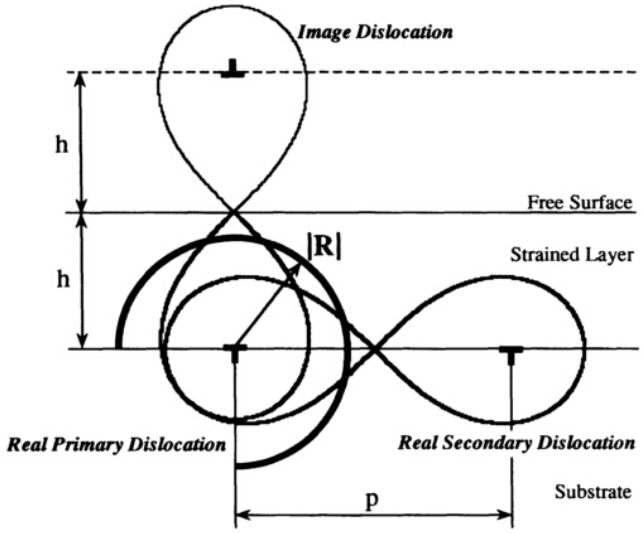

Figure 19: Schematic illustration of the configuration of real and image misfit dislocations in a strained heteroepitaxial structure proposed by A. Fischer et al. [7]

• **Adjusted Griffith model**

Griffith model is normally used to describe the brittle fracture [131]. The AlGaN layers grown on AlN templates are under compressive strain which will not be relaxed by forming cracks. But the simple relationship between critical thickness h_c and misfit strain ϵ from Griffith model can be used:

$$h_c \propto \frac{1}{\epsilon^2} \ . \tag{27}$$

The previous work by M. Abid has succeeded in giving an experimental curve of critical thickness for AlGaN layers grown on GaN templates [9]. The starting point was the Griffith model and the intrinsic parameters were adjusted according to the experimental data. The obtained critical thickness h_c and misfit strain ϵ can be expressed as the formula of composition of Al (x):

$$\begin{aligned} h_c &\simeq 5.3321 x^{-2.051}, \\ \epsilon^2 &= \left(\frac{3.122x + 3.189(1-x) - 3.189}{3.189}\right)^2 . \end{aligned} \tag{28}$$

In our case, $Al_yGa_{1-y}N$ grown on AlN templates has a compressive strain, and the

Table 6: Parameters used for the estimation of critical thickness.

	AlN	GaN	$A_xGa_{1-x}N$
ν	0.203 [106]	0.183 [106]	0.183+0.02x
Misfit of $Al_xGa_{1-x}N$/AlN	0.0215(1-x)		
Lattice a	3.122	3.189	3.189-0.067x

sqaure of the misfit strain is:

$$\epsilon^2 = (\frac{3.122y + 3.189(1-y) - 3.122}{3.122})^2 \ . \tag{29}$$

So the critical thickness for $Al_yGa_{1-y}N$ grown on AlN templates would be:

$$h_c \simeq 5.3321[1.02(1-y)^{-2.051}] \simeq 5.439(1-y)^{-2.051} \ . \tag{30}$$

The parameters (Poisson ratio ν, misfit f and lattice a) used in the calculations are summarized in Tab. 6. For AlGaN/AlN system, two plastic relaxation mechanisms have been proposed in the literature [132]: a-type (edge) treading dislocations (TDs) with Burgers vector $\boldsymbol{b}$ = 1/3<1 1 -2 0> from the AlN substrate are inclined toward the <1 -1 0 0 > directions when entering the AlGaN film, or mixed type TDs with Burgers vector $\boldsymbol{b}$ = 1/3<1 1 -2 3> glide on {0 -1 1 1} planes bend along the <-2 1 1 0> directions to generate misfit dislocations. In the AlN templates used, the edge type treading dislocations are dominant of which the details can be found in the following subsection. So the first process were considered in the calculations, except that in the PB model the Burger's vector of screw threading dislocations $\boldsymbol{b}$ = <0 0 0 1> was used. The curves of critical thickness versus Al content calculated based on different models are shown in Fig. 20

Although the critical thickness predicted by different models has a large dispersion, the calculations give a range of the possibilities. If the experimental data are located in the figure, the critical thickness is more or less close to the curve of adjusted Griffith model compared with the others, which can be used as a reference for a rough estimation of critical thickness.

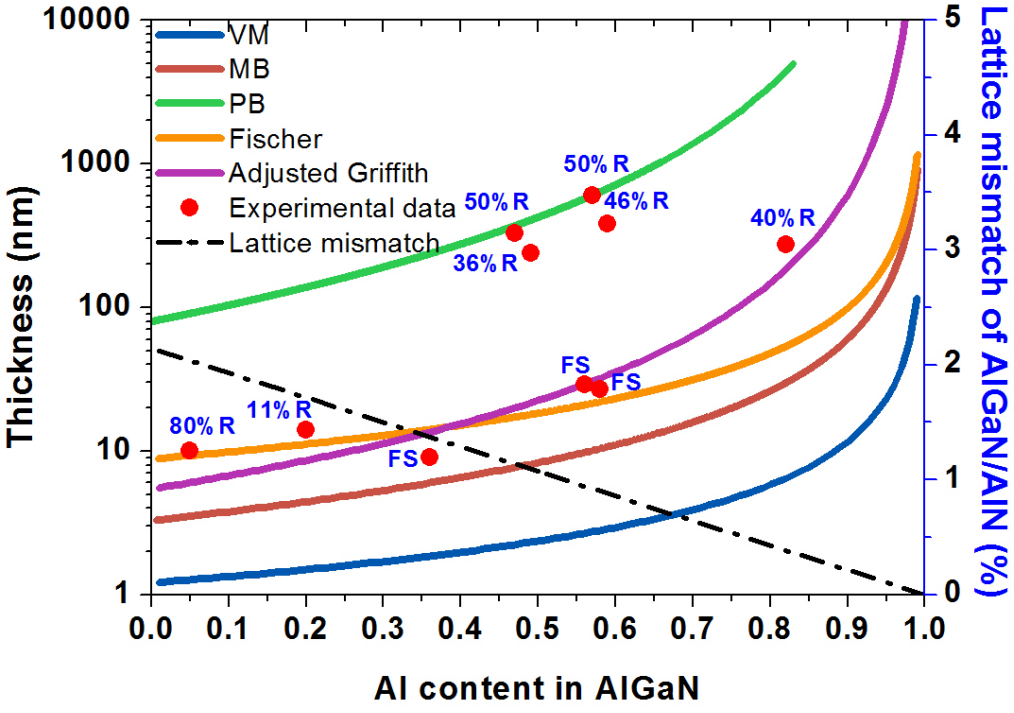

Figure 20: Critical thickness of AlGaN layers grown on AlN templates calculated by different models along with experimental data.

It should be noted that the process of misfit strain relaxation of AlGaN on AlN is complex with various different mechanisms. For example, if the substrate has very low dislocation density (<10^5 cm^{-2}), AlGaN can not relax effectively by the sparseness of pre-existing dislocations and alternative pathways of elastic surface roughening or misfit dislocating may take over [133]. Surface roughening can relax partially the misfit strain by purely elastic deformation of the film and substrate. At large misfit, the surface becomes rough enabling easy nucleation of dislocations. But this mechanism is kinetically unfavorable at low misfit, because the strain already relaxes by nucleation or movement of dislocations before the surface has enough strain to roughen [134].

3.1.3 Estimation of threading dislocation densities by XRD

[0 0 0 1] oriented III-nitrides normally contain three types of threading dislocations (TDs): a-type (edge) with $\boldsymbol{b}$ = 1/3<1 1 -2 0>, c-type (screw) with $\boldsymbol{b}$ = <0 0 0 1> and a+c type (mixed) with $\boldsymbol{b}$ = 1/3<1 1 -2 3>. Each dislocation type accommodates a lattice distortion. Edge TDs lead to a lattice twist, screw TDs lead to a lattice tilt and mixed TDs contributes to both.

In order to study the structural quality of substrates, epitaxial layers or devices, XRD is an effective and non-destructive method, which is not only for determination of composition but can also provide information on threading dislocation densities in the layers including both edge and screw types (components). ω-scans of symmetric planes can measure quantitatively the lattice tilt from screw TDs or screw component of mixed TDs. Twist caused by edge TDs or edge component of mixed TDs should be measured by skew symmetric ω-scans, because asymmetric ω scans are sensitive only to tilt [106]. FWHM (full width at half maximum) of a skew symmetric rocking curve is broadened by both tilt and in-plane twist, so a series of skew symmetric rocking curves for different planes (different inclination angle χ) should be done to separate tilt angle and twist angle, as expressed in

Table 7: Threading dislocation densities of AlN templates and AlGaN layers determined by XRD rocking curves (FWHM determination and linear fitting lead to an estimated error of 15%).

Type of TDs	AlN	29-nm $Al_{0.57}Ga_{0.43}N$	630-nm $Al_{0.58}Ga_{0.42}N$
Screw TDs (cm^{-2})	$\sim 9.0 \times 10^9$	$\sim 6.7 \times 10^9$	$\sim 5.6 \times 10^9$
Edge TDs (cm^{-2})	$\sim 2.7 \times 10^{11}$	$\sim 1.6 \times 10^{11}$	$\sim 1.5 \times 10^{11}$

Eq. 31, which is particularly useful for high defective layers such as AlN [106, 135]:

$$\beta^2 = (\beta_{twist}^2 - \beta_{tilt}^2) sin^2\chi + \beta_{tilt}^2 \ , \tag{31}$$

where β is FWHM angle of the skew symmetric rocking curve, β_{tilt} and β_{twist} are the tilt and twist spread, and χ is inclination angle between the reciprocal lattice vector and the c axis.

Then, the densities of screw TDs and edge TDs may be estimated by Eq. 32

$$\begin{aligned} N_{screw} &= \beta_{tilt}^2/(4.35 \times b_c^2) \\ N_{edge} &= \beta_{twist}^2/(4.35 \times b_a^2) \ , \end{aligned} \tag{32}$$

where the Burgers vector of screw type TDs (b_c) and edge type TDs (b_a) can be seen equal to the lattice c and lattice a of the material.

Skew symmetric rocking curves have been done for AlN/sapphire template, 29-nm $Al_{0.57}Ga_{0.43}N$ layer and 630-nm $Al_{0.58}Ga_{0.42}N$ layer in order to investigate the quality of the substrates and epitaxial layers. b_c is 0.4982 nm for AlN and 0.5067 nm for $Al_{0.58}Ga_{0.42}N$, and b_a is 0.3112 nm for AlN and 0.3144 nm for $Al_{0.58}Ga_{0.42}N$. The measured data to identify tilt and twist angle are shown in Fig. 21, and TD densities are summarized in Tab. 7

The results confirm that the thin and thick AlGaN layers are grown without generating extra threading dislocations that would propagate into MQWs. Some annihilation of dislocations originating from the AlN template may even happen during the growth of the thick buffer layer, which could explain the reduced FWHM of the rocking curves.

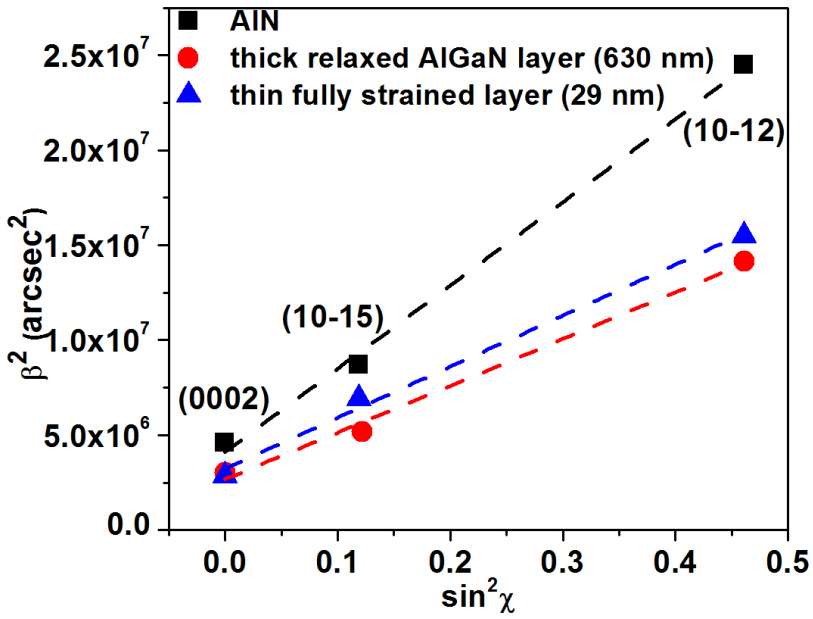

Figure 21: Skew symmetric scans for of AlN template, 29-nm $Al_{0.57}Ga_{0.43}N$ and 630-nm $Al_{0.58}Ga_{0.42}N$.

3.2 MOVPE growth of BAlN with high boron content

Compared with conventional AlGaInN system, Boron containing III nitrides are quite new in this family. They are suitable for DUV applications because of their wide bandgaps, and they can bring additional freedom in engineering the bandgap, lattice constant and refractive index of multi-layered devices. Most of the studies concentrate on BAlN single layers with only 1~2% boron. High boron containing layers grown by MOVPE have not been progressed a lot. This section describes the growth and characterizations of BAlN layers or heterostructures with high boron incorporation. The properties of the materials are studied and discussed.

3.2.1 BAlN/AlN grown at 1000 °C

The fabrication of BAlN/Al(Ga)N heterostructures is an important issue which needs to be further developed no matter for BAlGaN-based MQWs or for DBRs. BAlN/Al(Ga)N

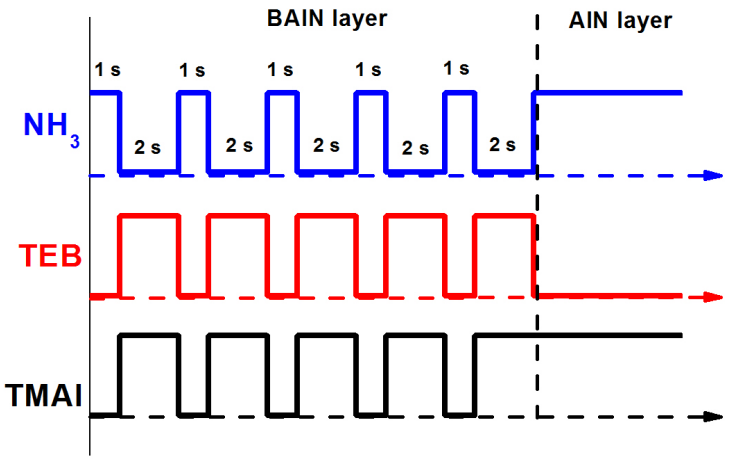

Figure 22: Schematic of precursors feeding sequence for BAlN and AlN.

heterostructures were grown at 1000 °C by both flow-modulate epitaxy (FME) and conventional continuous method. The experiments were performed in T-shape reactor at 100 Torr by using hydrogen as carrier gas. In this subsection the samples by FME method are analyzed in details, and the results of this part can also be found in Ref. [136]. The structural quality of the heterostructures grown by continuous method is investigated in the subsection 5.4.1 for DBRs.

The samples consist of 5-period AlN/BAlN layers (25 nm / 32 nm) on two types of substrates: 1 μm AlN templates on sapphire and 3 μm GaN templates on sapphire. The AlN templates are appropriate substrates for deep UV applications while GaN templates were used as reference. The temperature was maintained at 1000 °C during the growth and TEB/III molar ratio in the vapor phase was 39% in order to have high boron incorporation. Flow-modulate epitaxy (FME) was applied during the growth of BAlN layers in order to enhance the migration of B and Al atoms and also to suppress parasitic reactions [72, 75, 81]. 2 s supply of metalorganics and 1 s supply of NH_3 were alternatively run into the reactor without interruption. The AlN layers were grown in a continuous way. The schematic of precursor feeding sequence for BAlN and AlN is presented in Fig. 22.

3.2.1.1 Structural characterizations

The boron concentration in the BAlN layers along growth direction was evaluated by SIMS profile, as shown in Fig. 23(a). It was clear that B profile varies anti-phase with Al, which indicates that boron atoms substitute aluminium atoms on the III sites of the lattice to form an alloy. 5-period AlN/BAlN structure exhibits good uniformity except that the first AlN layer has lower AlN intensity which is due to some Ga contamination from the sample holder and the reactor [137]. It should be pointed out that the boron signal cannot be zero when it is sputtered into AlN layer considering SIMS detection limit when thin layers are analyzed. In order to calibrate SIMS signal for quantitative measurements of boron content in the layer, boron implanted AlN sample was used as a reference. The boron content distribution along the growth direction is presented in Fig. 23(b). Under our growth conditions, 11% (± 0.6%) boron incorporation has been obtained.

In order to investigate structural quality of this heterostructure and also crystalline characteristics, the cross-section STEM was performed along ⟨1 1 -2 0⟩ zone axis. As shown in Fig. 24(a), the bright-field STEM image shows that the AlN/BAlN heterostructure has columnar polycrystalline features, such as the part in the rectangle box. By looking into the higher magnification image of the interface between 1^{st} AlN and 1^{st} BAlN in Fig. 24(c), it is clear that the 1st AlN layer is still monocrystalline. When BAlN (with 11% boron) growth starts, the lattice is oriented along c-axis for around 5 nm, and then the tilt as large as 60° can be observed that means the structure tends to be polycrystalline and columnar growth starts. Better contrast of AlN and BAlN layers can be observed by Z-contrast HAADF-STEM image shown in Fig. 24(b), where layers with higher brightness represent AlN layers and darker layers represent BAlN. The surface roughness height caused by this columnar feature is around 10∼13 nm from STEM images.

The polycrystalline feature has been confirmed by HR-XRD results. In 2θ-ω scans shown in Fig. 25, a peak related to AlN (0 0 0 2) was located at 36.02 °. Another peak at 37.98 ° should correspond to AlN (1 -1 0 1). Combined with STEM results, it can be

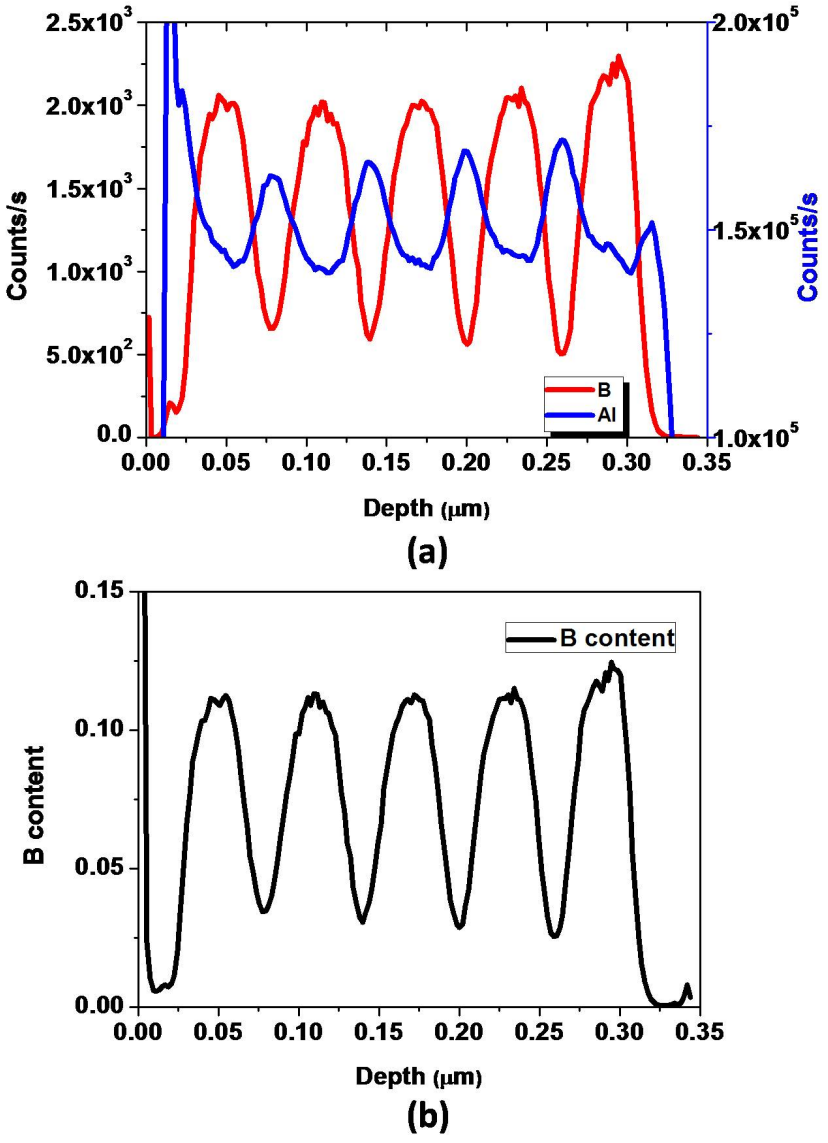

Figure 23: (a) SIMS elemental concentration depth profiles of B and Al for the sample grown on GaN template; (b) Boron content in solid layers calculated from SIMS by using boron implanted AlN sample as reference.

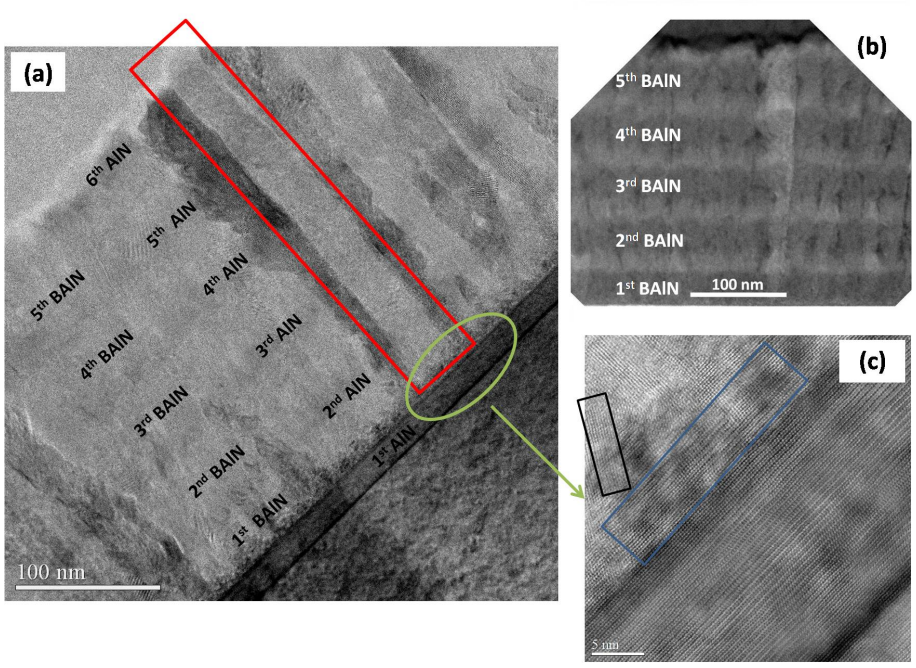

Figure 24: (a) STEM images (bright field) of 5-period AlN/BAlN heterostructure and columns are clearly observed in the structure; (b) HAADF-STEM image to show better contrast of BAlN and AlN layers; (c) high magnification of the zone where the 1^{st} BAlN layer starts to grow.

explained that the first AlN layer was monocrystalline along c-axis. After the BAlN starts to growth, the structure becomes polycrystalline and epitaxial AlN layers grown afterwards also have lattice tilt so that x-ray diffraction signal from other facets arises. BAlN XRD peak is absent due to its polycrystalline feature especially with high boron incorporation.

This AlN/BAlN heterostructure has total thickness of 310 nm. The morphology was examined by AFM shown in Fig. 26. The surface was covered by columnar crystallites confirming the STEM observations. The AFM scan area is 5 μm $\times$ 5 μm square. The structure has root-mean-square (RMS) of 3.3 nm. The average height of these columnar crystallites is around 10 nm which is in a good agreement with estimations from cross-section STEM images.

The polycrystalline feature is caused by the short diffusion length of boron atoms, which would challenge the applications of this material. From STEM image, it was observed that the monocrystalline critical thickness for BAlN with 11% boron is around 5 nm, above

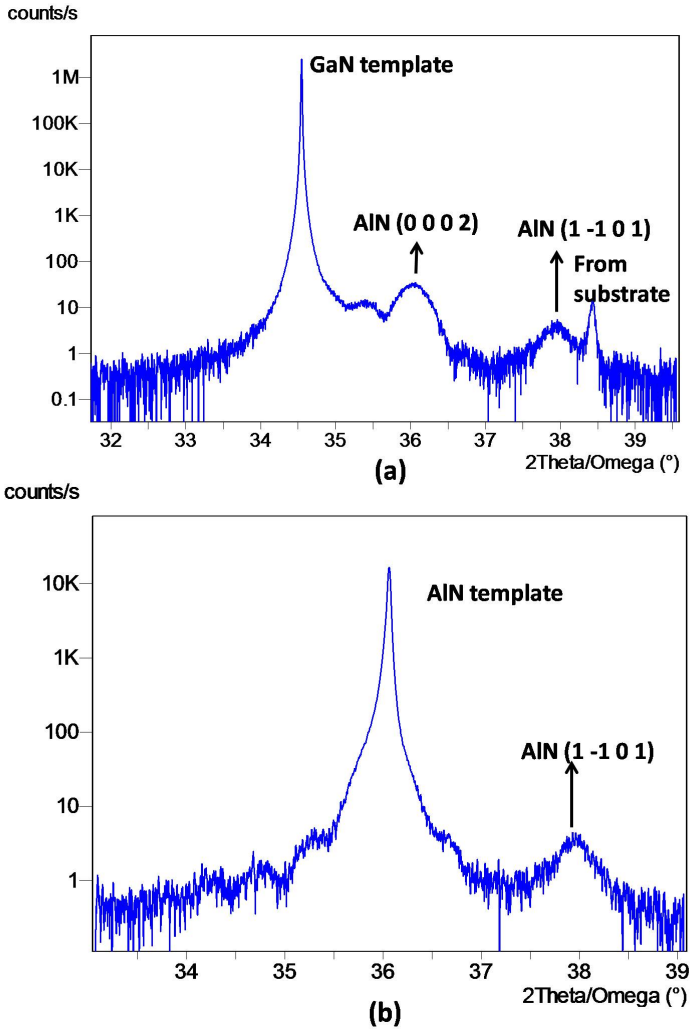

Figure 25: HR-XRD 2θ-ω scans of 5-period AlN/BAlN heterostructure grown on (a) GaN template and (b) AlN template.

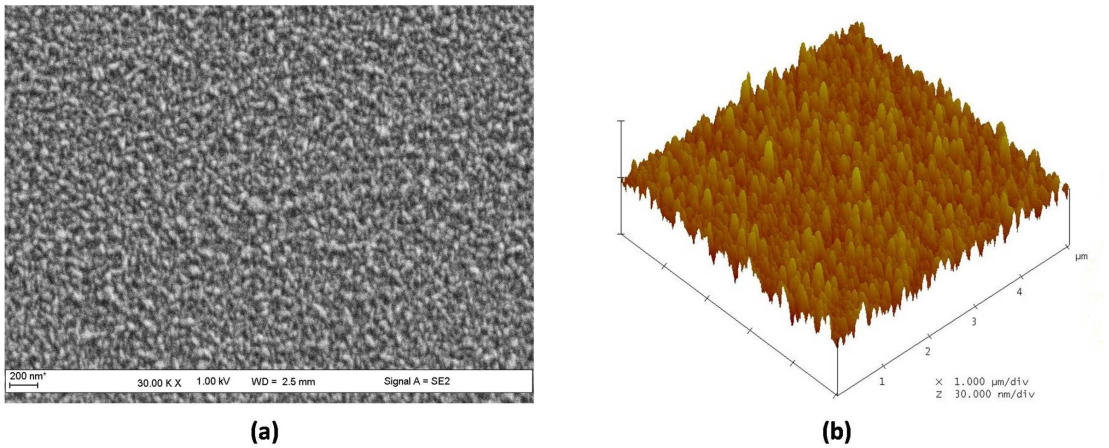

Figure 26: (a) SEM and (b) AFM images of 5-period AlN/BAlN heterostructure (310 nm for total thickness).

which the polycrystalline growth occurs. Meanwhile, the monocrystalline critical thickness is around 500 nm for BAlN of 2% boron as reported in the literature [72]. The more boron is incorporated, the smaller monocrystalline thickness of BAlN is. Therefore, for different applications, a compromise can be achieved between thickness and boron composition. For example, for deep UV DBRs, boron incorporation no more than 5% is enough to achieve high refractive index contrast theoretically [63, 64]. So it can be an option to reduce the boron content and maintain BAlN layers (30~40 nm) monocrystalline. For ultra-thin layers such as MQWs or strain engineering superlattices, higher boron incorporation can be used allowing a large design freedom and it can still be kept as monocrystalline for its thin thickness (below 10 nm).

3.2.1.2 Optical characterizations

In order to study optical properties of this heterostructure containing high boron, Cathodoluminescence (CL) and transmission spectra have been performed for the sample grown on AlN template. As shown in Fig. 27, a well-defined emission peak at 262 nm emerges when the excitation power is above 7 keV. Meanwhile, as shown in Fig. 28, the optical absorption occurred at 260 nm which agrees well with CL results. For the wavelengths longer than 290 nm, the oscillation level of transmission fraction keeps constant, which implies that there

is very less absorption by defects in this region. The results obtained exhibit potentials to apply this material and structure for UV and deep UV devices.

It is noted that CL emission peak of AlN has not been detected due to limitation of our detector below 210 nm. In addition, since emission wavelength of BAlN is at 260 nm, the emission around 200 nm of AlN would be absorbed by the BAlN layers. As shown in Fig. 28 of transmission curve, there is a transmission drop at 260 nm, and below 260 nm, there is a large absorption.

Until now, few results have been reported on optical properties of BAlN material, especially for high boron containing layers. Theoretical calculations show that BAlN has strong bowing parameter (5.45 eV) [86], and for BGaN material the value of 9.2 eV has been experimentally obtained [74]. Based on this prediction, our BAlN layers should give an emission at around 225 nm. Here a significant redshift of wavelength was observed which might be due to high concentration of carbon impurities incorporated from TEB precursors (carbon density about 2×10^{19} cm^{-3} by SIMS). The optical properties of BAlN requires more experimental investigations.

3.2.2 BAlN grown at low temperature with annealing

In the last subsection, the high boron content of BAlN grown at 1000 ° was determined by SIMS. No XRD peak related to the BAlN material was found. High boron content was also demonstrated in the literature [69], but the related XRD peak intensity was very weak. The objective of this subsection is to study the influences of growth conditions, especially the growth temperatures, in order to improve the crystallinity to have clear XRD peaks of BAlN layers [138].

3.2.2.1 Influence of growth temperature

BAlN layers were grown at 100 Torr by using hydrogen as carrier gas. The growth was performed on two types of substrates: 1 μm AlN templates on sapphire and 3 μm GaN templates on sapphire. As shown in Fig. 29, the substrates were annealed in hydrogen at

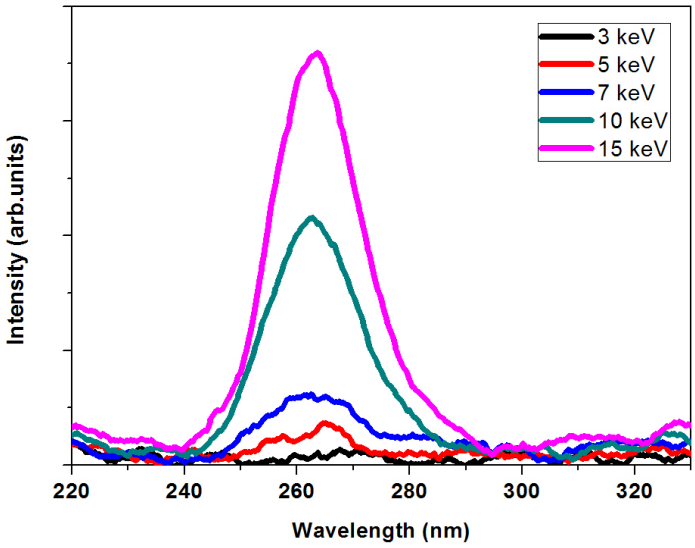

Figure 27: Cathodoluminescence spectra at 77 K of 5-period AlN/BAlN heterostructure grown on AlN template.

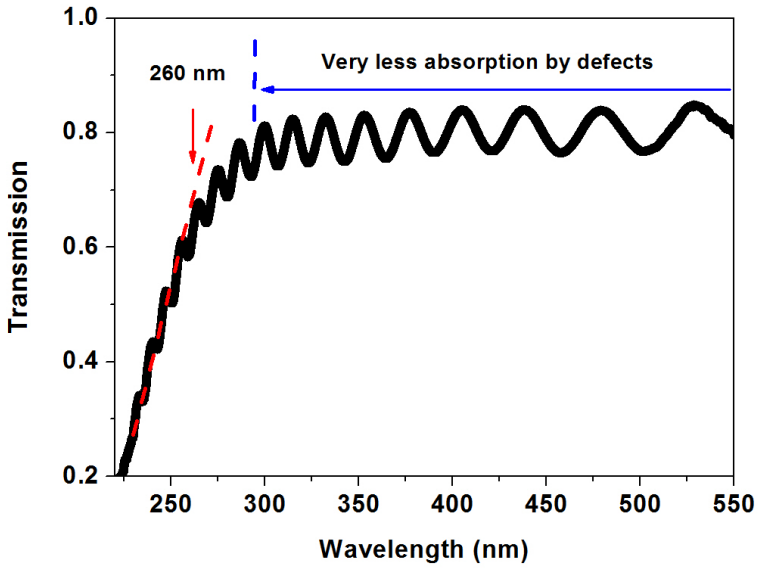

Figure 28: Transmission spectrum at room temperature of 5-period AlN/BAlN heterostructure grown on AlN template.

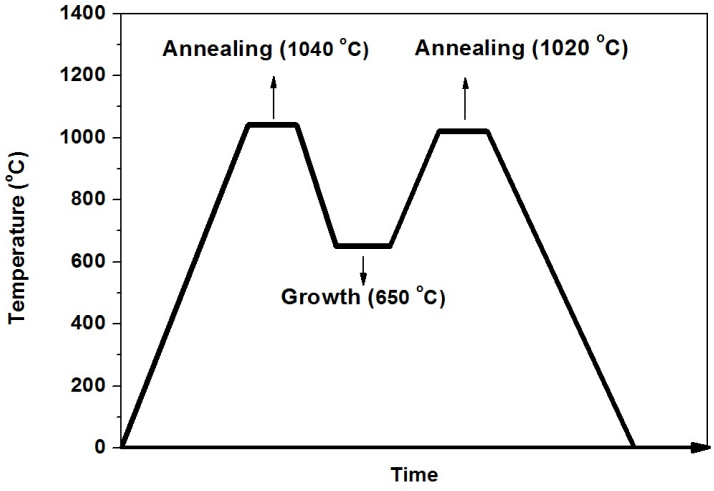

Figure 29: Schematic of growth procedure.

1040 °C prior to growth. Thin BAlN layers were grown in a continuous way at low temperatures, which were varied from 650 to 800 °C to study the influences. Then the temperature was ramped up to 1020 °C and the samples were annealed for 5 min before cooling down. A large flow rate of NH_3 (2.3 slm/min) was used due to inefficient decomposition of NH_3 at low temperature. Under high TEB/III ratio of 39%, as shown in Fig. 30(a), BAlN single layer grown at 650 °C with 20 nm thickness demonstrates an X-ray diffraction peak at 36.38 ° (± 0.17 °), which indicates that the layer has a smaller lattice c than AlN due to boron substituting Al atoms in the crystal structure. It is assumed that the layer is fully relaxed considering the large lattice mismatch between BAlN layer and GaN template. In this case, the c-lattice constant is 4.935 Å (± 0.022 Å), which corresponds to boron composition of 5.6% (± 2.8%) by applying Vegard's Law. The complete relaxation of the layer can be confirmed in Fig. 31; when TEB flow is stopped for growing AlN layer, the 2θ-ω peak of the layer is located at 36.02 ° corresponding to completed-relaxed AlN layer.

When the deposition temperature is increased, shown in Fig. 30(b), the BAlN peak is weakened, and then disappears when it is increased to 800°C. It indicates that under this high TEB/III ratio the crystallinity is worse when the layer is grown at higher temperature. Low temperature growth can alleviate the B-rich phase poisoning issue under high TEB/III

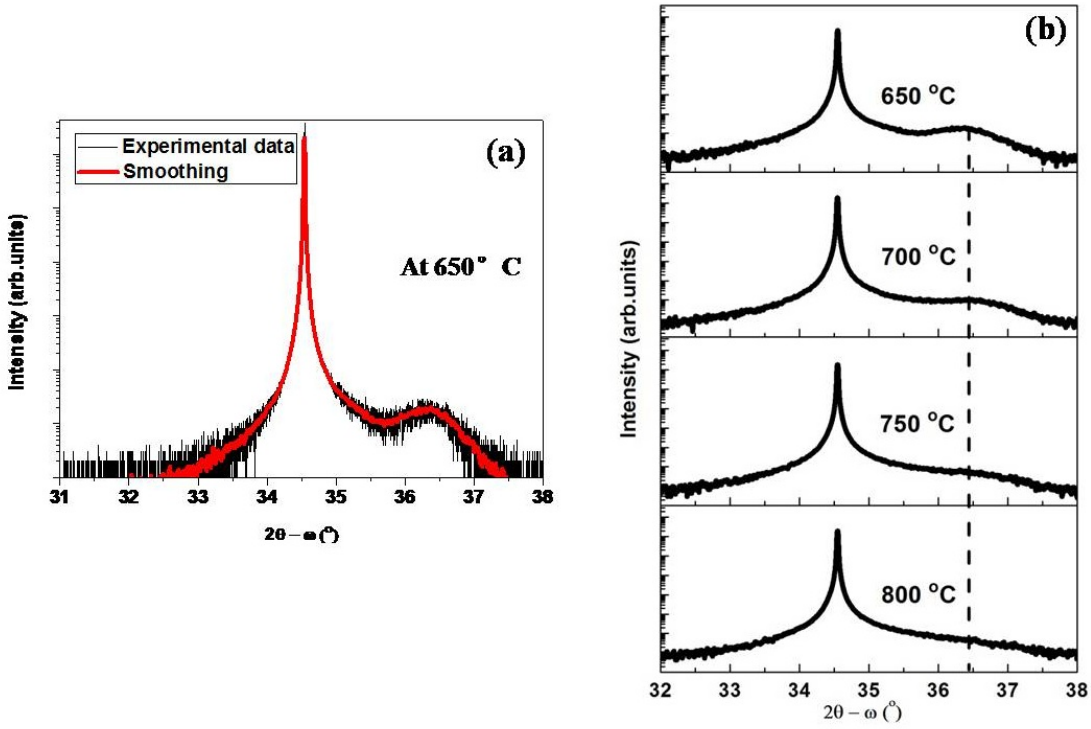

Figure 30: (a) HR-XRD 2θ-ω scan of 20 nm BAlN layers grown on GaN template at 650 under TEB/III=39%; (b) shows the influence of growth temperatures which was varied from 650 °C to 800 °C .

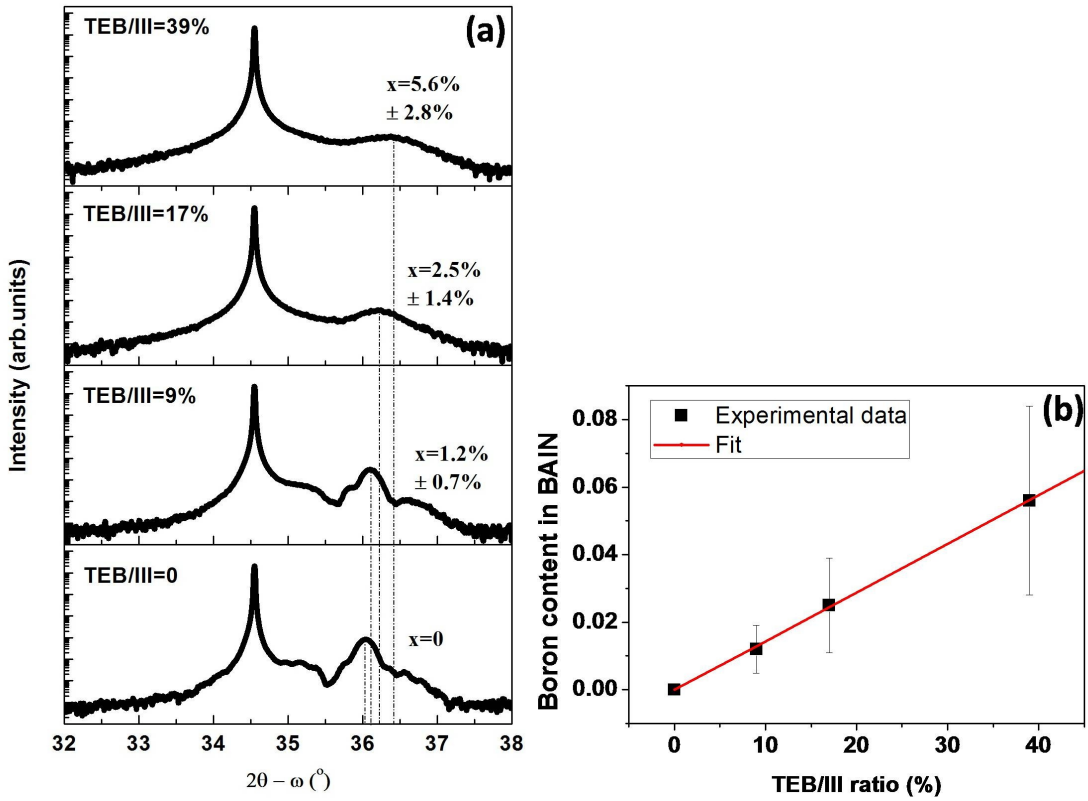

Figure 31: HR-XRD 2θ-ω scan of 20 nm BAlN layers grown on GaN templates by continuous method under different TEB/III ratio.

ratio. So the following results in this subsection are all referred to the growth at 650 °C.

3.2.2.2 Influence of TEB/III ratio

In order to have a different amount of boron incorporation, the flow rate of TMAl was maintained constant while flow rate of TEB was varied to have TEB/III molar ratio in the vapor phase of 0%, 9%, 17%, and 39%, respectively. As shown in Fig. 31(a), when TEB/III ratio is increased from 0 to 39%, the peak of the layer shifts gradually towards greater diffraction angles (0 to 5.6% boron). The peak is broadened with fringes missing due to polycrystalline nature of BAlN, which will be discussed later. Figure 31(b) shows that boron content in solid phase has almost a linear relationship with TEB/III ratio in the gas phase. The morphology change was studied by AFM in Fig. 32. As observed, without boron incorporation, 40 nm AlN layer on GaN template exhibits normal V-defects and

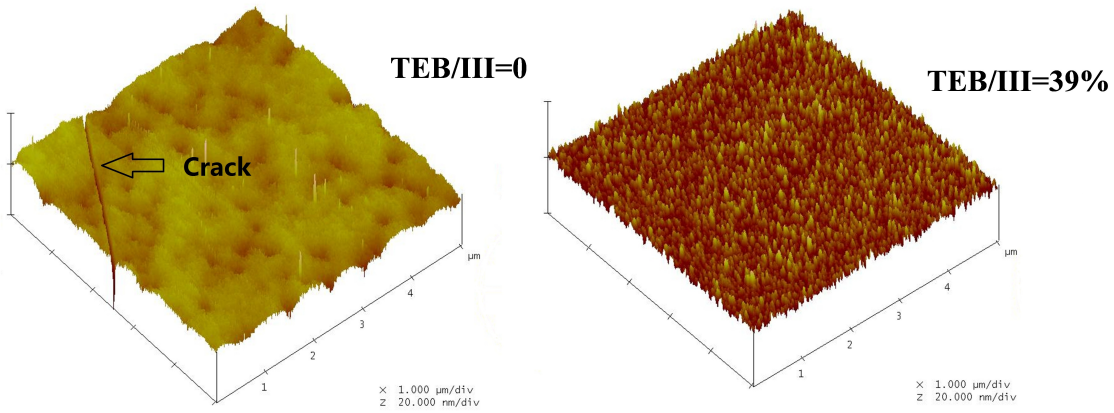

Figure 32: AFM images of 40 nm BAlN layers grown on GaN templates under TEB/III ratio of 0% and 39%.

cracks generated by lattice mismatch. The flat area be-tween defects has surface roughness around 0.7 nm. When boron was incorporated, the surface became rough, and cracks and v-defects disappeared. The surface is covered by small crystallites caused by columnar growth of BAlN, and this columnar feature would be clearly observed by STEM results. Surface roughness was around 1.2 nm for TEB/III=39% (~5.6% boron in solid phase).

3.2.2.3 BAlN on AlN by FME

For BAlN layers grown on AlN templates by continuous flow, the XRD peak of BAlN layer was too weak and it cannot be distinguished from noise. So FME method was applied to improve the crystalline quality. The same feeding sequence in Fig. 22 was used. BAlN single layers with clear defined X-ray diffraction peaks were also achieved on AlN templates which are appropriate substrates for deep UV devices, as well as on GaN templates, in order to distiguish the XRD peak of BAlN from the substrate peak. As shown in Fig. 33, clear XRD peaks can be identified at 36.59 ° (± 0.20°) on both GaN and AlN templates. Lattice c is 4.908 Å (± 0.025 Å) and the corresponding boron content is 9% (± 3.2%). Since BAlN peak is very close to AlN template peak, the deconvolution of substrate peak and layer peak is shown in the inset figure.

The concentration calculated by XRD has a large error range because of the broadness

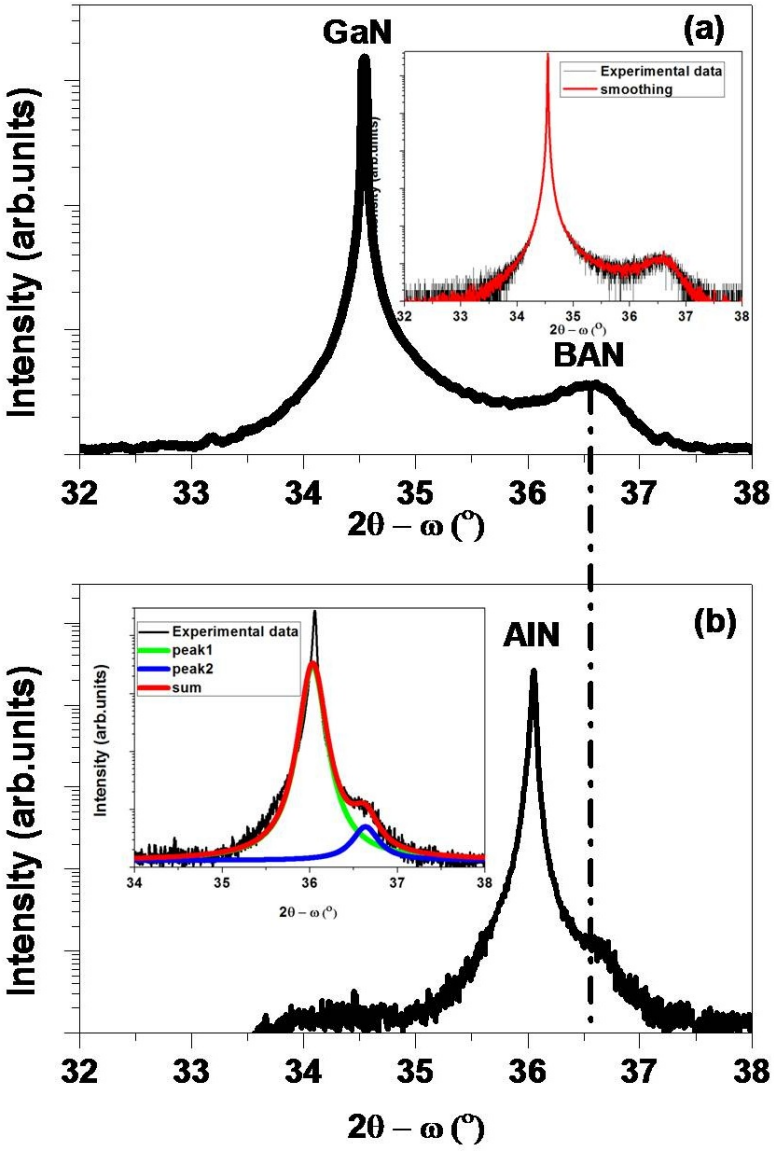

Figure 33: HR-XRD of 70 nm BAlN on (a) GaN template and (b) AlN template by FME growth (TEB/III=39%). Inset figures show the smoothing and deconvolution of two peaks.

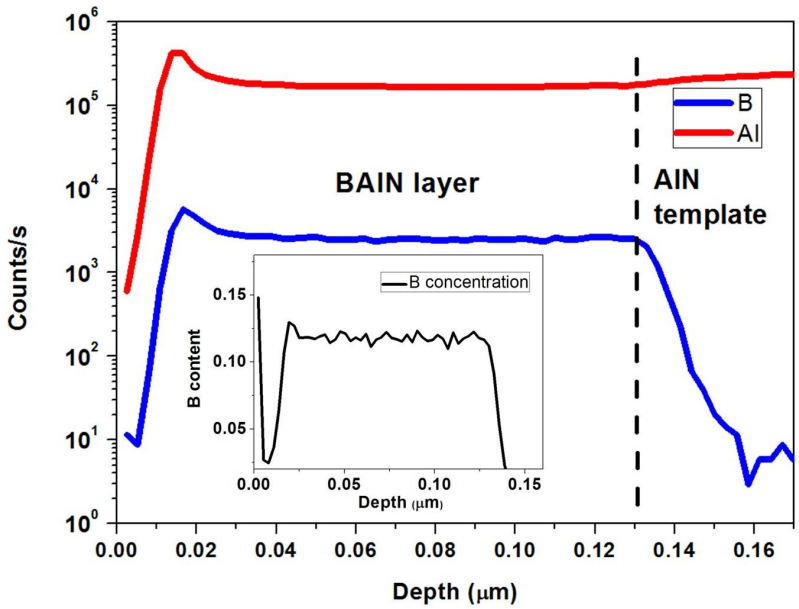

Figure 34: SIMS elemental concentration depth profiles of B and Al for the sample grown on AlN template; inset shows the boron concentration obtained by using boron-implanted AlN as calibration sample.

of the BAlN diffraction peak and uncertainty of the lattice parameters and strain. These all influence calculation of the composition from X-ray diffraction peak positions, especially for the layer with high boron content. So the boron incorporation into the layer was also analysed by SIMS profile along the growth direction in Fig. 34. The Al signal is decreased in the BAlN layer compared with the signal of the template indicating that boron atoms were substitutionally incorporated into AlN lattice. Boron has a uniform distribution along the growth direction. The concentration of boron can be calculated based on atomic concentration obtained by SIMS with a boron-implanted AlN sample as a reference. The concentration of boron calculated from the SIMS signal is 12% with 0.6% error (inset of Fig. 34), which agrees with the composition range given by XRD diffraction peak positions (6% $\sim$ 12%). STEM characterizations were also performed to study the crystallinity of the layer. Cross-section image in Fig.35 shows that BAlN layer has a columnar crystalline growth feature. At the beginning of BAlN growth, the lattice is still oriented along c-axis (the zone A). After around 10 nm, the crystals start to disorient and form columns (zone

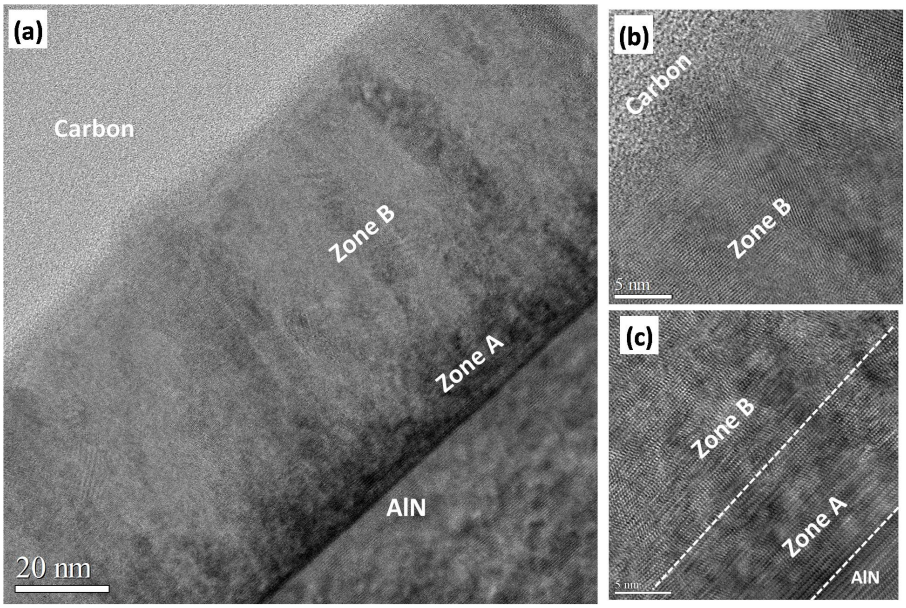

Figure 35: (a) Cross section STEM image (bright field) of 75 nm thick BAlN layers containing 12% boron along the [1 1 -2 0] zone axis. Zone A has lattice oriented along c-axis and Zone B has columnar feature; (b) higher magnification image for the top part of the layer; (c) higher magnification image for the film/substrate interface.

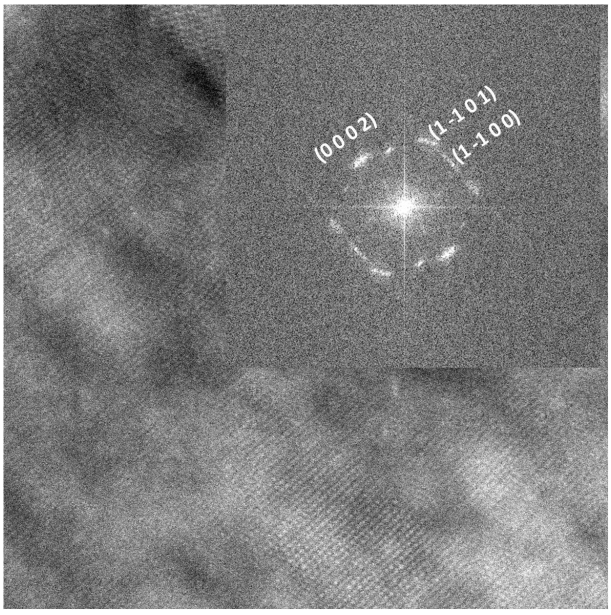

Figure 36: Cross section High-angle Annular Dark Field Scanning Transmission Microscopy (HAADF-STEM) image of 75 nm BAlN layer containing 12% boron; inset shows diffraction pattern after Fast Fourier Transform (FFT).

B). The monocrystalline thickness is higher than the one grown at 1000 ° by FME. The lattice of columnar crystals can be clearly observed in Fig. 35 (b) which is the top part of the layer. This columnar growth feature would lead to surface roughness, as observed in AFM analysis.

Fig. 36 presents HAADF-STEM image of the BAlN layer and diffraction pattern after fast Fourier transform (FFT). It exhibits mainly the typical pattern of the wurtzite crystal along the <1 1 -2 0> zone axis, even though the diffraction spots are elongated due to the different tilts of columnar polycrystals.

3.3 MOVPE growth of AlN/sapphire templates in CCS reactor

The key factor for increasing IQE of DUV MQWs is to reduce dislocation density of AlN substrates. AlN native bulk substrates can be one choice, but it is not commercially available and have impurity absorption issue. So its necessary to grow and optimize AlN/sapphire templates with low dislocation densities and low roughness. The AlN/sapphire templates used for MQW and DBR growth in this work are from the group of Prof. Dupuis. Since the new Aixtron 3×2 inch CCS reactor was installed recently in our lab, the studies of thick AlN layer grown on sapphire was initiated. By the new system, the substrate surface can be heated up to 1300 °C. The high growth temperatures can help to increase the diffusion length of Al atoms and decrease its affinity to oxygen. In this section, the growth conditions were optimized for the one-step growth of 1 μm AlN on sapphire. The structural quality and morphology were characterized and compared.

To study the influence of growth temperature, the V/III ratio was kept constant for a series of runs, as shown in Fig. 37. The low V/III ratio of 37 was chosen in order to alleviate the parasitic reaction in the gas phase. The growth rate is around 2.2 μm/h, and the thickness of AlN layer is 1 μm. At the growth temperature of 1033 °C, visible pits can be observed on the surface which indicates that the temperature is not high enough for enhance Al migration and reduce oxygen affinity. By increasing 20 degree for the

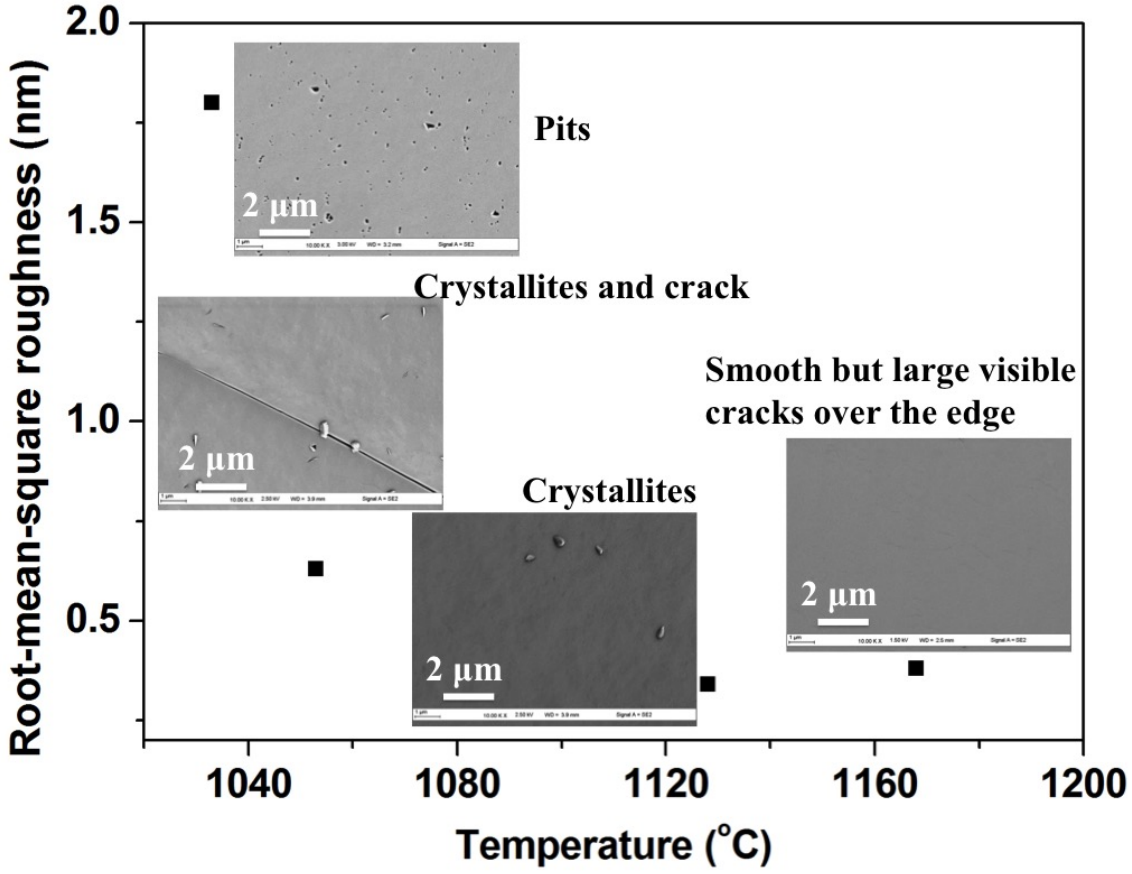

Figure 37: The surface roughness and morphology of AlN/sapphire templates grown in CCS reactor at different surface temperatures under the same V/III ratio of 37.

surface temperature, the pits disappear but there are small crystallites and a few cracks. By increasing temperature further to 1128 °C, the surface is smooth except a few crystalline particles. With higher temperature of 1288 °C, the template is smooth in the central part, but cracked in the edge area of 2-inch wafer (almost 1/4 area of the whole surface) which originates from the lattice mismatch as well as thermal mismatch between the layer and the substrate. The cracks in the edge area release the tensile strain leading to smooth surface in the central area. So here 1128 °C was chosen as the optimal temperature for the following studies.

For the same growth temperature at 1128 °C, by increasing V/III from 37 to 52, the surface roughness is almost the same (0.33 nm), but the crystallites are removed giving smooth surface. The XRD skew symmetric rocking curves of two samples were shown in Fig. 38, and the dislocation densities were calculated respectively. For V/III of 37, the densities are 3.4×10^9 cm^{-2} for the screw component and 9.0×10^{10} cm^{-2} for the edge component. For V/III of 52, the densities are 1.2×10^9 cm^{-2} for the screw component and 3.1×10^{10} cm^{-2} for the edge component. The threading dislocation density is reduced by 64% when increasing V/III by 40% .

Under this optimized condition, the 2-inch wafer of 1 μm AlN /sapphire template shows smooth surface without cracks or crystallites. The AFM image is shown in Fig. 39. The root-mean-square roughness (RMS) is 0.33 nm and growth steps can be clearly observed. There are pits positioned at the surface step, corresponding to the surface termination of pure-screw- or mixed- dislocations propagating to the surface.

The dislocation densities and surface roughness can be further improved by other techniques, such as using intermediate layers and increasing AlN thickness, as reported by X.-H. Li [139, 140]. This will be the next plan in CCS reactor to obtain high quality AlN templates for DUV devices.

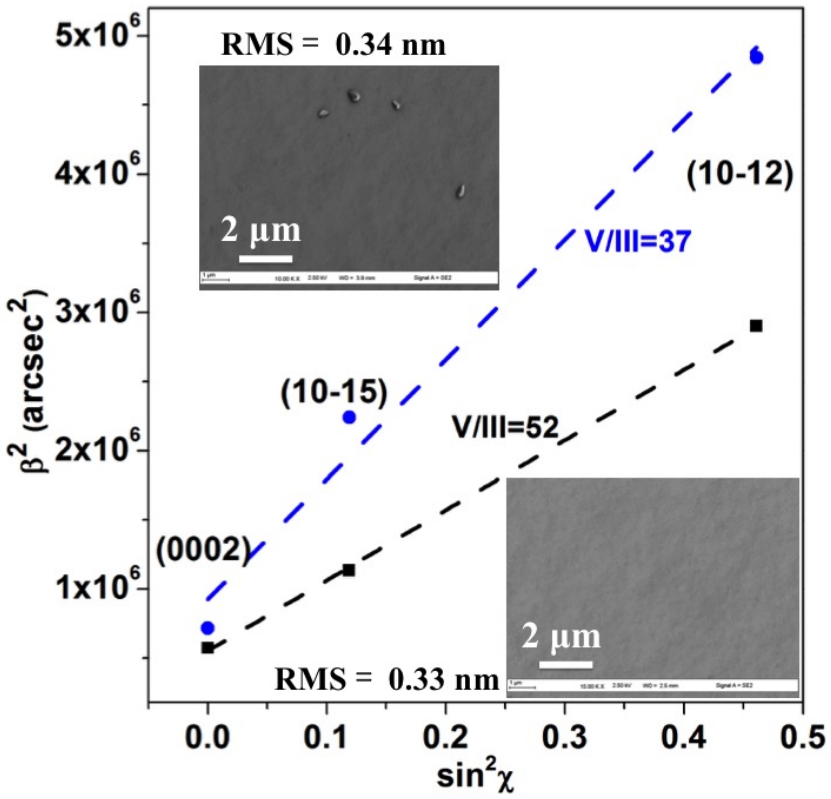

Figure 38: XRD skew symmetric scans for of AlN/sapphire template grown in CCS reactor at 1128 °C but with different V/III ratio; inset shows the morphology of the samples

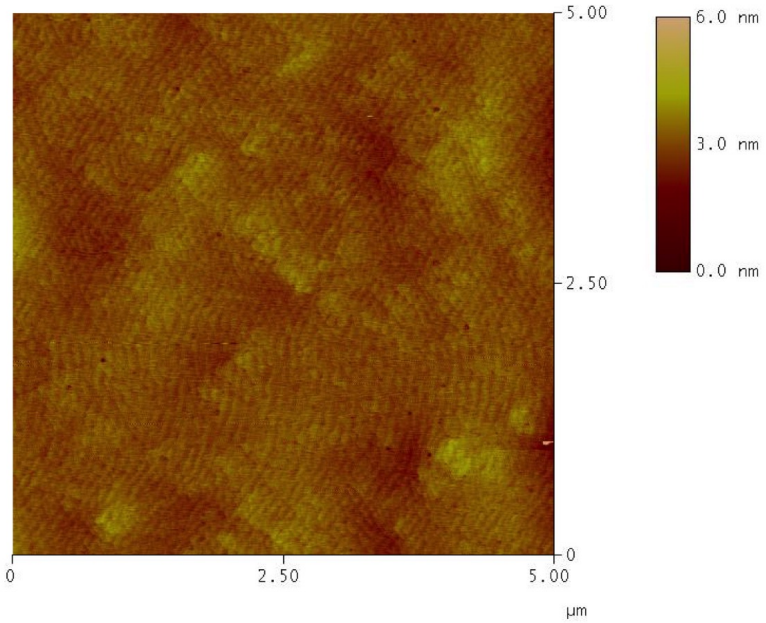

Figure 39: AFM image of AlN/sapphire template.

CHAPTER 4

DESIGN, GROWTH AND CHARACTERIZATIONS OF DEEP UV AlGaN MQWS

This chapter is addressed to the AlGaN MQWs emitting at 280 nm: design, growth and characterizations. The simulation and the design of MQWs to enhance surface emission were done by the partners in Institut Pascal - Université Blaise-Pascal (LASMEA, Aubière, France), and the basic principles are described in the first section. The structural and optical properties of 4-, 10- and 20-period MQWs are studied in the second and third sections. The experimental results confirmed the preserved oscillator strength of surface emission as designed. Besides, the analysis of typical defects in QW samples is presented in the last section. Their influences on the structural and optical properties of the MQWs are investigated.

4.1 AlGaN MQW design for enhanced TE (E⊥c) emission

4.1.1 Principles of AlGaN band structure calculation

III nitrides (AlGaN) has a direct wide bandgap over the entire composition range. The valence band (VB) splits into three bands due to crystal-field splitting and spin-orbit interaction. The schematic of band ordering is shown in Fig. 40. The energies of three bands (Γ_9, Γ_{7+} and Γ_{7-}) are related to crystal-field split-off energy Δ_{cr} and spin-orbit split-off energy Δ_{so}. The values of Δ_{cr} and Δ_{so} can be determined by measuring the interband optical-transition energies E_V^A - E_V^B and E_V^A - E_V^C [141].

Δ_{cr} of GaN is positive, so the order of VBs is E_V^A (Γ_9), E_V^B (Γ_{7+}) and E_V^C (Γ_{7-}). On the other hand, Δ_{cr} of AlN is negative, and E_V^B (Γ_{7+}) becomes the top valence band. So in AlGaN alloys, the order of the two upper valence bands is modified along with the increase of Al content, as shown in Fig. 41. Apart from the modification of the electric band structure, alloying also leads to a modification of the optical polarization properties of the interband transitions which influences the performance of the devices. In GaN, the

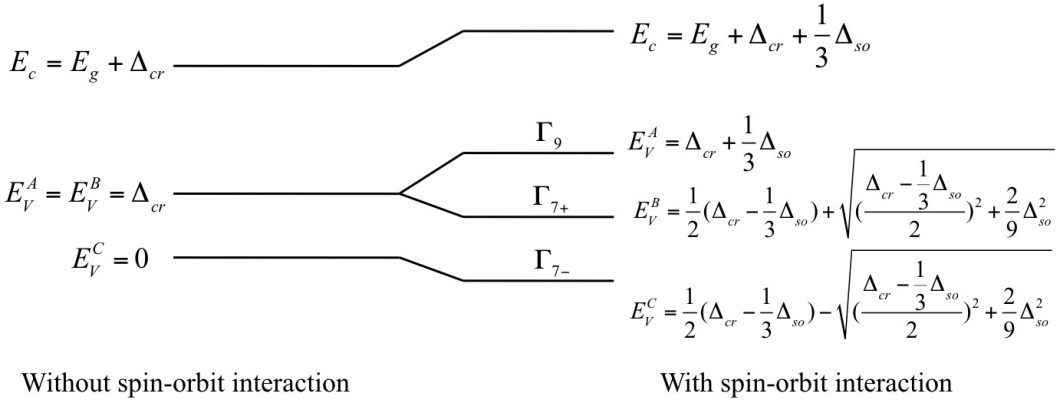

Figure 40: The band-edge energies with and without spin-orbit interaction.

upper valence band corresponds to the heavy hold band of Γ_9 symmetry, while the second one corresponds to the light hole band of symmetry Γ_{7+}. For an aluminum composition typically higher than 10%, the energy order of these two bands reverses and the band of Γ_{7+} symmetry becomes the upper valence band [88–92]. This energy crossover between AlN and GaN is also accompanied by a switching of the valence band state symmetry. The topmost Γ_{7+} valence band is governed by p_z-like state. The following bands (Γ_9 and lower Γ_{7+}) are governed by p_x and p_y-like states. So, if the three valence bands are labeled according to their zone center wavefunctions, the appropriate notation for AlN but also for AlGaN with high Al composition becomes CH (crystal field split-off band), HH (heavy hole band) and LH (light hole band) from top to bottom. The oscillator strength between the conduction band and the upper Γ_{7+} (split-off hole, CH) valence band, which becomes the fundamental transition, is highly reduced with increasing Al fraction for the configuration where the electric field is perpendicular to the c axis [88–92].

The band alignment of AlGaN is shown in Fig. 41. The band energies of AlGaN ternary alloy can be deduced from band energies of AlN and GaN with considering bowing

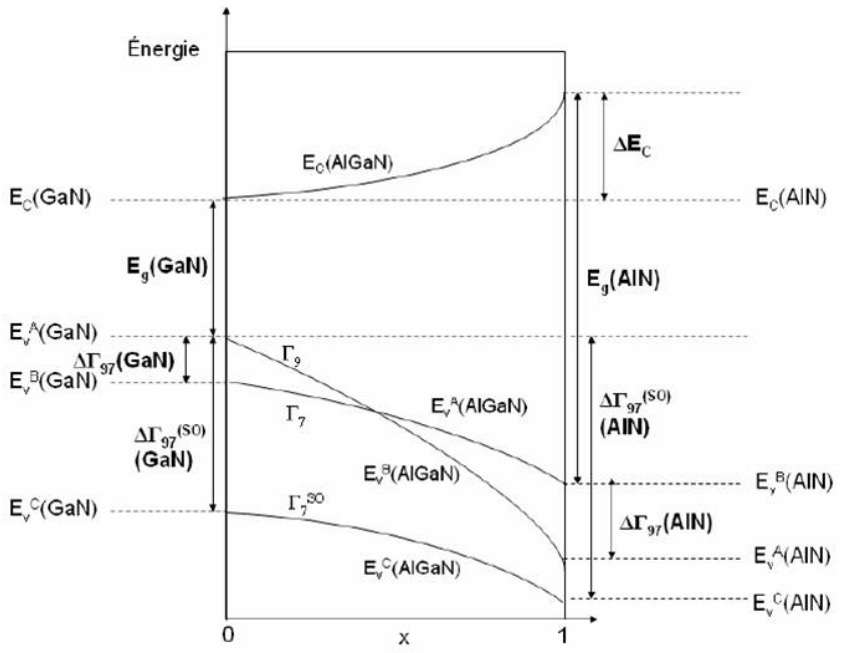

Figure 41: Band alignment of GaN/AlGaN structure [4].

parameter [4]:

$$
\begin{aligned}
E_c(AlGaN) =& E_g(GaN) + x\Delta E_c - \eta b x(1-x) \\
E_v^A(AlGaN) =& -x(\Delta E_v + \Delta\Gamma_{79}(AlN)) + (1-\eta)bx(1-x) \\
E_v^B(AlGaN) =& -x(\Delta E_v - \Delta\Gamma_{97}(GaN)) + (1-\eta)bx(1-x) - \Delta\Gamma_{97}(GaN) \\
E_v^C(AlGaN) =& -x(\Delta E_v + \Delta\Gamma_{79}(AlN) + \Delta\Gamma_{97}^{(SO)}(AlN) - \Delta\Gamma_{97}^{(SO)}(GaN)) \\
& + (1-\eta)bx(1-x) - \Delta\Gamma_{97}^{(SO)}(GaN)\ ,
\end{aligned}
\tag{33}
$$

where ΔE_v and ΔE_c are CB and VB offset. $\Delta\Gamma_{97}$(GaN), $\Delta\Gamma_{97}^{(SO)}$(GaN), $\Delta\Gamma_{97}$(AlN) and $\Delta\Gamma_{97}^{(SO)}$(AlN) are positive parameters of the band energy differences. η and $1-\eta$ are fraction of bowing b on the conduction band and valence band.

Besides the composition, the strain can also affect the valence band states and the selection rules [141–145]. Based on the work of Chuang and Chang [141], the strained effect on VB energies at Γ point can be considered by adding the terms θ_ε which represents the energy change due to uniaxial strain and λ_ε which represents the energy change due to

biaxial strain:

$$
\begin{aligned}
E_V^A(\Gamma_9) &= \Delta_{cr} + \frac{1}{3}\Delta_{so} + \theta_\varepsilon + \lambda_\varepsilon \\
E_V^B(\Gamma_{7+}) &= \frac{1}{2}(\Delta_{cr} - \frac{1}{3}\Delta_{so} + \theta_\varepsilon) + \lambda_\varepsilon + \sqrt{(\frac{\Delta_{cr} - \frac{1}{3}\Delta_{so} + \theta_\varepsilon}{2})^2 + \frac{2}{9}\Delta_{so}^2} \\
E_V^C(\Gamma_{7-}) &= \frac{1}{2}(\Delta_{cr} - \frac{1}{3}\Delta_{so} + \theta_\varepsilon) + \lambda_\varepsilon - \sqrt{(\frac{\Delta_{cr} - \frac{1}{3}\Delta_{so} + \theta_\varepsilon}{2})^2 + \frac{2}{9}\Delta_{so}^2} \ ,
\end{aligned}
\tag{34}
$$

where the uniaxial term and biaxial term can be expressed as the function of the deformation potentials D_{1-4} of the material and strain terms ε_{xx}, ε_{yy} and ε_{zz}:

$$
\begin{aligned}
\theta_\varepsilon &= D_3\varepsilon_{zz} + D_4(\varepsilon_{xx} + \varepsilon_{yy}) \\
\lambda_\varepsilon &= D_1\varepsilon_{zz} + D_2(\varepsilon_{xx} + \varepsilon_{yy}) \ .
\end{aligned}
\tag{35}
$$

The strain terms can be calculated based the lattice parameters "a" before and after deformation and elastic stress constants "C" as follows:

$$
\begin{aligned}
\varepsilon_{xx} = \varepsilon_{yy} &= \frac{a_{strained} - a_{original}}{a_{original}} \\
\varepsilon_{zz} &= -\frac{2C_{13}}{C_{33}}\varepsilon_{xx} \ .
\end{aligned}
\tag{36}
$$

4.1.2 Design of AlGaN MQWs

The amplitude of the oscillator strength for TE polarization can be restored by imposing some strain in the AlGaN QW. The strain can be due to the lattice mismatch between barriers and wells which have different Al content. Thus, the barrier composition can be chosen to provide sufficient compressive strain in the wells, and to enhance the TE-polarized optical transition.

The calculations of band structures and design of AlGaN MQWs were performed by LASMEA (Aubière, France). The band structure and the optical interband matrix elements of AlGaN compounds were carried out by using $\mathbf{k} \cdot \mathbf{p}$ formalism for strained wurtzite semiconductors taking into account both valence band mixing due to crystal field and spin orbit effects and strain effect [142], as described in the last subsection. For the design of the AlGaN/AlGaN MQW structure, envelop function simulations taking into account strain and

built-in electric fields have been performed. Considering the large scatter of valence-band offset (VBO) values reported in the literature (0.3 eV to 0.7 eV for GaN/AlN) [146–150], the experimental value of 0.5 eV determined by Baur et al. [146] for the VBO of GaN/AlN interface in the absence of strain is used. This value has already been tested on GaN/AlGaN QWs with a good agreement between calculations and experimental data [4]. The band diagram for the AlGaN/AlGaN heterostructure is then constructed by distributing the bandgap bowing on the conduction and valence bands of each alloy and by adding the strain effects induced by the lattice mismatch between two materials [4, 89, 141, 151]. The relative oscillator strength modeling is calculated by evaluating the matrix element between conduction and valence bands.

To achieve emission at a wavelength of around 280 nm, the Al composition of the well was chosen to be $x_{Al} = 0.37$ and the well thickness was fixed to 1.7 nm in the calculations. The thickness of barriers was fixed to 10 nm. The calculated values of the relative oscillator strengths for TE transition are displayed in Fig. 42 as a function of the Al composition in the barriers. The uppermost valence bands of wurtzite nitrides are formed out of p orbitals with wave functions combining $|X\rangle$, $|Y\rangle$ and $|Z\rangle$ symmetries. The anisotropic strain mixes these valence band states and the polarization properties of the interband transitions are thus modified. When the biaxial stress increases with the increase of Al content in the barriers, the band-to-band oscillator strength of the fundamental transition involving Γ_7-valence band (crystal field split-off hole band (CH)) increases up to 0.5, which corresponds to the value of the oscillator strength of the transition involving the Γ_9-valence band (heavy hole). The CH valence band is no longer purely governed by p_z states but arises from a mixing between p_x, p_y and p_z states and is therefore not forbidden for TE polarization. The compressive strain increases the weight of p_x, p_y-like states at the expense of p_z-like states. So, the optimal Al content in barriers is designed to be 0.57 ($\pm$0.01), for which the strain (-0.5%) introduced in the wells is sufficient to enhance TE-polarized optical transition and therefore surface emission. The above calculations assume no strain in the AlGaN barrier

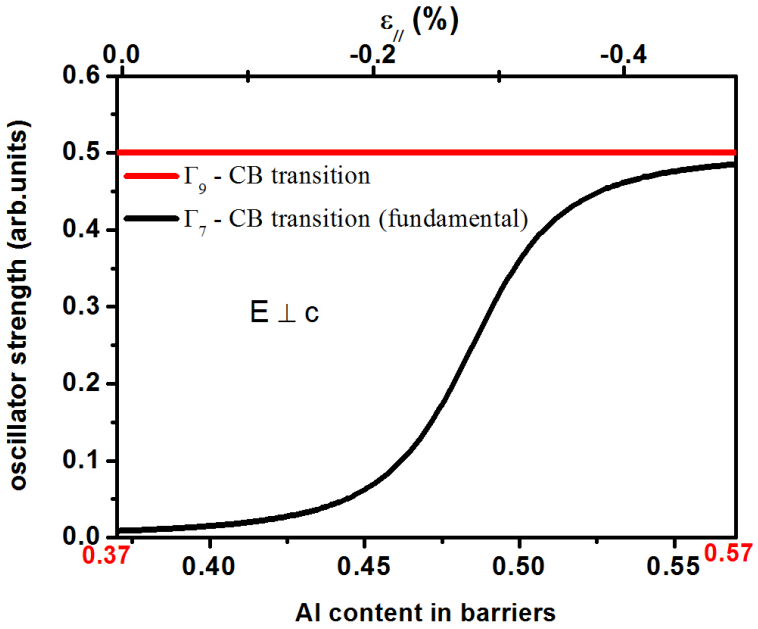

Figure 42: Relative oscillator strengths for the optical transitions between the valence bands (Γ_7 (CH) and Γ_9 (HH)) and conduction band (CB) in an AlGaN/AlGaN quantum well as a function of the Al composition in the barriers, with Al content in the well fixed to x_{Al} = 0.37. The corresponding strain in the well is also reported in the top axis. Calculations consider that the barriers are strain-free and QWs are fully-strained on AlGaN barriers.

material.

The strong electric-field in AlGaN quantum wells due to both piezoelectric and spontaneous polarization in this structure is around 1.15 MV·cm^{-1} and tends to separate the electrons and holes. To solve this problem, ultra-thin wells below 2 nm must be considered so that the oscillator strength obtained is not counteracted by the QCSE.

Practically, in order to release excess strain in the barriers, it is necessary to start the growth of the active region from a pseudo-substrate with barrier lattice mismatch as small as possible. AlN templates grown on c-Al_2O_3 wafers are appropriate substrates for the growth of Al-rich AlGaN MQW structures, however, AlN shows a lattice mismatch of 1% with $Al_{0.57}Ga_{0.43}N$ barriers. Hence, a thick, relaxed $Al_{0.57}Ga_{0.43}N$ layer has to be inserted before the MQW growth, acting as a latticed-matched buffer. Fig. 43 presents the final design of the structure.

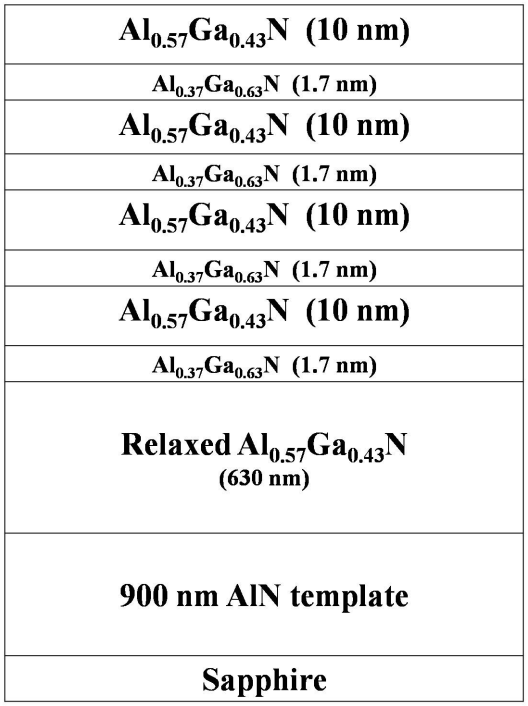

Figure 43: Schematic of MQW structure for emission at 280 nm

4.2 Growth and characterizations of MQWs

AlGaN MQW structures were realized based on the design. Detailed characterizations relating to the determination of compositions and optical properties are described in this section.

4.2.1 Structural characterizations

The quality of the relaxed AlGaN buffer is analyzed in Section 3.1.3. The MQW sample exhibits 2D morphology, and the root-mean square (RMS) surface roughness is 0.45 nm for 1×1 μm^2 scan. Figure 44 shows the corresponding 2θ-ω scan of the sample. The diffraction pattern is dominated by the strong peaks related to the AlN template and the AlGaN relaxed buffer. Satellite diffraction peaks (SL) associated with the quantum wells can also be observed indicating a good quality of MQWs. The RSM in the inset shows the AlN template spot as well as the broader AlGaN buffer spot (and barriers). The signal from the thin quantum wells is too weak to be observed in RSM. From the symmetric 2θ-ω scan and asymmetric RSM, the composition and relaxation degree of the buffer were

estimated: the average Al composition of buffer is ~0.58 (±0.01) and the buffer has 70% relaxation. The composition and thickness of the wells could not be estimated accurately by just fitting 2θ-ω scan considering that the simulation of multi-layered structure is influenced by thickness and composition for each layer simultaneously. Further characterization using STEM and EDX is necessary in order to obtain more information about the quantum wells.

HAADF-STEM cross-section images of MQWs and upper part of the relaxed buffer are shown in Fig. 45(a) and 45(b). The barrier thickness is measured to be 10 ~ 11 nm from intensity profiles and the well thickness is of 1.6 ~ 1.8 nm. It can be observed that after each well there is an Al-rich layer which is presumably caused by a switch between precursors that can be optimized for the planned future work.

The average composition of barriers could be determined from EDX quantitative analysis and was found to be 0.57 (± 0.015). The k-factors used for the EDX quantification have been calibrated using thick AlN and GaN layers layers epitaxially grown on a silicon substrate. All calibration samples were prepared by FIB (the thickness of the slices is comprised between 60 to 80 nm). The systematic control of the stoichiometry (ratio between the III elements and the nitrogen content measured) ensures to be the right conditions for quantitative analysis (with accurate k-factors). The accuracy of the EDX analysis is estimated to be 1% (except with nitrogen where the precision is rather ± 2%). The results of the quantitative analysis (composition in atomic %) does not vary by more than ± 1% when the slice thickness varies in the range from 60 nm to 80 nm.

Since the spatial resolution of the EDX analysis is typically of 2 nm, high-resolution HAADF-STEM images have been used to estimate the composition of the thin quantum wells following a procedure proposed in [110]. The electron beam scattered intensity for each point M of the background-subtracted HAADF STEM image can be expressed as:

$$I(M) = d(M) \times K \times \sum_i x_i Z_i^{\alpha} \ , \tag{37}$$

where d(M) is the STEM slice thickness at point M, K is a proportionality factor depending on the number of atoms per unit volume in the lattice, the label i corresponds to atom i, x_i

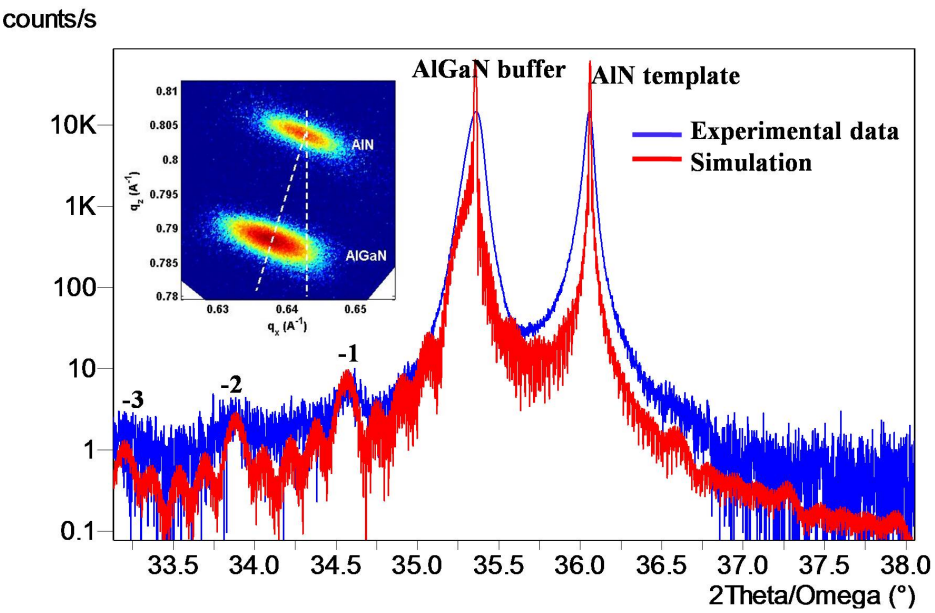

Figure 44: (0 0 0 2) 2θ-ω scan for 4 quantum wells grown on a relaxed buffer on AlN template and the simulation of the structure which used values obtained by XRD, STEM and EDX analyses. The RSM of (1 1 -2 4) reflection is shown in the inset.

is the relative proportion of atom i (at point M), Z_i is its atomic number, and the value of power α is typically close to 2.

For the $Al_xGa_{1-x}N$ layers ($x=x_{Al}$), Eq. 37 can be written as:

$$\frac{I_x(M)}{d_x(M)} = \frac{K}{2} \times {Z_{Ga}}^{\alpha}[a(\alpha) - b(\alpha) \times x] \,, \tag{38}$$

where $a(\alpha) = 1 + {Z_N}^{\alpha}/{Z_{Ga}}^{\alpha}$, and $b(\alpha) = 1 - {Z_{Al}}^{\alpha}/{Z_{Ga}}^{\alpha}$.

In order to use Eq. 38, the background-subtracted intensity $I_x(M)$ is corrected from slight variations in the STEM slice thickness variations ($d_x(M)$) by comparing the intensity of the HAADF-STEM images at points where the EDX quantitative analysis predicts a nearly constant Al composition (in the AlGaN buffer, in the barriers). The thickness variation is extrapolated from these points for the whole HAADF image. A slight, regular and nearly linear variation of the thickness is observed, except at the very top surface of the epitaxial structure where a sharper variation of the slice thickness seems to occur. This region is therefore discarded from the analysis.

Then, the value of power α and of the proportionality constant K can be retrieved from

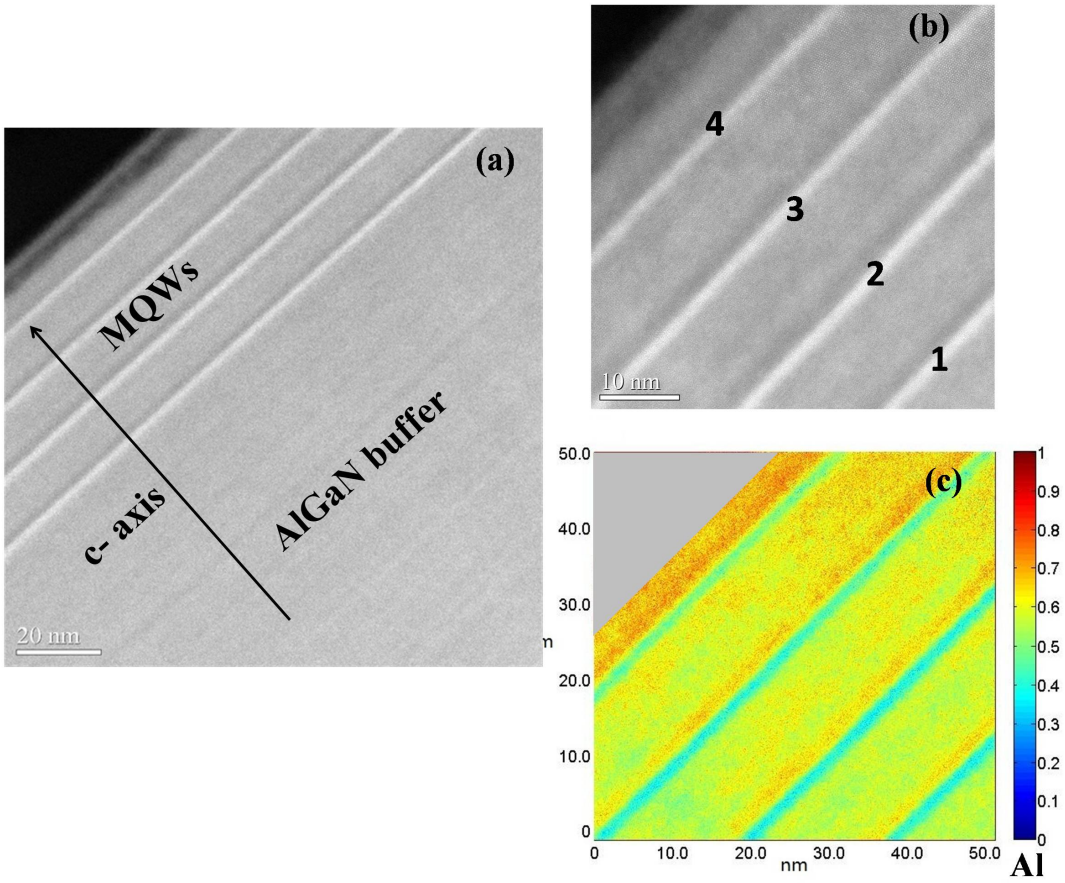

Figure 45: (a) Cross-section High-angle Annular Dark Field Scanning Transmission Electron Microscopy (HAADF-STEM) images taken along <1 1 -2 0> zone axis for MQWs and buffer layer; (b) High magnification of HAADF-STEM images; (c) Al composition map obtained from (b).

points in the AlGaN buffer layer and in the AlN template, where x_{Al} is given by the EDX quantitative analysis. It is moreover assumed that K is constant for the range of materials considered. Given the values of Z_{Ga} = 31, Z_{Al} = 13, Z_N = 7, and α lying in the range of 1.6 to 2 [110], it is found that the best consistency with the experimental values in AlGaN buffer and AlN template are obtained for α = 2 in our case.

The complete analysis results in a chemical mapping, as shown in Fig. 45(c). The average Al content in the barriers is in accord with EDX value ($x_{Al} \sim 0.57$) and the average Al content in the wells is estimated to be $x_{Al} \sim 0.38$ (± 0.015). The thickness and composition values obtained from Figs. 45(a)-45(c) fit well the XRD experimental data shown in Fig.

44.

It is noticed that the composition of 4^{th} well in the mapping is abnormally high (x_{Al} = ~0.50), and so as the last barrier (x_{Al} = ~ 0.67) which is not consistent with EDX value. It might be caused by the fact that the thickness variation near the top surface deviates from the linear extrapolation and hence leads to the inaccuracy of composition estimation from Z-contrast intensity.

4.2.2 Optical characterizations

Cathodoluminescence (CL) spectra at 77 K under different excitation energy are shown in Fig. 46(a). Under a low excitation power of 3 keV corresponding to a penetration depth of the electron beam of typically 30 nm, a single emission peak from wells at 286 nm indicates that the carriers are mostly confined in the wells. When the excitation power is increased to 10 keV and the penetration depth of the excitation beam reaches 230 nm, a luminescence signal at 262 nm appears in addition to the emission of the wells, which is attributed to the barriers and buffer layer. The emission at 262 nm corresponds to a bandgap energy of 4.73 eV, which is in agreement with the experimental composition of the barriers and buffer layer (x_{Al} ~ 0.57). At room temperature the increase of the barrier luminescence with respect to 77K is attributed to the thermal activation of carriers in the AlGaN layers (barriers or buffer layers). In the case of an optical in-well pumping (excitation at 266 nm) as displayed in Fig. 46(b), the laser beam is mainly absorbed in the QWs and not in the barriers. Thus, only the luminescence of the wells is observed. However, it is found that both classical photoluminescence and cathodoluminescence provide the same QW emission line. The linewidth is 9.5 nm for PL at 77 K and 11.9 nm for PL at 300 K.

Figure 46(c) shows the transmission measurements (E-field $\perp$ c configuration) at 77 K together with numerical simulations based on transfer matrix formalism. The experimental spectrum reveals the absorption edge of the barriers at 260 nm, while a 10% drop of transmission is observed at 281 nm due to absorption in the wells. It is worth noting that calculations fit the experimental results in a satisfying way. The absorption coefficients

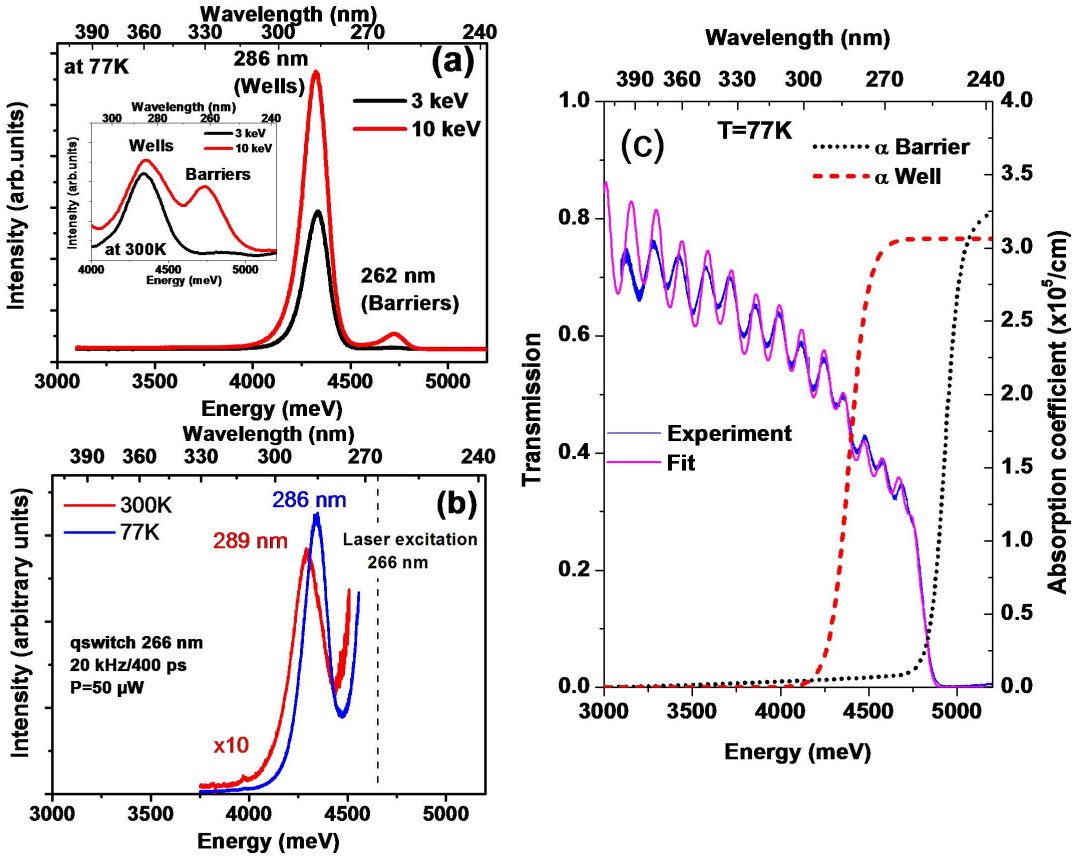

Figure 46: (a) Cathodoluminescence (CL) spectra at 77 K (and at 300 K in the inset) for two different values of excitation power; (b) Photoluminescence (PL) at 77 K and at 300 K under excitation of 266 nm; (c) transmission measurements and transfer-matrix simulation of MQWs together with absorption coefficients (α_{well}, $\alpha_{barrier,\,buffer}$ used in the simulation).

used in the simulation are also displayed in Fig. 46(c) for both barriers and wells. A weak absorption with linear energy dependence has been added in the barriers and the buffer in order to reproduce the overall decrease of the transmission signal. The latter might be caused by defects originated from the AlN template. The absorption coefficient in the wells is found to be as high as 3×10^5 cm^{-1}, which implies that the oscillator strength is preserved in the QWs despite the high aluminium composition.

It is noted that the splitting between Γ_{7CH}-CB (fundamental) and Γ_9-CB transitions is evaluated to be equal to 32 meV. By considering the AlGaN emission broadening which is due to intrinsic alloy disorder and extrinsic inhomogeneities such as QW thickness fluctuations, it appears that the Γ_{7CH}-CB and Γ_9-CB transitions lie in the same energy range. The energy difference between these two transitions depends on several parameters (band offset, deformation potentials, effective masses...). So the absorption signal accounts for both transitions. However, it has been established through calculations that the strain preserves the oscillator strength of the fundamental transition (Γ_{7CH}-CB). Therefore it can be concluded that our MQW design with the use of relaxed buffer is promising for the fabrication of surface-emitting LED or lasers in DUV region.

The results of this section can be found in [152].

4.3 10- and 20-period MQWs

The results shown in the last section is an example for 4-period MQWs. In this section, 10- and 20-period MQWs would be analyzed and compared in the aspect of structural quality and emission properties. These samples would be used for the processing of devices by depositing high-reflective dielectric DBR on the top and the bottom after thinning down sapphire.

The XRD symmetric 2θ-ω scans and unsymmetric RSMs can be seen in Fig. 47. Satellite peaks associated with MQWs interfaces can be clearly observed for both. The MQWs are pseudomorphically strained on the AlGaN relaxed buffer based on (1 1 -2 4) RSMs.

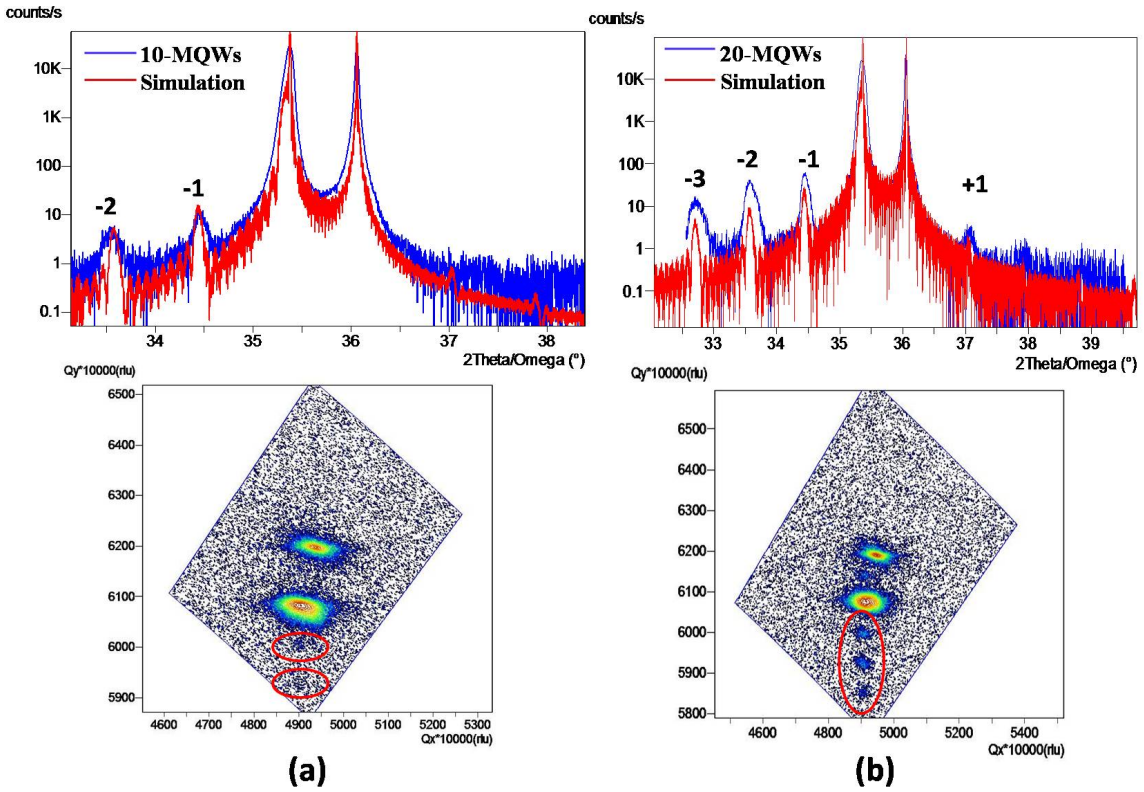

Figure 47: Symmetric 2θ-ω scans and (1 1 -2 4) RSMs of (a) 10-period and (b) 20-period MQWs grown on a relaxed AlGaN buffer on AlN templates.

According to the simulation, the buffer containing 0.58 (± 0.01) Al has 70% relaxation, the wells of both samples contain 0.38 (± 0.015) Al with thickness of 1.3 nm (± 0.2 nm), and the barriers contain 0.58 (± 0.015) Al with thickness of 9.3 nm (± 0.2 nm). Figure 48 shows that the 20-period MQWs exhibit obvious growth terraces beyond the V-pits. The influences of V-pits would be discussed in the section 4.4. Cross-sectional HAADF-STEM image of 10-period MQWs and corresponding chemical mapping were demonstrated in Fig. 49. Based on the chemical mapping, the ultra-thin wells contain 0.37 (± 0.016) Al and thickness was around 1.5~1.7 nm, which confirmed the XRD simulations.

The optical properties were investigated by CL at room temperature with different excitation energy. The wavelength of 20-period MQWs is 17 nm red-shifted, which can be due to the thickness variation of ultra-thin wells between samples. Based on our studies on different MQW samples, a small change of well thickness (e.g. from 1.1 nm to 1.5

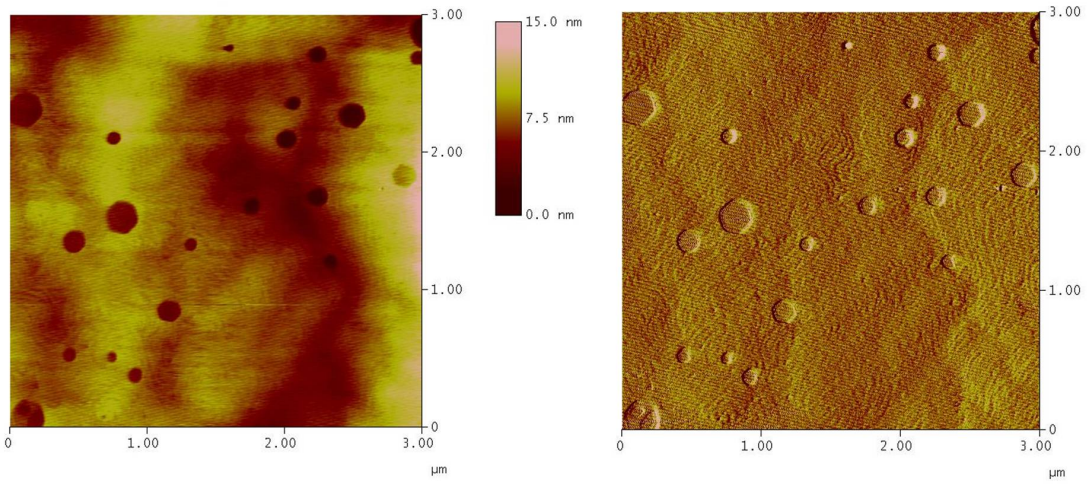

Figure 48: AFM images of 20-period MQWs grown on a relaxed AlGaN buffer on AlN templates.

nm) can cause an obvious shift of the emission wavelength. However, the determination of well thickness can not be accurate enough to identify this small variation. Along the increase of excitation energy, the wavelengths stay almost constant. The intensity increases first and then decreases along with the increase of penetration depth. 10-period MQWs achieve maximum emission intensity under 4 keV with penetration depth of around 40 nm and 20-period MQWs achieve maximum under 6 keV with penetration depth of around 70 nm. The FWHM demonstrates an inverse "S" shape, which might be related to the carrier dynamics and also penetration depth in the MQWs.

SEM image and corresponding hyperspectral CL mapping of 20-period MQWs are shown in Fig. 51. It scans over the large area (228 × 171 μm^2), and the variation of emission wavelength is only 0.9%, the variation of FWHM is 10%, and the variation of intensity is 8%, which indicate the good uniformity of the MQW growth.

4.4 Defects in MQWs and their influence on DUV emission

Compared with InGaN-based visible laser diodes or light emitting diodes (LEDs), the efficiency of DUV light sources based on AlGaN material system is much lower. One of

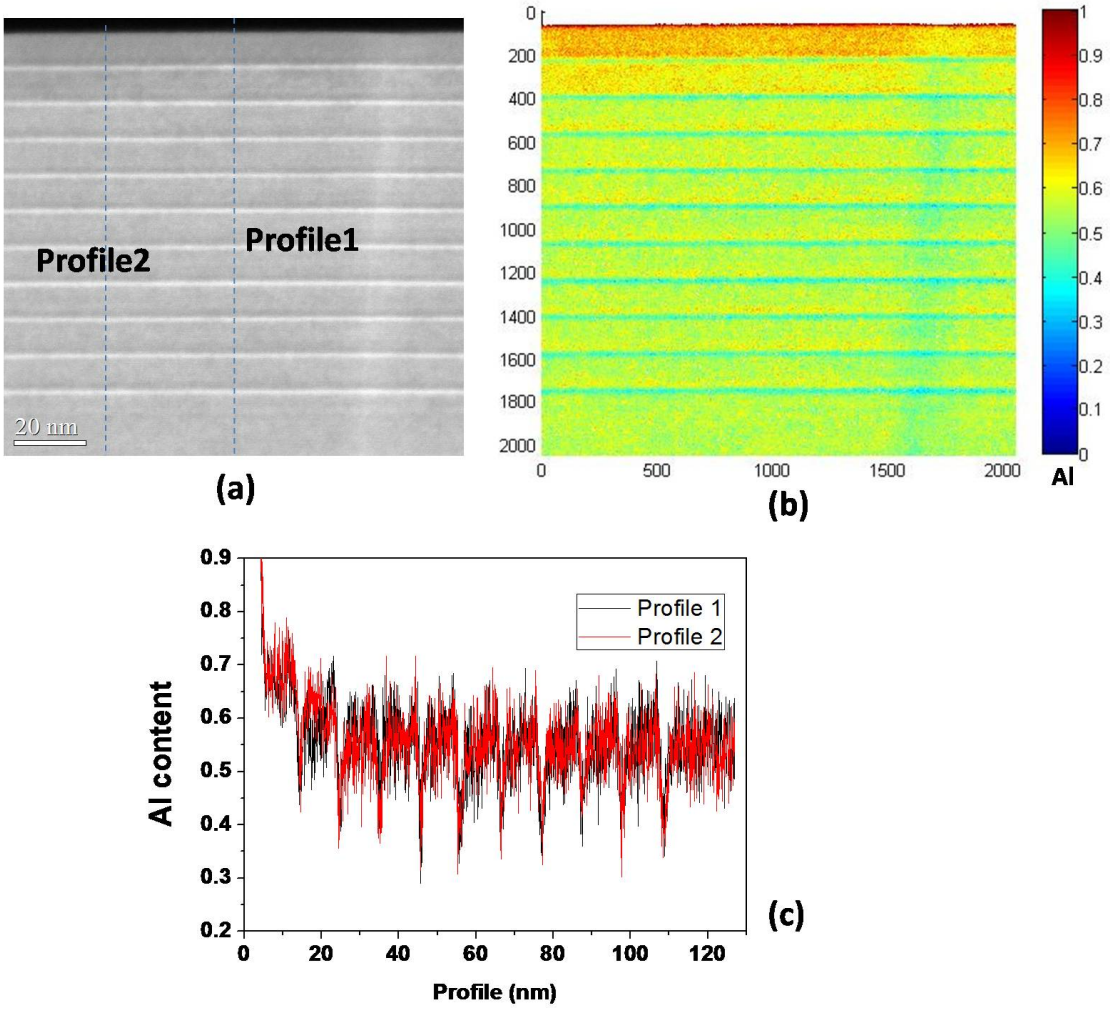

Figure 49: (a) Cross-sectional HAADF-STEM image of 10-period MQWs grown on a relaxed AlGaN buffer; (b) Compositional mapping obtained from the STEM image; (c) Al content distribution along the profiles marked in (a).

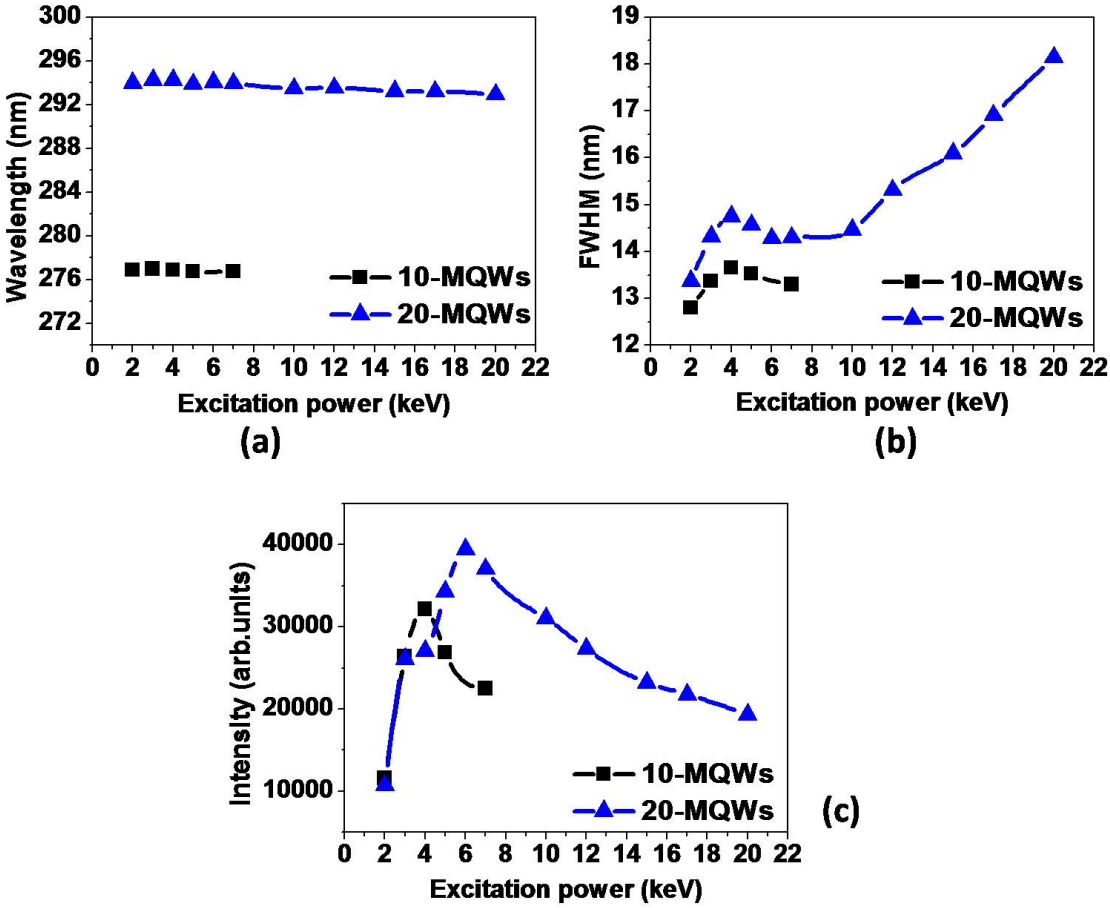

Figure 50: Comparison of (a) CL emission wavelength, (b) FWHM and (c) emission intensity at room temperature between 10- and 20-period MQWs grown on a relaxed AlGaN buffer on AlN templates.

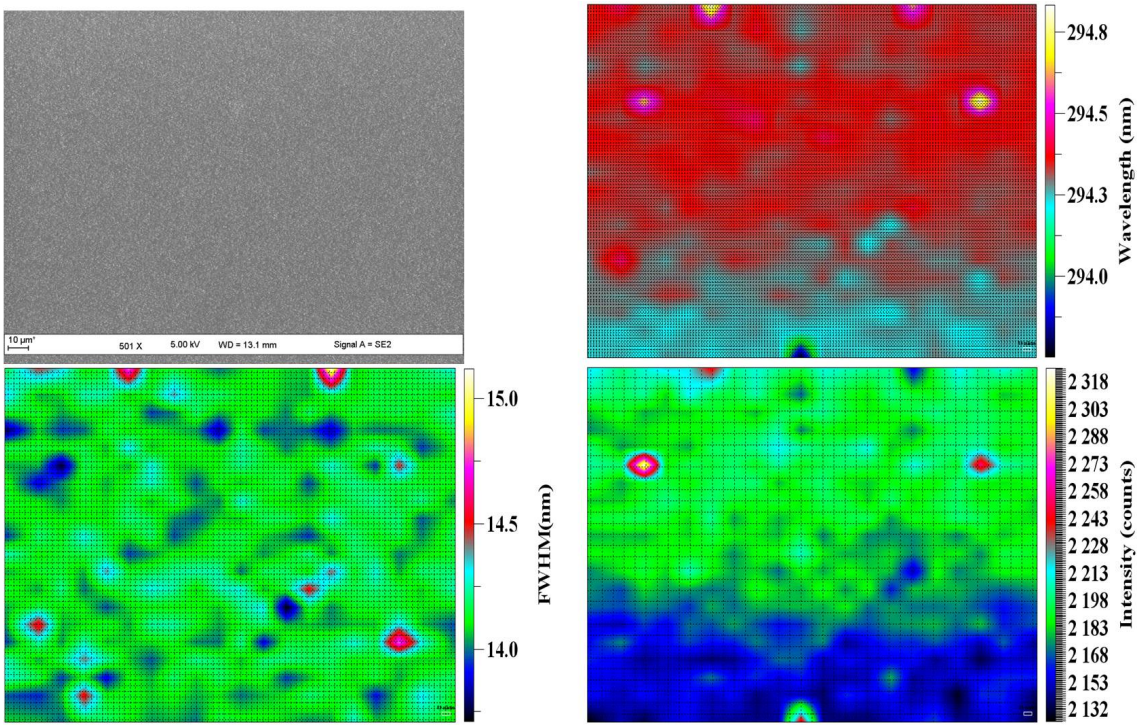

Figure 51: CL hyperspectral mapping of 20-period MQWs at room temperature.

the biggest issues is the rapid degradation of structural quality for Al(Ga)N epitaxial layers with increased Al content. Bulk AlN substrates could be good candidates to achieve low-threshold optically pumped DUV lasers due to small lattice mismatch with epitaxial layers and low dislocation density below 5×10^{8} cm^{-2} [21, 43, 44], but they suffer from high impurity absorption, high cost and limited availability. LED and laser devices were also obtained on AlN templates grown on sapphire [46, 47], but threading dislocation density is still above 10^{9} cm^{-2}, limiting performance. Besides threading dislocations (TDs), the impurity (such as oxygen) effect is greater in AlN epitaxial layers than in GaN due to low diffusion length of Al atoms (high sticking coefficient) and increased affinity of Al to oxidize, which cause rather high density of defects in AlGaN layers with Al content larger than 50% [22, 23]. Unlike the defects in InGaN/GaN MQWs which have been widely studied (even though the influence of defects on emission efficiency is still controversial) [153–158], only a few reports have focused on the study of the typical defects in metal organic vapor phase epitaxy (MOVPE) grown AlGaN MQWs on AlN templates for DUV

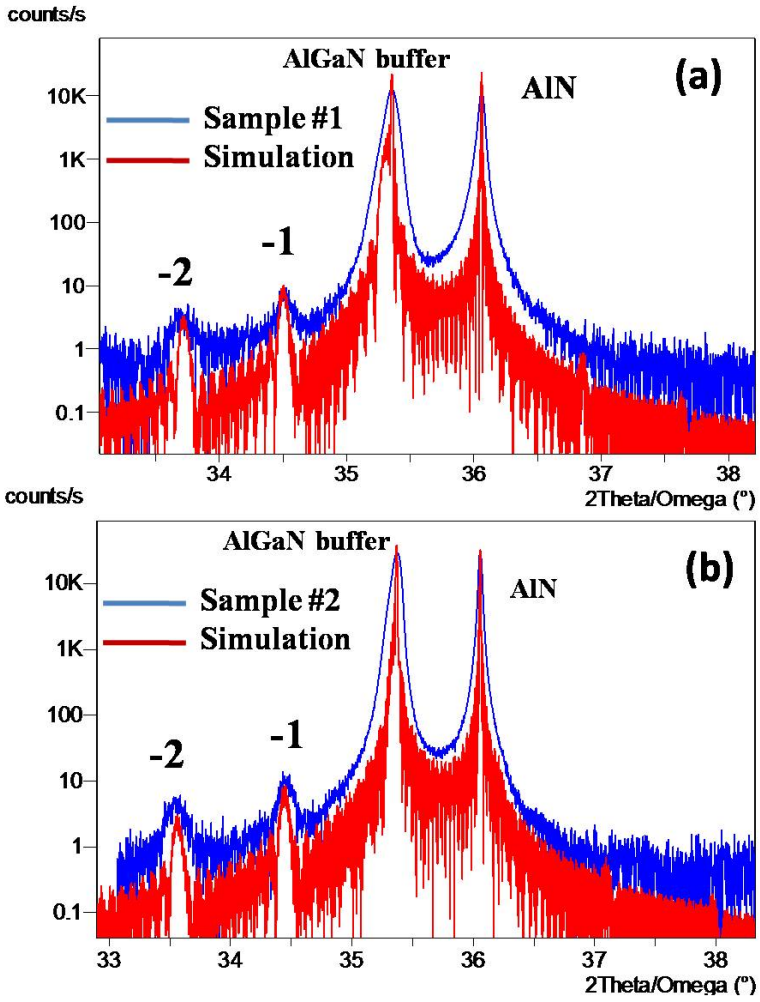

Figure 52: 2θ-ω scans of (a) sample #1 and (b) sample #2.

devices and especially their influence on the optical emission [159–162].

In this section, the threading dislocations and V-shape pits in AlGaN MQW structure grown on AlGaN buffer on AlN templates were characterized by different methods that allow a discussion of the potential origin of dislocations and V-pits [163]. MQWs samples with different defect densities were prepared in order to study the optical influence of the defects on DUV emission at 280 nm.

4.4.1 Structural investigations of defects

AlN templates grown on c-axis sapphire with different threading dislocation densities were used as substrates for the same structure, one with high dislocation density (template #1)

and the other with low dislocation density (template #2). The samples grown on the same type of template in different runs have comparable defect density, which confirmed reproducibility. The samples grown on different types of templates have significant difference in V-pit density and they were labeled as sample #1 (on template #1) and sample #2 (on template #2) for this study. Figure 52 shows (0 0 0 2) 2θ-ω scans of both samples. Satellite diffraction peaks (SL) associated with the quantum wells can be observed which indicates abrupt interfaces between wells and barriers. Based on (1 1 -2 4) reciprocal space mapping, the buffer containing 0.58 (± 0.01) Al has 70% relaxation. According to the simulation, the wells of sample #1 contain 0.38 (± 0.015) Al with thickness of 1.5 nm (± 0.2 nm), while the barriers contain 0.58 (± 0.015) Al with thickness of 10.3 nm (± 0.2 nm). For the sample #2, the wells contain 0.38 (± 0.015) Al with thickness of 1.3 nm (± 0.2 nm), while the barriers contain 0.58 (± 0.015) Al with thickness of 9.3 nm (± 0.2 nm).

The FWHM angles measured for AlN templates and thick AlGaN layers (buffer + MQWs) of two samples are shown in Fig. 53. The screw and edge TD densities calculated by the method above are summarized in table 1. For both samples, extra TDs were not generated within the relaxed AlGaN buffer layers. The AlN template used for sample #1 exhibits 3 times higher screw and edge TD densities than sample #2, and the density of pits on the surface is around 30 times higher as seen in SEM images. These holes have hexagonal shape, and the ultra-high density of the holes in sample #1 leads to the surface inhomogeneities. On the contrary, sample #2 with much lower pit density has a flat surface (apart from holes) with root-mean square roughness (RMS) as small as 0.5 nm by AFM measurements. The slight difference of thickness may be due to unintentional drift between the runs.

In order to study the origin of these holes and their influence on the MQWs growth, the cross-section HAADF-STEM was performed and images of sample #1 are shown in Fig. 54. In the flat area of Fig. 54(a), the 10-period MQWs have good uniformity and periodicity. The thickness of barriers and wells agrees with XRD simulation results. In Fig. 54(b),

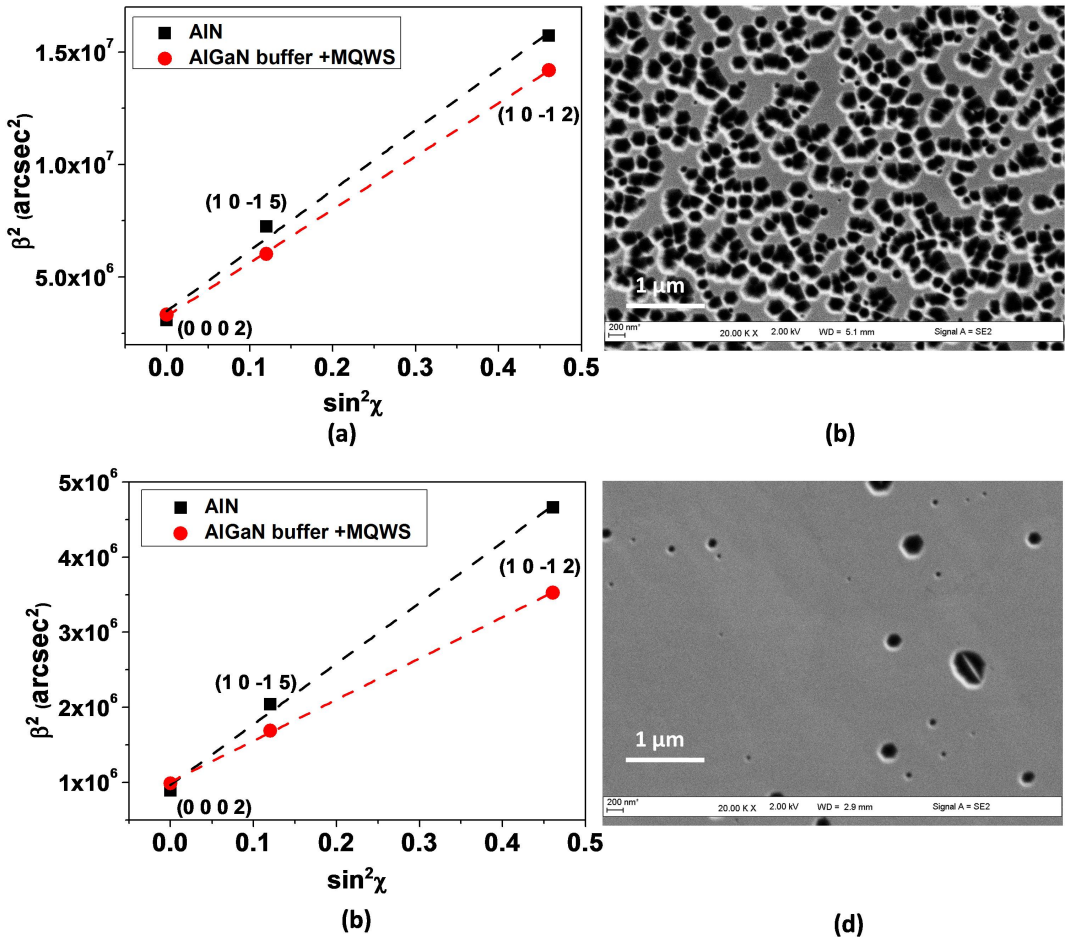

Figure 53: (a) Skew symmetric ω scans and (b) SEM images of sample #1; (c) skew symmetric ω scans and (d) SEM images of sample #2.

Table 8: Estimated defect densities (FWHM determination and linear fitting lead to an estimated error of 15% for threading dislocations) for sample #1 and sample #2.

		Screw TDs (cm^{-2})	Edge TDs (cm^{-2})	V-pits (cm^{-2})
Sample #1	AlN template	$\sim 7.3 \times 10^9$	$\sim 1.7 \times 10^{11}$	$\sim 2 \times 10^9$
	AlGaN buffer	$\sim 6.7 \times 10^9$	$\sim 1.5 \times 10^{11}$	
Sample #2	AlN template	$\sim 2.0 \times 10^9$	$\sim 4.9 \times 10^{10}$	$\sim 7 \times 10^7$
	AlGaN buffer	$\sim 2.1 \times 10^9$	$\sim 3.5 \times 10^{10}$	

it is clearly observed that the threading dislocations originate from the nucleation layer at the interface of AlN and sapphire. After certain thickness, the dislocations are mostly aligned along the [0 0 0 1] axis. These dislocations can form low angle grain boundaries and lead to a twist of the lattice. The V-pits near the surface are always associated to these grain boundaries. Figure 54(c) is the plan-view HRTEM images of the AlN template in which some grains with size from 50 to several hundred nanometers can be identified. The atomic resolution STEM image with higher magnification is shown in Fig. 54(d) to get rid of the Moiré fringes. These grains are separated by low-angle boundaries with small misorientation of 1 $\sim$ 2 degrees. During regrowth of AlGaN layers and MQWs, the threading dislocations and grain boundaries propagate into the following layers and penetrate the whole structure.

By looking into the V-shape pits in Fig. 54(e) with higher magnification, the apex of the holes is connected to extended defects which are c-axis oriented and inherited from the AlN layer. These lines should be edge threading dislocations or mixed threading dislocations since the image is taken along the <1 1 -2 0> zone axis. The possible cause of V-pits could be that impurities tend to segregate into dislocations, which may locally impede growth resulting in a small indentation. Once the facets of slow growth planes are formed due to these indentations, a V-pit can be generated [164, 165]. Compared with the sample #2, the sample #1 has higher edge threading dislocation density which increases the probability for forming pits.

As shown in Fig. 54(e) and 54(f), the facets of the holes are inclined about 62° to the c plane, which corresponds to {1 0 -1 1} facets. The growth rate on these planes is much slower than on the c plane [164, 165], so a V-shape hollow hole is formed. Figure 54(f) is an example of 4-period MQWs for investigating the sidewall growth in a V-pit. On the V-pit sidewall which is near c-plane surface, the weak contrast of QWs can be observed. Both the thickness of wells and barriers here are almost one third of the ones grown on the c plane. This small area of QW growth on the sidewall may lead to some additional emission

wavelengths with weak intensity giving rise to main peak broadening. In the area closer to the center of the hole, the wells are merged into the barriers and cannot be identified. The V-pits interrupt the superlattice growth and may lead to non-uniformity of 2D MQW properties.

4.4.2 Optical influence of defects in AlGaN MQWs

The optical properties of the MQWs samples were investigated. The PL measurements were done from 5 K to 275 K with a cw laser (266 nm) and a weak excitation power of 1W/cm^2 in order to maintain the thermal equilibrium condition and to avoid saturation of emission intensity. The spot diameter of PL is around 100 μm. For transmission measurements, the size of probed area is around 0.02 mm^2. Figure 55(a) shows the PL at 80 K and transmission spectrum at 77 K. Sample #1 shows a well-defined emission at 282 nm. The absorption edge of the wells is at 281 nm and absorption edge of barriers is at 260 nm, which is in a good agreement with the design and with the compositions determined by XRD. For the sample #2, the PL emission is at 278 nm while absorption edge is 275 nm for the wells and 260 nm for the barriers. The absorption edge of sample #2 is 6 nm blue-shifted which can be due to the thinner wells according to XRD simulation. The emission of sample #1 has full width at half maximum (FWHM) of 12.5 nm, while sample #2 has FWHM of 7.2 nm indicating a lower inhomogeneous broadening, which is consistent with transmission measurements. The broadening of emission peak in sample #1 can be caused by the local variations of thickness or composition in MQWs which occurred in the high density of V-pit sidewalls near the c-plane surface, as shown in Fig. 54(f).

Figure 56 shows the PL integrated intensity as function of the inverse of temperature as well as Arrhenius fitting curves. The fitting equation is as follows [166]:

$$I_{PL}(T) = \frac{I_0}{1 + Aexp(-\frac{E_A}{kT}) + Bexp(-\frac{E_B}{kT})}, \tag{39}$$

where I is the integrated intensity with arbitrary unit, and I_0 is a fitting parameter which can be seen as the integrated intensity when T is close to 0 K. A and B are fitting constants for

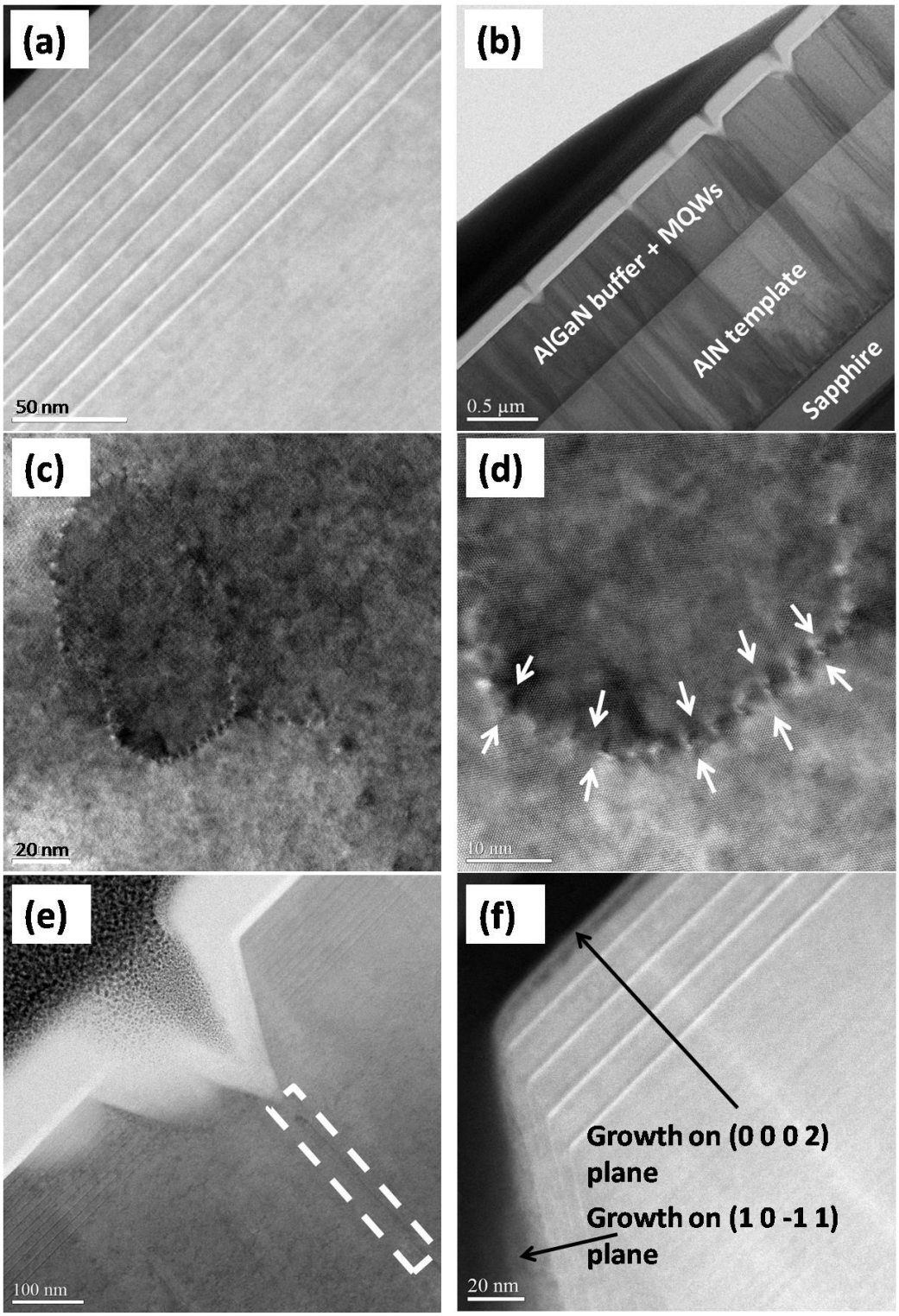

Figure 54: (a) Cross-section HAADF-STEM image of sample #1 showing 10-period MQWs without dislocations; (b) low-magnification bright field (BF) STEM image showing origin of defects; (c) plan-view HRTEM image of AlN template on sapphire showing grains; (d) high magnification image of grain boundaries; (e) high-magnification BF image on V-shape pits; (f) high-magnification HAADF-STEM image of 4-period MQWs showing sidewall of V-pits.

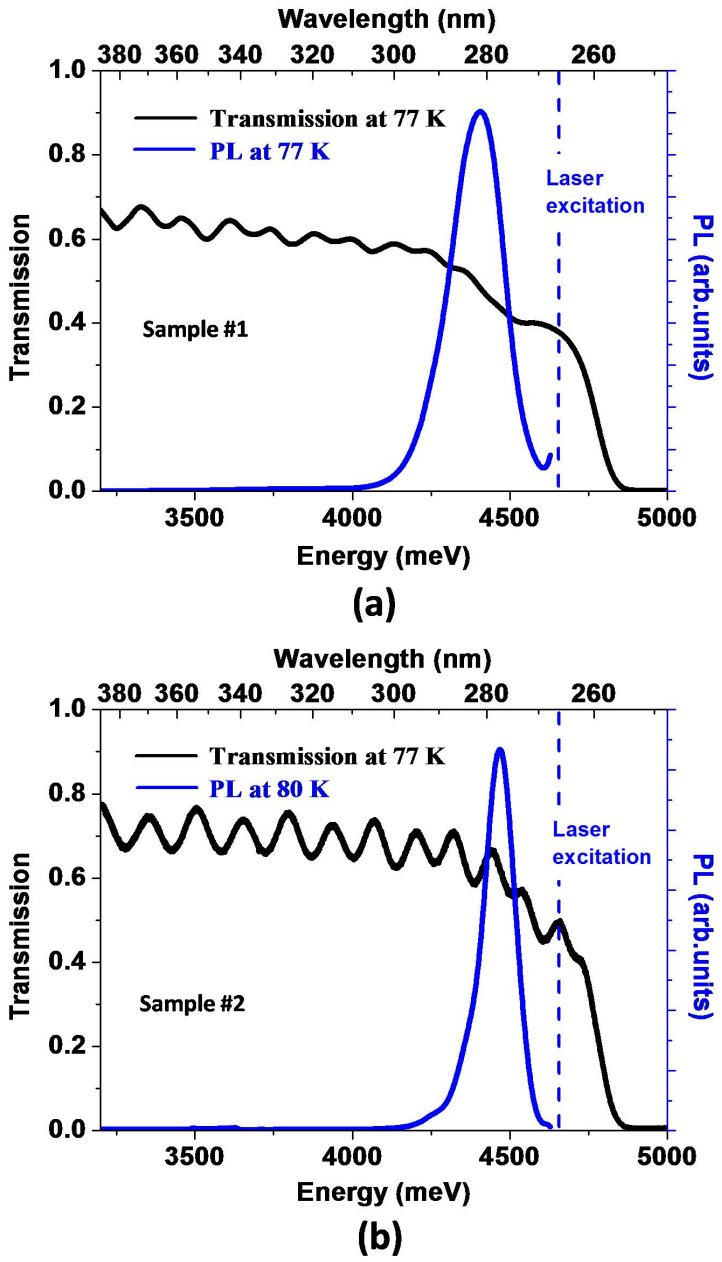

Figure 55: Transmission spectra at 77 K and macro-PL at 80 K for (a) sample #1 and (b) sample #2.

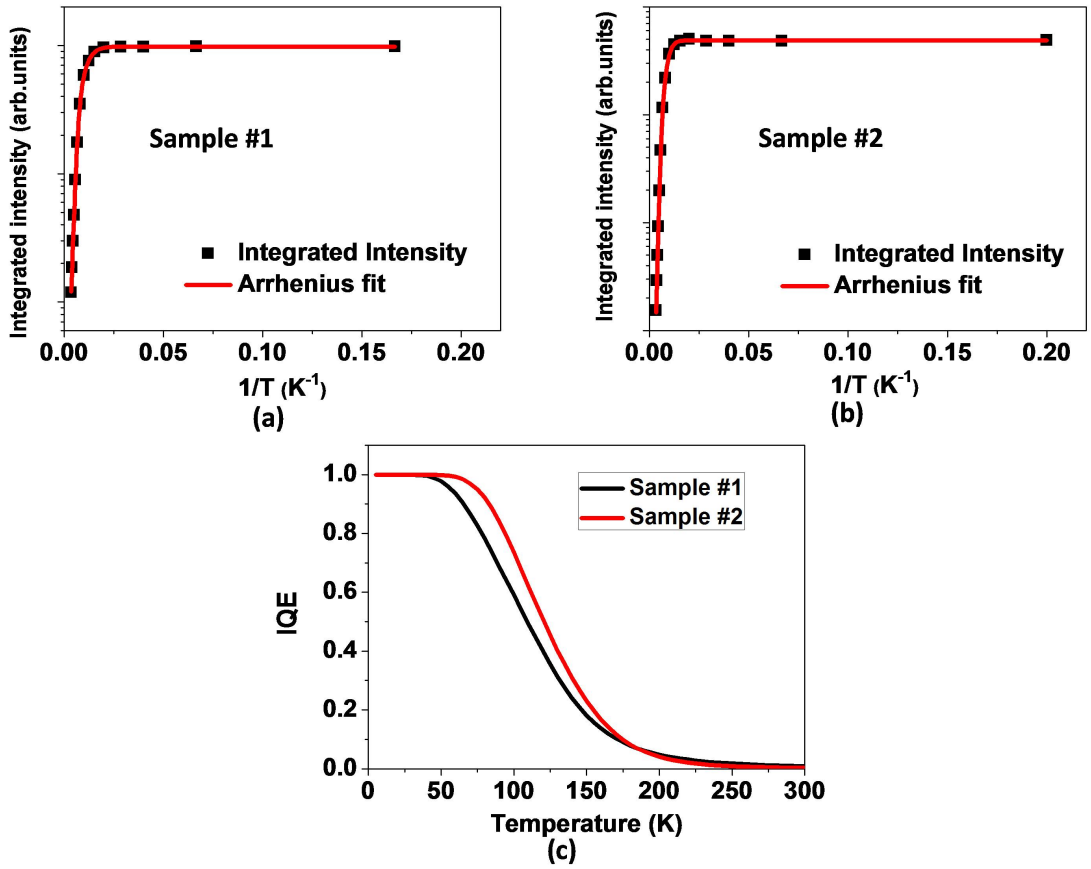

Figure 56: PL integrated intensity as function of temperature (with a cw laser and a weak excitation of ~ 1W/cm^2) and Arrhenius fitting for (a) sample #1 and (b) sample #2; (c) is the curve of IQE versus temperature based on Arrhenius equation fitting.

two nonradiative recombination channels: the first mechanism (channel A) is for detrapping of localized excitons which dominates at low temperature range, and the second (channel B) is for escaping out of the wells which dominates at high temperature range. E_A and E_B are corresponding activation energies required for two paths of carriers escape from localized states into the non-radiative recombination centers. The internal quantum efficiency (IQE) can be compared by defining IQE=I(T)/I_0 [167, 168]. In this case, the efficiency is assumed to be 100% at 5 K, which is reasonable since the intensity was almost constant (to be I_0) in the temperature range of 5 to 50 K indicating almost no influence of nonradiative process in this range.

Based on Arrhenius equation fitting, sample #1 has 29 meV for E_A and 96 meV for

E_B. Sample #2 has 49 meV for E_A and 150 meV for E_B. There is a larger energy barrier of nonradiative processes for sample #2. Figure 56(c) shows the IQE variation along with the temperature for two samples based on Arrhenius equation. At 77 K, the IQE of sample #1 decreased to 80% while sample #2 still has IQE of 94%. This can be explained by the increased concentration of nonradiative centers caused by higher dislocation density in sample #1 [169, 170]. In the high temperature range, the IQE of both samples drops dramatically due to the high level of dislocation densities. Near room temperature, the error bar becomes large because emission intensity is weak and the residual laser contribution to the luminescence is not negligible. Both samples have IQE of 0.5 $\sim$ 1% near room temperature, which is in agreement with simulated value for this level of dislocation densities [171]. To increase the IQE at room temperature, the quality of AlN templates should be further improved [118, 119] to reduce threading dislocation densities. The 30 times higher density of V-defects in sample #1 doesn't seem to affect the PL behaviour. It could be explained by the fact that the QWs are almost absent in the V-pits according to Fig. 54(f), in other words, the contribution of this part to the intensity (I) of main emission peak is negligible. But it should be noted that these pits may lead to current leakage as what has been observed in InGaN MQWs [155] and to lower external emission efficiency of current-injected LEDs or lasers [160].

The CL spectra shown in Fig. 57 were collected by scanning over an area $\sim$ 8 μm $\times$ 11 μm at room temperature, giving the average information of the sample (including flat areas and rough areas with pits). The measurements were done under excitation from 3 keV to 7 keV. Figures 57(a) and 57(b) show the spectra under 7 keV which corresponds to a penetration depth of the electron beam of typically 90 nm. Emission from wells is located at 286 nm with FWHM of 16 nm for sample #1 and at 276 nm with FWHM of 13 nm for sample #2. Besides the emission from MQWs, both samples show weak defect band emission at 333 nm. By comparing the emission intensity from the wells and the defect band, the ratio of $I_{MQWs}/I_{defects}$ is 4.5 for sample #1 and 24 for sample #2 which

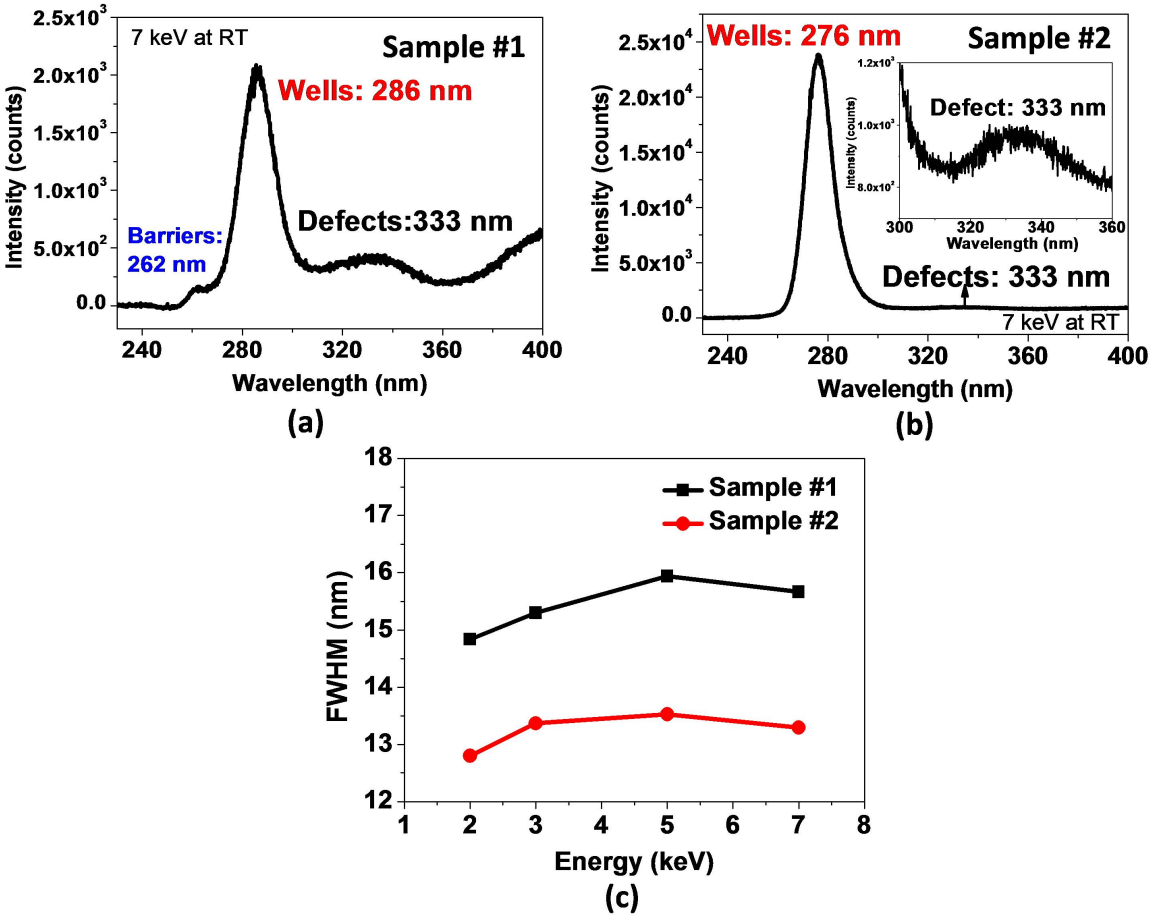

Figure 57: CL spectra under 7 keV at room temperature for (a) sample #1 and (b) sample #2; (c) is FWHM of QW emission peaks under different electron beam energies at room temperature.

may be attributed to lower dislocation density and the existence of more flat surface area with good quality QWs which can interact with the electron beam. The comparison of FWHM between the two samples in Fig. 57 confirms again the higher emission uniformity of sample #2 with the fewer V-pits.

CHAPTER 5

DISTRIBUTED BRAGG REFLECTOR: SIMULATIONS AND REALIZATION

Chapter 5 focuses on the theoretical simulation and the experimental realization of DUV DBRs that apply BAlN/Al(Ga)N heterostructures. The simulation of the ideal DBR structures is based on the transfer-matrix method presented in the first section. The reflector software was developed by Dr. Abid in his thesis in 2013 [9]. The design of DBRs is discussed in the second section.

In the third section, different factors leading to the degradation of DBR performance including surface roughness, interface roughness and strain are introduced into the reflector software, and their influences on the DBR reflection are investigated theoretically. Then the experimental results of BAlN/Al(Ga)N DBRs obtained are presented in the last section. The influences of the structures and growth conditions are studied. Based on the detailed characterizations, the simulations with the input of quality parameters are performed and then compared with the experimental spectra .

5.1 Transfer-matrix simulations of DBRs

This section describes the principles and methods for simulating the specular reflection on the surface of distributed Bragg mirrors.

The tangential components of the electric and magnetic fields are continuous across the interface, so it should satisfy the boundary conditions as follows:

$$\begin{cases} E_{i1} + E_{r1} = E_{t1} + E'_{i1} \\ B_{i1}/\mu_1 - B_{r1}/\mu_1 = B_{t1}/\mu_2 - B'_{i1}/\mu_2 \ , \end{cases} \tag{40}$$

where E and B are electric field and magnetic field, respectively, and μ is the permeability. It is known that:

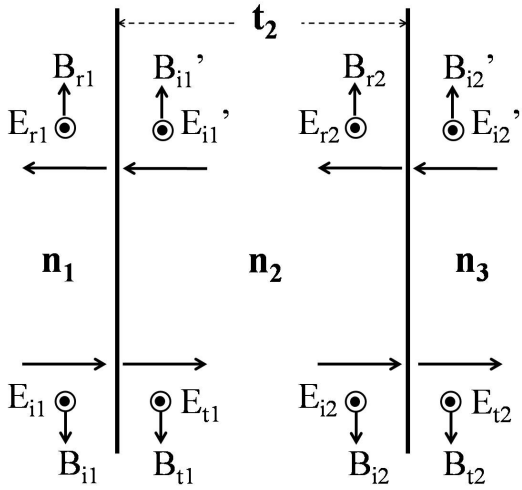

Figure 58: Schematic of electromagnetic wave propagation in the DBR structure.

$$B = \sqrt{\mu\varepsilon}E = n\sqrt{\mu_0\varepsilon_0}E = \gamma E \ , \tag{41}$$

where ε is the permittivity, n is the refractive index and γ is the inverse of the wave velocity in the film. For non-magnetic media, μ is equal to μ_0. So the Eq. 40 can be written as:

$$\begin{cases} E_{i1} + E_{r1} = E_{t1} + E'_{i1} \\ \gamma_1(E_{i1} - E_{r1}) = \gamma_2(E_{t1} - E'_{i1}) \ . \end{cases} \tag{42}$$

Considering the wave propagation in the layer 2, we have:

$$\begin{cases} E'_{i1} = E_{r2}e^{-j\varphi_2} \\ E_{t1} = E_{i2}e^{j\varphi_2}, \end{cases} \tag{43}$$

where the phase difference in the film φ=2πnt/λ_0. So the Eq. 42 can be converted to:

$$\begin{cases} E_{i1} + E_{r1} = E_{i2}e^{j\varphi_2} + E_{r2}e^{-j\varphi_2} \\ \gamma_1(E_{i1} - E_{r1}) = \gamma_2(E_{i2}e^{j\varphi_2} - E_{r2}e^{-j\varphi_2}) \ . \end{cases} \tag{44}$$

Then E_{i1} and E_{r1} at the 1^{st} interface can be expressed as the function of the E_{i2} and E_{r2} at

the 2^{nd} interface:

$$\begin{aligned}\begin{bmatrix} E_{i1} \\ E_{r1} \end{bmatrix} &= \begin{bmatrix} \frac{\gamma_1+\gamma_2}{2\gamma_1}e^{j\varphi_2} & \frac{\gamma_1-\gamma_2}{2\gamma_1}e^{-j\varphi_2} \\ \frac{\gamma_1-\gamma_2}{2\gamma_1}e^{j\varphi_2} & \frac{\gamma_1+\gamma_2}{2\gamma_1}e^{-j\varphi_2} \end{bmatrix}\begin{bmatrix} E_{i2} \\ E_{r2} \end{bmatrix} \\ &= \frac{1}{2}\begin{bmatrix} 1+\frac{\gamma_2}{\gamma_1} & 1-\frac{\gamma_2}{\gamma_1} \\ 1-\frac{\gamma_2}{\gamma_1} & 1+\frac{\gamma_2}{\gamma_1} \end{bmatrix}\begin{bmatrix} e^{j\varphi_2} & 0 \\ 0 & e^{-j\varphi_2} \end{bmatrix}\begin{bmatrix} E_{i2} \\ E_{r1} \end{bmatrix}.\end{aligned} \tag{45}$$

Then $W_{i,i+1}$ can be defined as the refraction term representing the interface between the i^{th} and $(i+1)^{th}$ layer which only relates to the refractive indices of two layers , and U_i is the phase matrix representing the i^{th} layer the wave is propagating through, which relates to the refractive index and optical thickness of the layer.

$$\begin{aligned} W_{i,i+1} &= \frac{1}{2}\begin{bmatrix} 1+\frac{\gamma_{i+1}}{\gamma_i} & 1-\frac{\gamma_{i+1}}{\gamma_i} \\ 1-\frac{\gamma_{i+1}}{\gamma_i} & 1+\frac{\gamma_{i+1}}{\gamma_i} \end{bmatrix} = \frac{1}{2}\begin{bmatrix} 1+\frac{n_{i+1}}{n_i} & 1-\frac{n_{i+1}}{n_i} \\ 1-\frac{n_{i+1}}{n_i} & 1+\frac{n_{i+1}}{n_i} \end{bmatrix} \\ U_i &= \begin{bmatrix} e^{j\varphi_i} & 0 \\ 0 & e^{-j\varphi_i} \end{bmatrix}, \ \varphi_i = 2\pi n_i t_i/\lambda_0 \ , \end{aligned} \tag{46}$$

Considering the incidence term from the substrate to the bottom layer E_{is}=0, the surface incidence and reflection terms are derived to be:

$$\begin{bmatrix} E_{i0} \\ E_{r0} \end{bmatrix} = W_{0,1}U_1W_{1,2}U_2...W_{k-1,k}U_kW_{k,k+1}\begin{bmatrix} E_{is} \\ E_{rs} \end{bmatrix} = \begin{bmatrix} s_{11} & s_{12} \\ s_{21} & s_{22} \end{bmatrix}\begin{bmatrix} 0 \\ E_{rs} \end{bmatrix}. \tag{47}$$

The reflection R is equal to:

$$R = \left|\frac{E_{r0}}{E_{i0}}\right|^2 = \left|\frac{s_{22}}{s_{12}}\right|^2. \tag{48}$$

By giving the refractive indices and thicknesses of each layers in DBRs, the specular reflection on the top surface can be obtained by calculating the elements of transfer matrix. The optical thickness of each layer is normally one-quarter of the wavelength so that one period is equal to $\lambda/2$ to have constructive interference for the reflection on the surface.

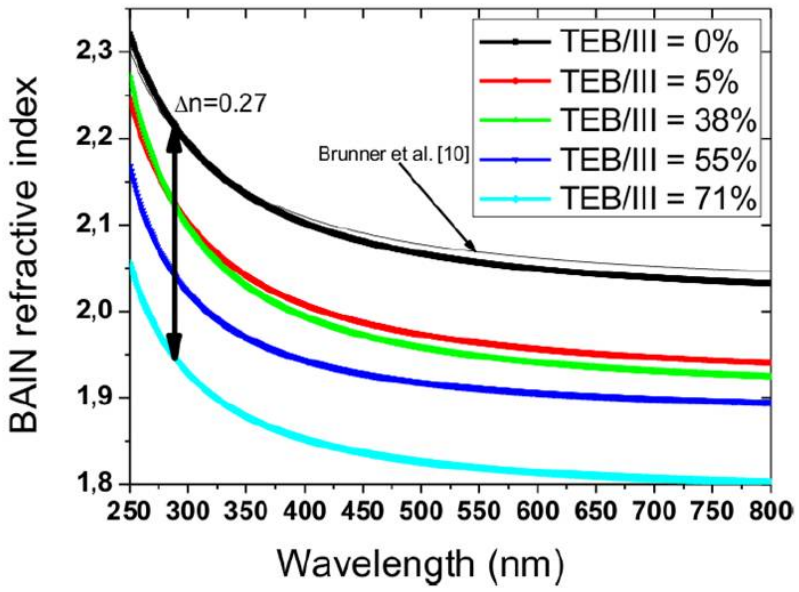

Figure 59: Experimental refractive index of BAlN versus incident wavelength [8, 9].

5.2 Design of BAlN/AlGaN DBRs

The Reflector software has been programmed by Dr. Abid based on the transfer matrix method described in the last section to simulate the reflection of III-nitride epitaxial DBRs in the ideal case [9]. In the software, the refractive indices of AlGaN are derived from the equations reported by Brunner [10]:

$$
\begin{aligned}
n(Al_xGa_{1-x}N) &= \sqrt{C(x) + \frac{A(x)(2 - \sqrt{1+y} - \sqrt{1-y})}{y^2}} \\
C(x) &= -(2.2 \pm 0.2)x + (2.66 \pm 0.12) \\
A(x) &= (3.17 \pm 0.39)\sqrt{x} + (9.98 \pm 0.27) \\
y &= \frac{h\nu}{E_g x} \, .
\end{aligned}
\tag{49}
$$

And the refractive indices of BAlN used in the simulation are experimental values taken from Ref. [9, 64], as shown in Fig. 59.

In this project, BAlN/AlGaN structure is proposed for DBRs reflecting at DUV wavelengths. Compared with the conventional AlGaN/AlGaN structure, it has larger refractive index contrast so that the reflectivity and stopband width can be increased. Additionally,

the tensile strain of BAlN layers can compensate the compressive strain induced in AlGaN layers.

Several factors need to be considered during the design of DBRs. Firstly, large refractive index contrast in the two layers is required, which means more boron in BAlN and more Ga in AlGaN. But this will lead to larger lattice mismatch with the AlN template. Meanwhile, more Ga in AlGaN would lead to more absorption of DUV wavelengths. The number of the periods or the total thickness also needs to be paid attention to. Too thick structure is not favorable for the quality concern, so it would be limited below 20 periods. The last point is that high boron incorporation would be difficult for MOVPE techniques.

In order to avoid absorption by AlGaN band tail states, the composition of AlGaN should be chosen in the way that its absorption coefficient for the targeted wavelength should be below 10^3 cm^{-1}, or the band-edge wavelength is at least 40 nm shorter than the targeted wavelength. The AlGaN absorption coefficient as function of the energy for different Al content is shown in Fig. 60. Based on this criterion, the AlGaN layers should contain more than 70% Al.

Choosing AlGaN layer with 70% and 80%Al, the simulations were done for the structures with different boron compositions in BAlN layers, and with different number of periods of stacks.The results are shown in Fig. 61. It can be seen that in the range of 0 to 15% boron, the reflectivity increases up to 4% boron. After that, the reflectivity keeps constant. Considering all the factors mentioned before, 4% boron was proposed. Also, by this composition, the lattice mismatch between BAlN and AlN is -0.74%, which can almost compensate the compressive strain in AlGaN (around 0.64%). So the proper structure is: 33 nm BAlN containing 4% boron and 28 nm AlGaN containing 70% Al.

The simulation and the design are based on the ideal case and there would be deviations in the real experiments, especially considering the growth challenges and the fact that the quality of the epitaxial layers can significantly affect the DBR performance. In fact, the DBRs with different compositions were performed in the experiments for the studies.

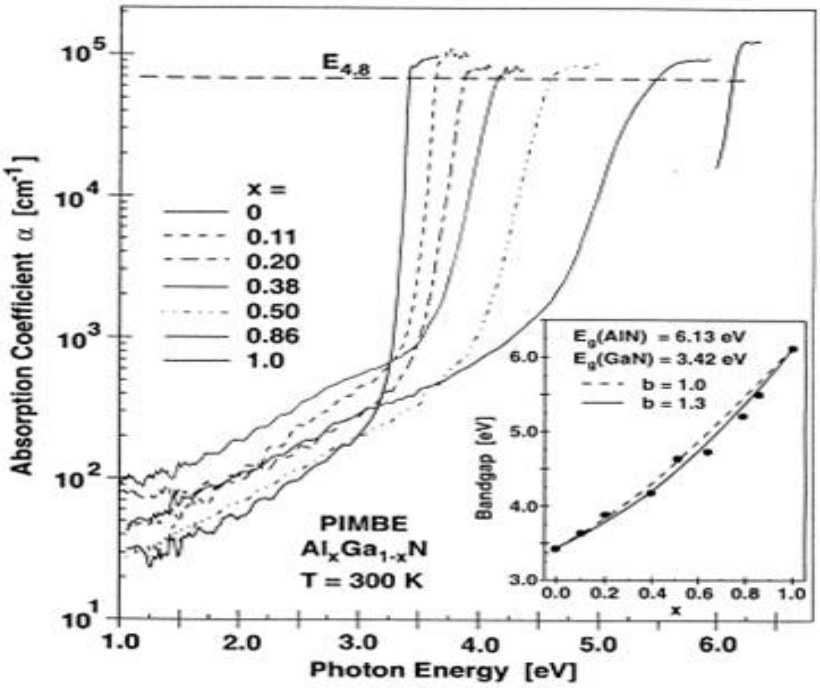

Figure 60: AlGaN absorption coefficient as function of the energy for different Al content [10].

5.3 Simulation of structural quality factors

The simulation in the last two sections is for an idea case and it means that the DBR structure has perfect quality without any roughness, defects or any strain in the layers. However, in the real case, thick DBR structures usually suffer from quality issues. In this section, different factors involving the structural quality and strain state have been input into the simulation and software, in order to understand their influences on the performance of DBRs. The factors considered include roughness (surface and interface roughness) and lattice strain. The methods to introduce those factors are presented in this section and their impacts on the reflecting behavior of DBRs are discussed.

5.3.1 Roughness

The roughness including surface roughness and interface roughness cause light scattering on the surface and interface of the DBRs, which reduces the specular reflectance. To consider the scattering effect at each interface, the large-scale roughness model should be

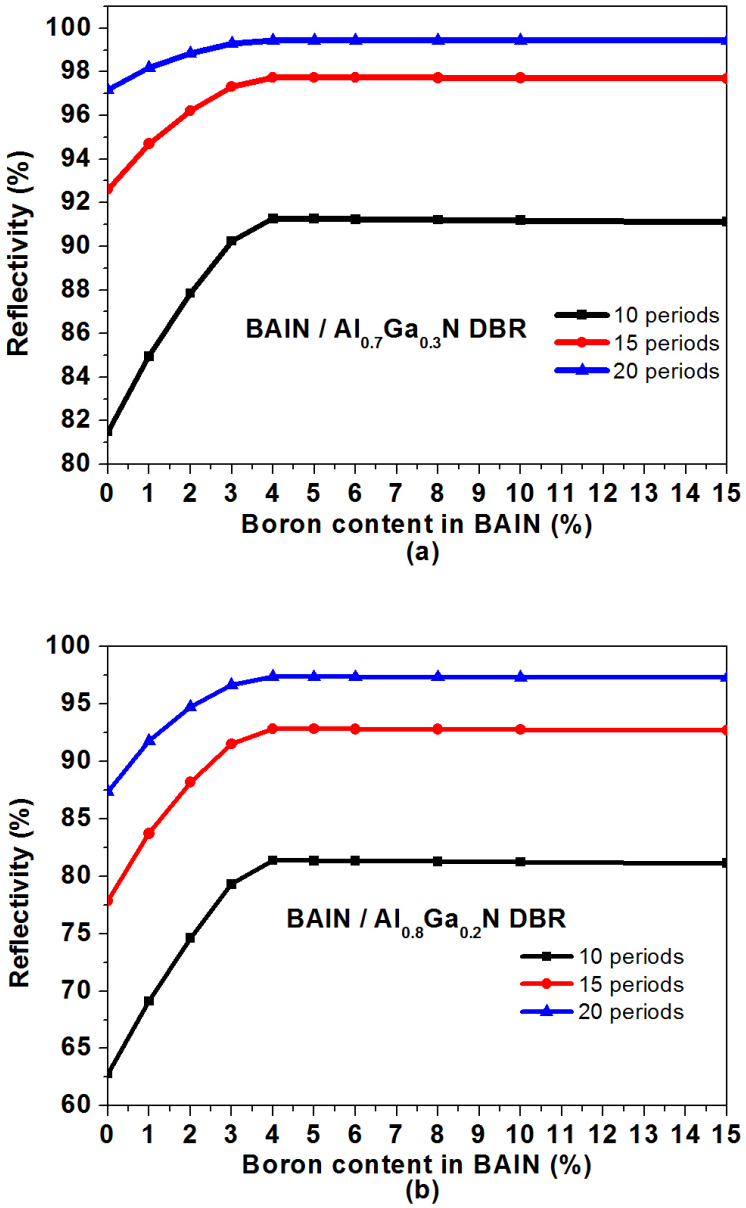

Figure 61: Simulated reflectivity of (a) $B_xAl_{1-x}N/Al_{0.70}Ga_{0.30}N$ structure and (b) $B_xAl_{1-x}N/Al_{0.80}Ga_{0.20}N$ structure.

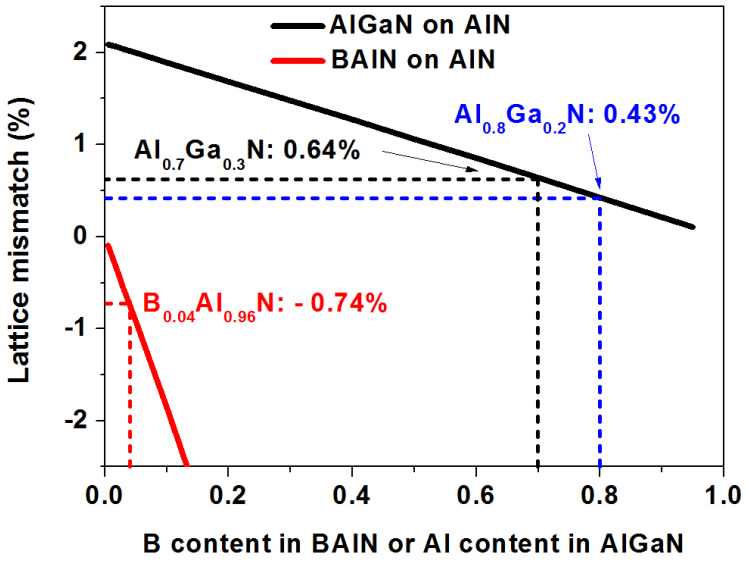

Figure 62: Lattice mismatch of AlGaN/AlN and BAlN/AlN.

applied [172]. The effect of the corresponding roughness harmonic on the amplitude reflection and transmission in Fig. 58 can be described as [172]:

$$\begin{cases} r(w.roughness) = r(w.o.roughness)(1 - 2k^2 n_1^2 \sigma^2) \\ t(w.roughness) = t(w.o.roughness)[1 - 0.5k^2(n_1 - n_2)^2 \sigma^2] \,, \end{cases} \tag{50}$$

where $r = \dfrac{E_{r1}}{E_{i1}}$, $t = \dfrac{E_{t1}}{E_{i1}}$, $k = \dfrac{2\pi}{\lambda}$ and σ is the root mean square roughness (RMS). If it is assumed that $rrms_i = (1 - 2k^2 n_i^2 \sigma^2)$ and $trms_i = 1 - 0.5k^2(n_i - n_{i+1})^2 \sigma^2$, the interface term $W_{i,i+1}$ can be replaced by:

$$W_{i,i+1} = \frac{1}{2} \begin{bmatrix} (1 + \dfrac{n_{i+1}}{n_i}) \dfrac{1}{trms} & (1 - \dfrac{n_{i+1}}{n_i}) \dfrac{rrms}{trms} \\ (1 - \dfrac{n_{i+1}}{n_i}) \dfrac{rrms}{trms} & (1 + \dfrac{n_{i+1}}{n_i}) \dfrac{1}{trms} \end{bmatrix}. \tag{51}$$

Figure 63 shows the simulation results for 20-period $B_{0.04}Al_{0.96}N$ (33 nm) /$Al_{0.70}Ga_{0.30}N$ (28 nm) DBR after inputting roughness values (the surface roughness is considered to be equal to the interface roughness). The roughness can lead to reflectivity reduction, narrower stopband and also phase shift of the reflectance spectrum. The inset of Fig. 63 gives the relationship between the central wavelength reflectivity and the roughness. When the

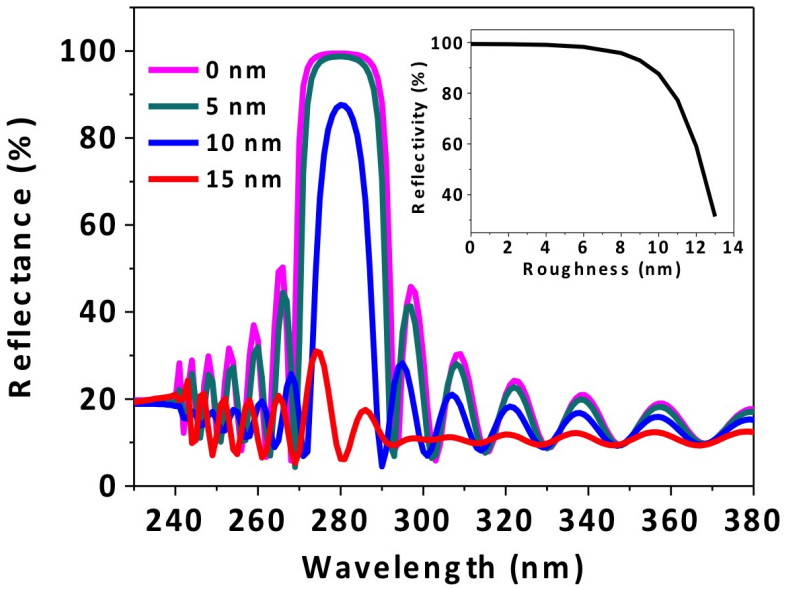

Figure 63: Simulated reflectance of 20-period $B_{0.04}Al_{0.96}N$ (33 nm) /$Al_{0.70}Ga_{0.30}N$ (28 nm) DBR with different values of roughness; Inset shows the curve of the central wavelength reflectivity versus the roughness.

roughness increases from 0 to 6 nm, there is only several percent decrease of the reflectivity. However, when the roughness exceeds 8 nm, the reflectivity of this structure drops dramatically. Therefore, the roughness of the DBR structure needs to be controlled below 6 nm so that it doesn't have significant influence on the DBR performance.

5.3.2 Influence of lattice strain

In order to get a good quality of DBR, the structure is expected to be coherently-strained on the substrate, since the relaxation would lead to dislocations or cracks. In this case, each layer is under compressive or tensile strain. In this subsection, the relation between in-plane strain of the DBR layers and the reflectivity is investigated and discussed.

The first question would be how to input the strain factor in the simulation. The general idea is that: the lattice strain influences the energy gap E_g, and then changes the refractive index of the layer n. It is assumed that the variance of n due to lattice strain ε is relatively small compared with the original value. Thus, the refractive index variance Δn of ternary

material $A_xB_{1-x}N$ can have a linear relationship with the variances of its binary compounds:

$$\Delta n = x \cdot \Delta n(AN) + (1 - x) \cdot \Delta n(BN) \ . \tag{52}$$

Considering the correlation between refractive index, energy gap and lattice strain, this equation can be changed into:

$$\begin{aligned} \Delta n &= x \cdot \frac{\partial n(AN)}{\partial E_g} \Delta E_g(AN) + (1 - x) \cdot \frac{\partial n(BN)}{\partial E_g} \Delta E_g(BN) \\ &= [x \cdot \frac{\partial n(AN)}{\partial E_g} \frac{\partial E_g(AN)}{\partial \varepsilon} + (1 - x) \cdot \frac{\partial n(BN)}{\partial E_g} \frac{\partial E_g(BN)}{\partial \varepsilon}] \Delta \varepsilon \ . \end{aligned} \tag{53}$$

The DBR is a multi-layered structure in which the strain state in each layer is difficult to determine when the structure is relaxed. So the structure is assumed to be pseudomorphically strained. The in-plane lattice of the structure is either equal to the in-plane lattice of the substrate, or it can be obtained by asymmetric RSMs.

Then it needs to find out the equation of parameter "n" in the form of E_g and parameter E_g in the form of strain. As the linear interpolation is taken into account, only equations of binary alloys instead of complex ternaries are required.

A. Hafaiedh [173] has noted that the empirical expression proposed by Herve and Vandamme [174] gives better agreement with known data obtained for refractive indices in the case of III-V semiconductors. And this model is used here:

$$\begin{aligned} n &= \sqrt{1 + (\frac{13.6}{E_g + 3.4})^2} \\ \frac{\partial n}{\partial E_g} &= -\frac{13.6^2}{(E_g + 3.4)^2 \sqrt{(E_g + 3.4)^2 + 13.6^2}} \ . \end{aligned} \tag{54}$$

According to S. Krishnanukutty [175], the change in the energy gap as the function of the strain in a direction can be generally written as:

$$\Delta E_g = \alpha \cdot \varepsilon \ . \tag{55}$$

In a hexagonally symmetric crystal:

$$\alpha = \frac{2a(C_{33} - C_{13})}{C_{33}} = 2a \cdot \frac{1 - 2\nu}{1 - \nu}, \tag{56}$$

Table 9: Parameters used of III-nitrides for Eq. 59

	BN	AlN	GaN
E_g [eV]	5.9	6.28	3.42
ν	0.19 [176]	0.203 [106]	0.183 [106]
E [GPa]	400 [176]	330 [177]	290 [106]
$dE_g/d\varepsilon$ [eV/GPa]	0.006 [178]	0.049 [179]	0.047 [180, 181]

where a is the hydrostatic deformation potential given by:

$$a = -K \cdot \frac{dE_g}{dp}. \tag{57}$$

K is the bulk modulus which can be converted into an expression of Young's modulus E and Poisson ratio ν:

$$K = \frac{E}{3(1-2\nu)}\ . \tag{58}$$

So, the derivative of E_g with respect to the strain can be written as:

$$\frac{dE_g}{d\varepsilon} = -\frac{2E}{3(1-2\nu)} \cdot \frac{1-2\nu}{1-\nu} \cdot \frac{dE_g}{dp} = -\frac{2E}{3(1-\nu)} \frac{dE_g}{dp}\ . \tag{59}$$

For AlN, GaN, BN, the parameters from the literatures are summarized here in Tab. 9.

In this way, the derivative of refractive indices of III-nitrides with respect to the strain

can be obtained:

$$\begin{aligned}
\frac{\partial n(BN)}{\partial E_g(BN)}\frac{\partial E_g(BN)}{\partial \varepsilon} &= -\frac{13.6^2}{(E_g+3.4)^2\sqrt{(E_g+3.4)^2+13.6^2}}\cdot\frac{-2E}{3(1-\nu)}\frac{dE_g}{dp} \\
&= -\frac{13.6^2}{(5.9+3.4)^2\sqrt{(5.9+3.4)^2+13.6^2}}\cdot\frac{-2\cdot 400}{3(1-0.19)}\cdot 0.006 \\
&= 2.91 \\
\frac{\partial n(AlN)}{\partial E_g(AlN)}\frac{\partial E_g(AlN)}{\partial \varepsilon} &= -\frac{13.6^2}{(E_g+3.4)^2\sqrt{(E_g+3.4)^2+13.6^2}}\cdot\frac{-2E}{3(1-\nu)}\frac{dE_g}{dp} \\
&= -\frac{13.6^2}{(6.28+3.4)^2\sqrt{(6.28+3.4)^2+13.6^2}}\cdot\frac{-2\cdot 330}{3(1-0.203)}\cdot 0.049 \\
&= 1.60 \\
\frac{\partial n(GaN)}{\partial E_g(GaN)}\frac{\partial E_g(GaN)}{\partial \varepsilon} &= -\frac{13.6^2}{(E_g+3.4)^2\sqrt{(E_g+3.4)^2+13.6^2}}\cdot\frac{-2E}{3(1-\nu)}\frac{dE_g}{dp} \\
&= -\frac{13.6^2}{(3.42+3.4)^2\sqrt{(3.42+3.4)^2+13.6^2}}\cdot\frac{-2\cdot 290}{3(1-0.183)}\cdot 0.047 \\
&= 0.26\ .
\end{aligned} \tag{60}$$

For the ternary alloys, the expressions are as follows:

$$\begin{aligned}
Al_xGa_{1-x}N:\ \ \Delta n &= [1.60x + 2.91(1-x)]\cdot\Delta\varepsilon \\
B_xAl_{1-x}N:\ \ \Delta n &= [0.26x + 1.60(1-x)]\cdot\Delta\varepsilon \\
B_xGa_{1-x}N:\ \ \Delta n &= [0.26x + 2.91(1-x)]\cdot\Delta\varepsilon\ .
\end{aligned} \tag{61}$$

Figure 64(a) shows the theoretical reflectivity of 20-period AlN/Al_xGa_{1-x}N DBR with different Al content (x) in the AlGaN layer with or without consideration of the strain effect in the simulation. Fig. 64(b) is the same case for 20-period $B_xAl_{1-x}N/Al_{0.7}Ga_{0.3}N$ DBR. It means that the input of the strain effect only leads to a small reduction of reflectivity which is less than 1%. The strain in the layers doesn't affect the reflectivity in an obvious way by influencing the refractive indices. But it should be paid attention to that large strain in the layers may degrade the structural quality and therefore the device performance.

The interface of the reflector software after inputting surface roughness, interface roughness and strain is shown in Fig. 65.

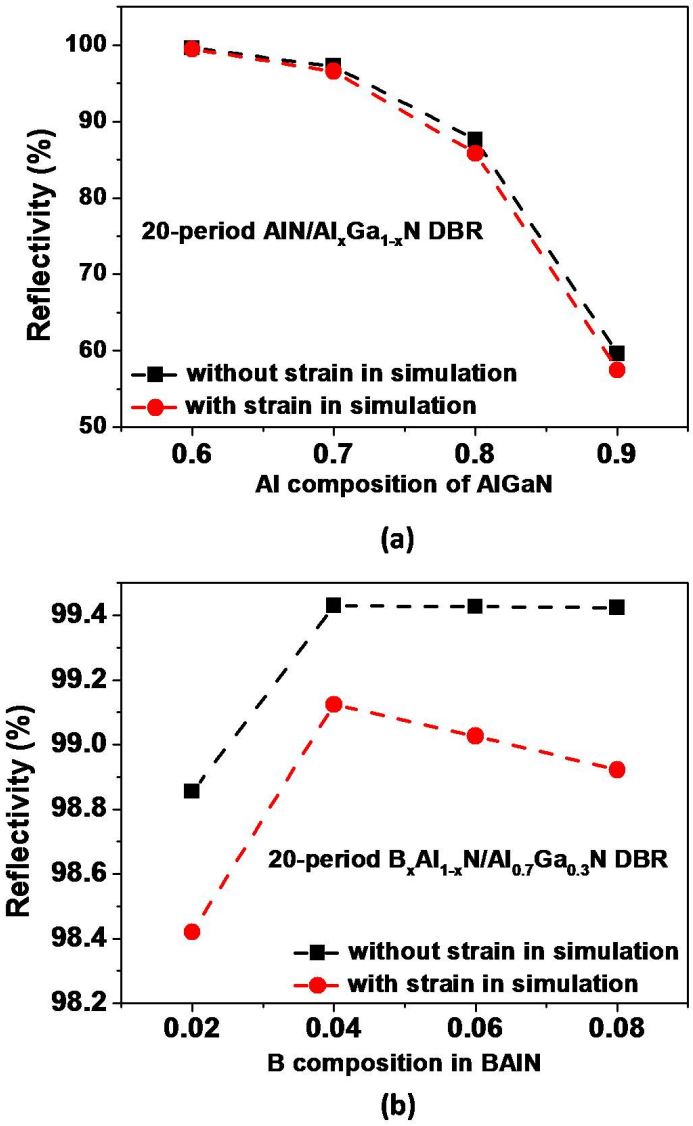

Figure 64: Simulated reflectivity spectra with and without consideration of the strain for (a) 20-period AlN/Al_xGa_{1-x}N DBR and (b) $B_xAl_{1-x}N/Al_{0.70}Ga_{0.30}N$ DBR.

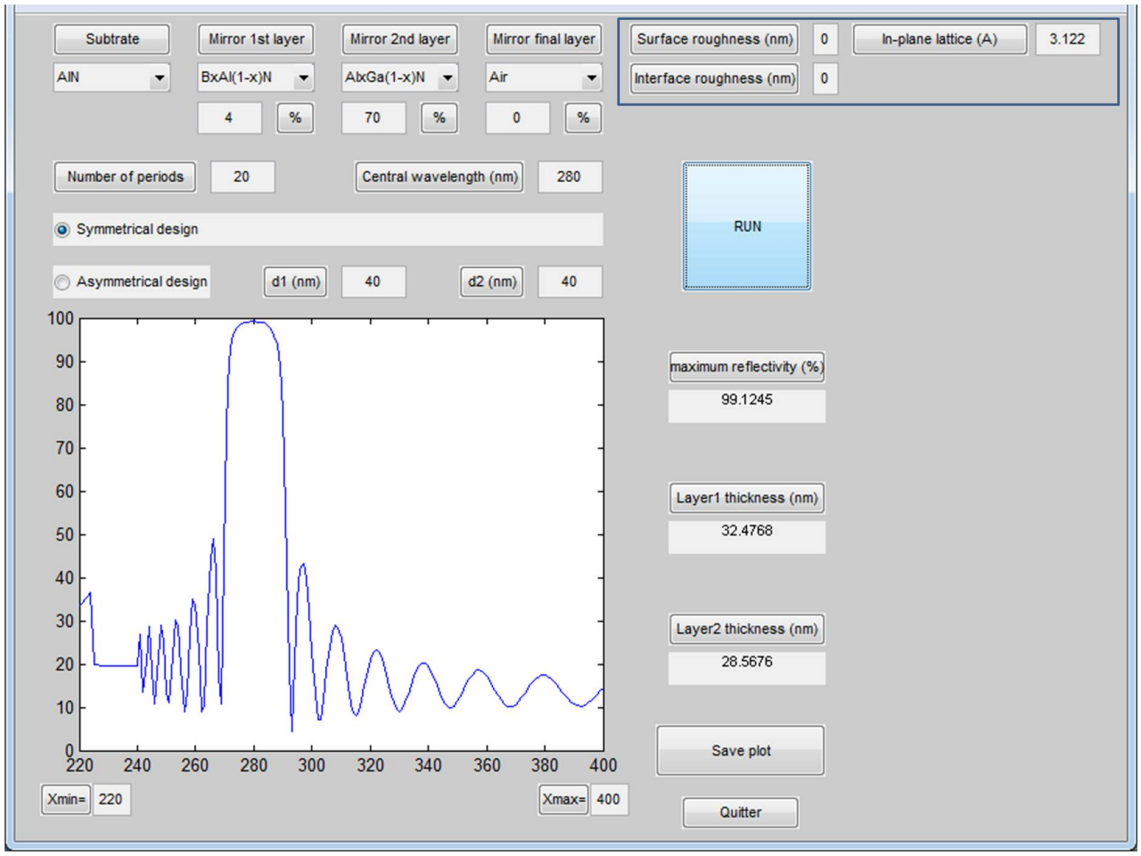

Figure 65: Reflector software interface with factors of surface roughness, interface roughness and strain.

5.4 Realization of BAlN/Al(Ga)N DBRs for DUV

This section describes the realization of BAlN/Al(Ga)N DBRs in T-shape MOVPE reactor. Related characterizations were performed and analyzed. The influences of increasing TEB/III ratio for BAlN layers on structural and optical characteristics of DBRs as well as the influences of replacing AlN layer with AlGaN were studied. The experimental results are also compared with the simulations by using parameters determined from characterizations.

5.4.1 Growth conditions for DBRs

The section 3.2 analyzed structural features of BAlN layers grown at 1000 °C and at low temperature of 650 °C with annealing at 1020°C by FME method. Figure 66 compares the cross-sectional HAADF (BF) images of the BAlN layers or heterostructures grown in those conditions with the heterostructures grown at 1000 °C in a continuous way. By FME method, crystalline quality can be improved since the grain size is increased and columns are formed. But in this case, the interface of BAlN and AlN layers would be destroyed, which can be a disaster for DBR. For example, the structure of 5-period BAlN (32 nm) / AlN (25 nm) didn't have any reflection peak at around 260 nm as it is supposed to.

Meanwhile, by looking into the structure grown at 1000 °C simply in a continuous way (Fig. 66(c)), the BAlN layer is nanocrystalline and the small-size crystallites maintain an accepted interface as well as a clear contrast between two materials. In this work, the DBRs for DUV region have been realized under this condition. More details and analyses of STEM images about the DBR structure are presented in subsection 5.4.3.

5.4.2 BAlN/Al(Ga)N DBRs with reflection at DUV wavelengths

Firstly, a series of 18-pair BAlN/$Al_{0.72\sim0.76}Ga_{0.28\sim0.24}N$ DBRs have been grown. The average growth rate for the BAlN/AlGaN structure is around 2 μm/h. Different TEB/III ratios were used for BAlN layers in order to study the influence of boron incorporation on the performance of DBRs.

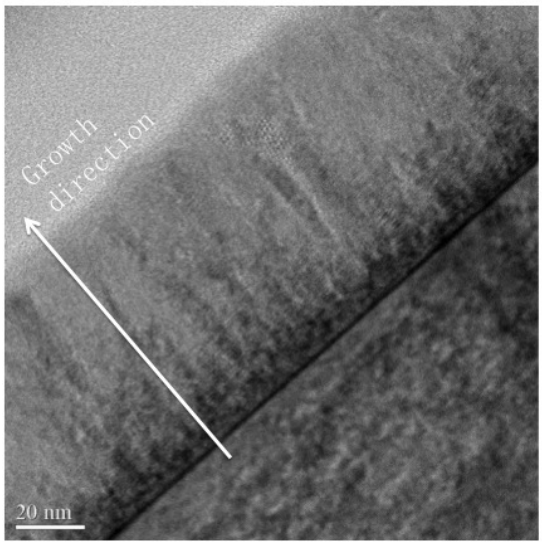

(a) 75 nm BAlN grown at 650 °C and annealed at 1020 °C by FME method

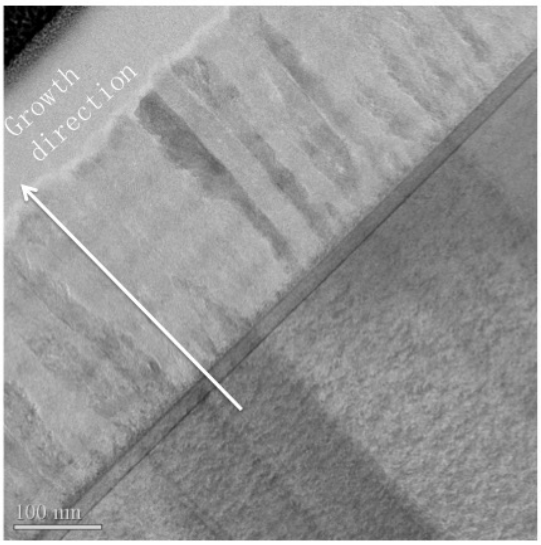

(a) 5-period BAlN (32 nm) / AlN (25 nm) grown at 1000 °C by FME method

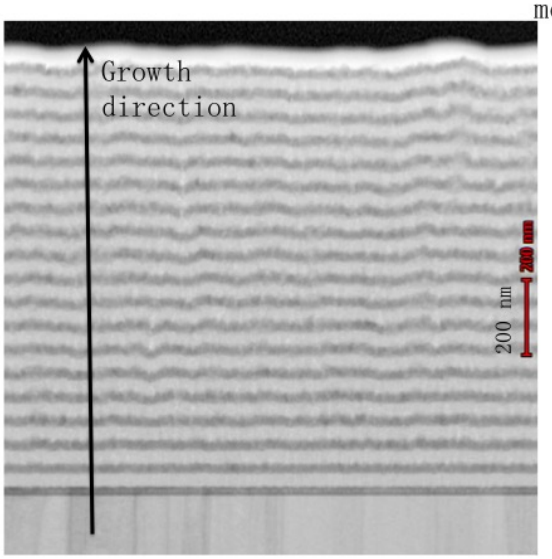

(c) 18-period BAlN (32 nm)/AlGaN (24 nm) grown at 1000 °C in a continuous way

Figure 66: Cross sectional HAADF-STEM (BF) images of (a) 75 nm BAlN grown at 650 °C with annealing at 1000 °C by FME method, (b) 5-pair BAlN (32 nm) / AlN (25) nm grown at 1000 °C by FME and (c) 18-pair BAlN (32 nm) / AlGaN (24 nm) grown at 1000 °C in a continuous way.

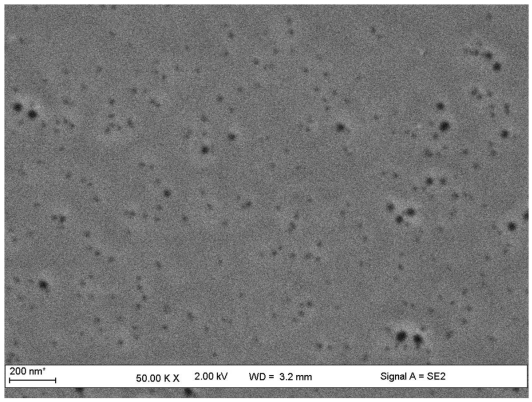

(a) 30 nm $Al_{0.82}Ga_{0.18}N$ on AlN template

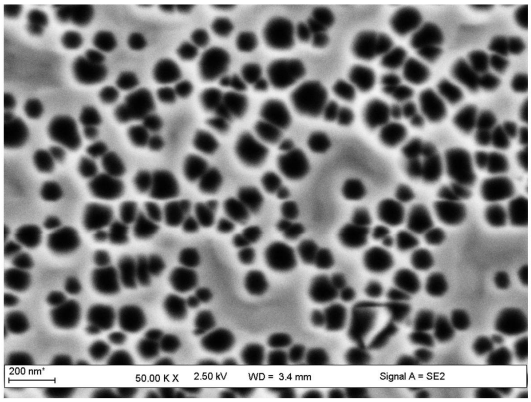

(b) 5-period AlN (30 nm)/ $Al_{0.82}Ga_{0.18}N$ (30 nm) on AlN template

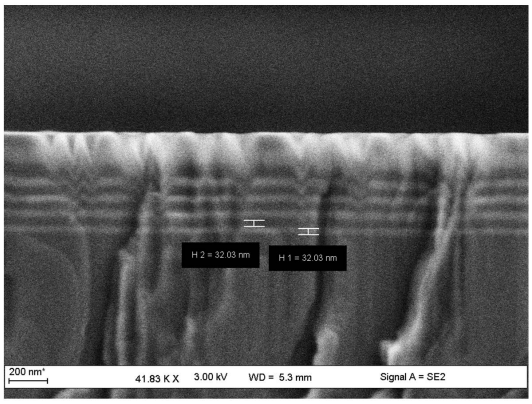

(c) 5-period AlN (30 nm)/ $Al_{0.82}Ga_{0.18}N$ (30 nm) on AlN template (cross-section)

Figure 67: SEM images of (a) 30 nm $Al_{0.82}Ga_{0.18}N$ and (b) 5-period AlN (30 nm) / $Al_{0.82}Ga_{0.18}N$ (30 nm) grown on AlN/sapphire templates; (c) cross-sectional SEM image of the sample in (b).

It is known that the surface of AlN or AlGaN with high Al content (>70% Al for DUV design) would have high density of V-pits due to the low diffusion length of Al atoms and high affinity to oxygen at 1000 °C, as shown in Fig. 67. That's to say, for simple AlGaN/AlN structures, the flat areas apart from pits have 2D morphology, but the surface would be isolated into small islands by the high density pits as shown in Fig. 67(c). The heterostructure growth would occur on the sidewalls of the pits and the island morphology would scatter the light on the surface. For these AlGaN (with more than 70% Al) /AlN DBRs designed for DUV wavelengths, no reflection was obtained.

Figure 68 shows the SEM images, XRD experimental spectra with fittings and reflection spectra of the BAlN/AlGaN DBRs using three different TEB/III ratios. The composition of boron used in the XRD fittings is estimated by assuming that it has a simple linear relationship with TEB/III ratio, and it is 15% for TEB/III=39% according to EDX measurements. When TEB/III=7%, very little boron was introduced into the layer (might be around 2~3%). The morphology of the structure is in the transition stage between 2D morphology isolated by pits and 3D nanocrystalline morphology. For this morphology, no reflection was obtained as what was observed for AlN/AlGaN structures. But the XRD spectrum exhibit good fringes relating to periodicity of heterostructures since it's still maintained monocrystalline.

When the TEB/III ratio was increased, the structure becomes polycrystalline and crystallites spread on the whole surface. In the XRD, only the peak relating to the first monocrystalline AlGaN layer before BAlN growth can be observed, except that there is a small peak at 37.7 ° in the XRD of TEB/III=26% which can be related to (1 -1 0 1) facet of AlGaN.

For TEB/III=26%, 30% reflection was obtained for the central wavelength of 267 nm with a stopband-width of 14 nm. For TEB/III=39%, 55% reflection was obtained for the central wavelength of 279 nm with a stopband-width of 20 nm. The increase of the reflection and stopband-width is due to higher refractive index contrast introduced by more boron incorporation and less absorption at longer wavelength.

DBRs were also grown with a lower growth rate of 500 nm/h, since the low growth rate can increase the mobility of Al and B elements, and hence improve the homogeneity and interface abruptness [182]. The RMS is around 9 nm over 20×20 μm^2 while the RMS of similar structures grown at 2 μm/h is around 16 nm. The experimental reflection spectra along with the simulations of three DBR structures are summarized in Fig. 69. The simulations here only considered ideal case without roughness or strain, and the comparison between experimental data and simulations considering quality factors would be demonstrated in the next subsection. The composition and thickness of AlGaN layers

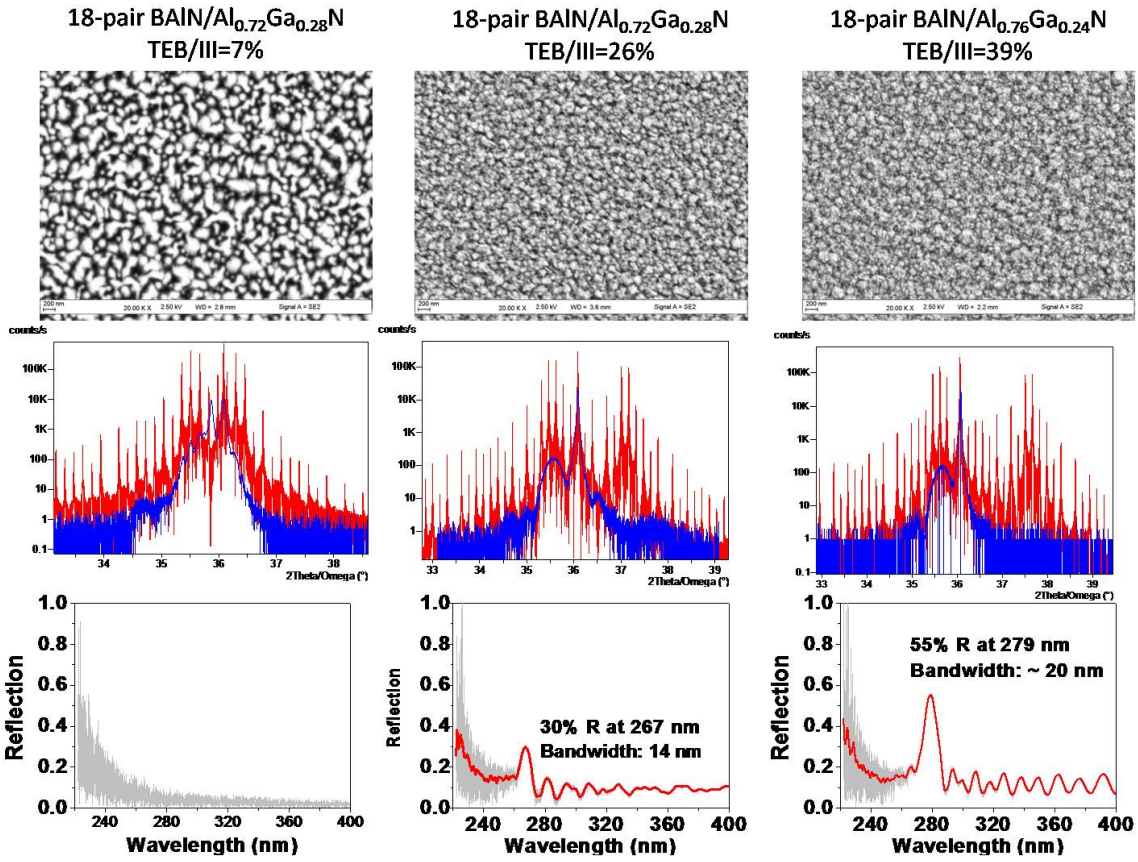

Figure 68: 18-pair BAlN/$Al_{0.72\sim0.76}Ga_{0.28\sim0.24}N$ DBRs with different TEB/III ratios (The composition of boron used in the XRD fittings is estimated by an assumption that it has a linear relationship with TEB/III ratio, and it is 15% for TEB/III=39% according to EDX measurements).

were determined by XRD. The composition and thickness of BAlN were determined by EDX (next subsection) and approximate calculation from reflection peak wavelength (the optical thickness of each layer should be one quarter of the central reflection wavelength). For BAlN/AlN structures, the experimental results are very close to the simulations. From central wavelength of 260 nm to 282 nm, the reflection was increased from 48% to 70%. At central wavelength of 260 nm and 265 nm, by replacing AlN with $Al_{0.8}Ga_{0.2}N$, the reflection was also increased from 48% to 70% and the stopband width was increased from 12 nm to 19 nm (more than 50%) which confirmed better performance of BAlN/AlGaN structure than BAlN/AlN structure. In order to have a simulation more close to the real case, additional characterizations are required to determine the thickness for each layer, boron content, roughness values and so on.

5.4.3 Characterizations of DBRs and reflectance comparison with simulations

Taking the sample in Fig. 69(c) as an example, more structural analyses are presented in this subsection. Experimental reflection spectrum is compared with the simulation in ideal case and with the simulation considering quality factors. The parameters for simulations were obtained from characterizations.

Cross-section STEM images are shown in Fig. 70. It's clear that BAlN layers consist of nanocrystals with size of 2~3 nm instead of forming bigger columns as the ones grown by FME method. The following AlGaN layers inherit this nanocrystalline feature but tends to form bigger grains (5~10 nm) since Ga atoms have larger diffusion length than B atoms. These grains increase the interface roughness (Fig. 70(b)). The thickness is estimated to be 31 nm for BAlN and 27 nm for AlGaN.

EDX mapping and profiles for different elements are shown in Fig. 71 and Fig. 72. Al content in AlGaN calculated by atomic percentage is 81% (±2%) which agrees well with XRD fitting. B content in BAlN is estimated to be 15% (±3%).

AFM image is shown in Fig. 73. The value of room-mean square (RMS) roughness was calculated by scanning over $20 \times 20\ \mu m^2$ to get an average information. The RMS of this

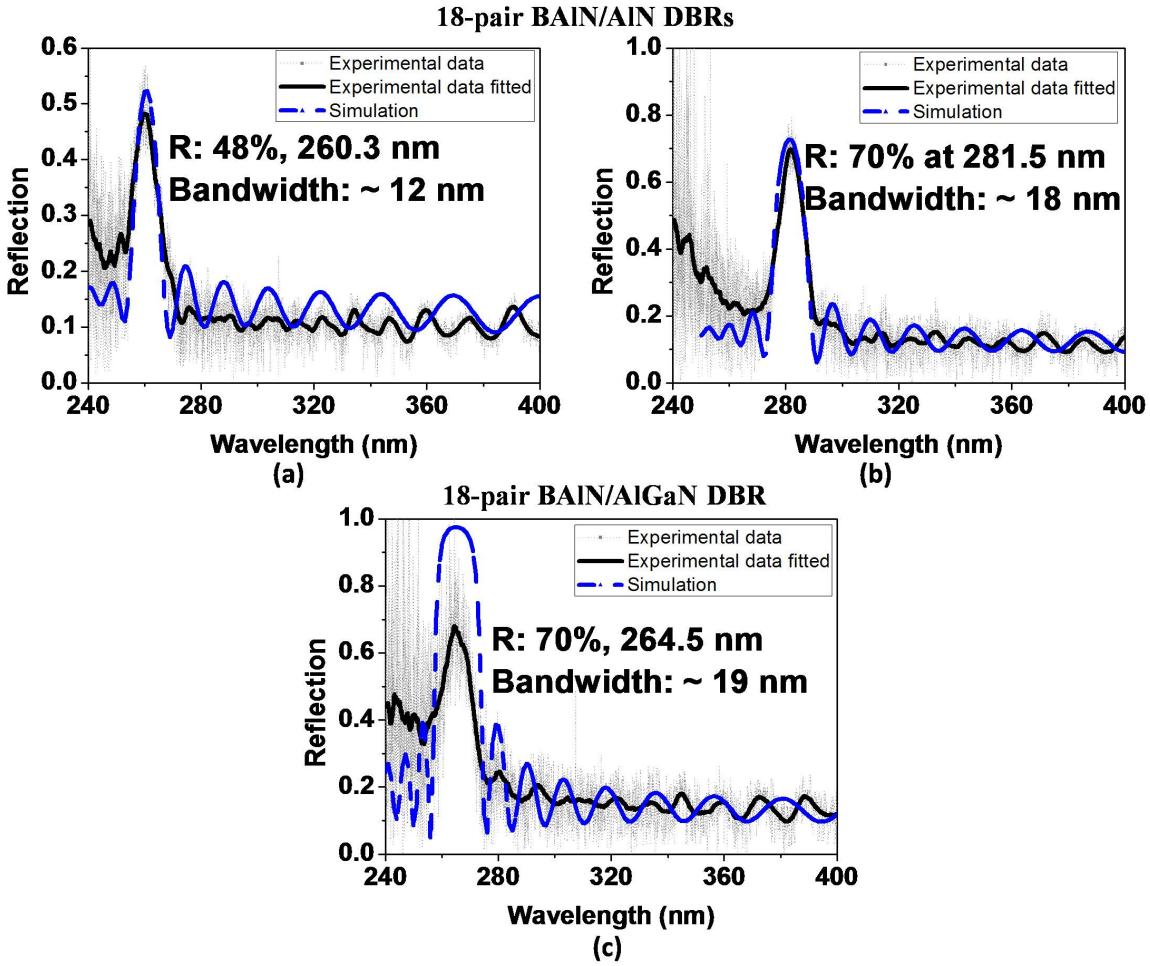

Figure 69: (a) 18-pair BAlN (29 nm) / AlN (29 nm) DBRs reflecting at 260 nm; (b) 18-pair BAlN (33 nm) / AlN (32 nm) DBRs reflecting at 280 nm; (c) 18-pair BAlN (33 nm) / $Al_{0.8}Ga_{0.2}N$ (24 nm) DBRs reflecting at 265 nm.

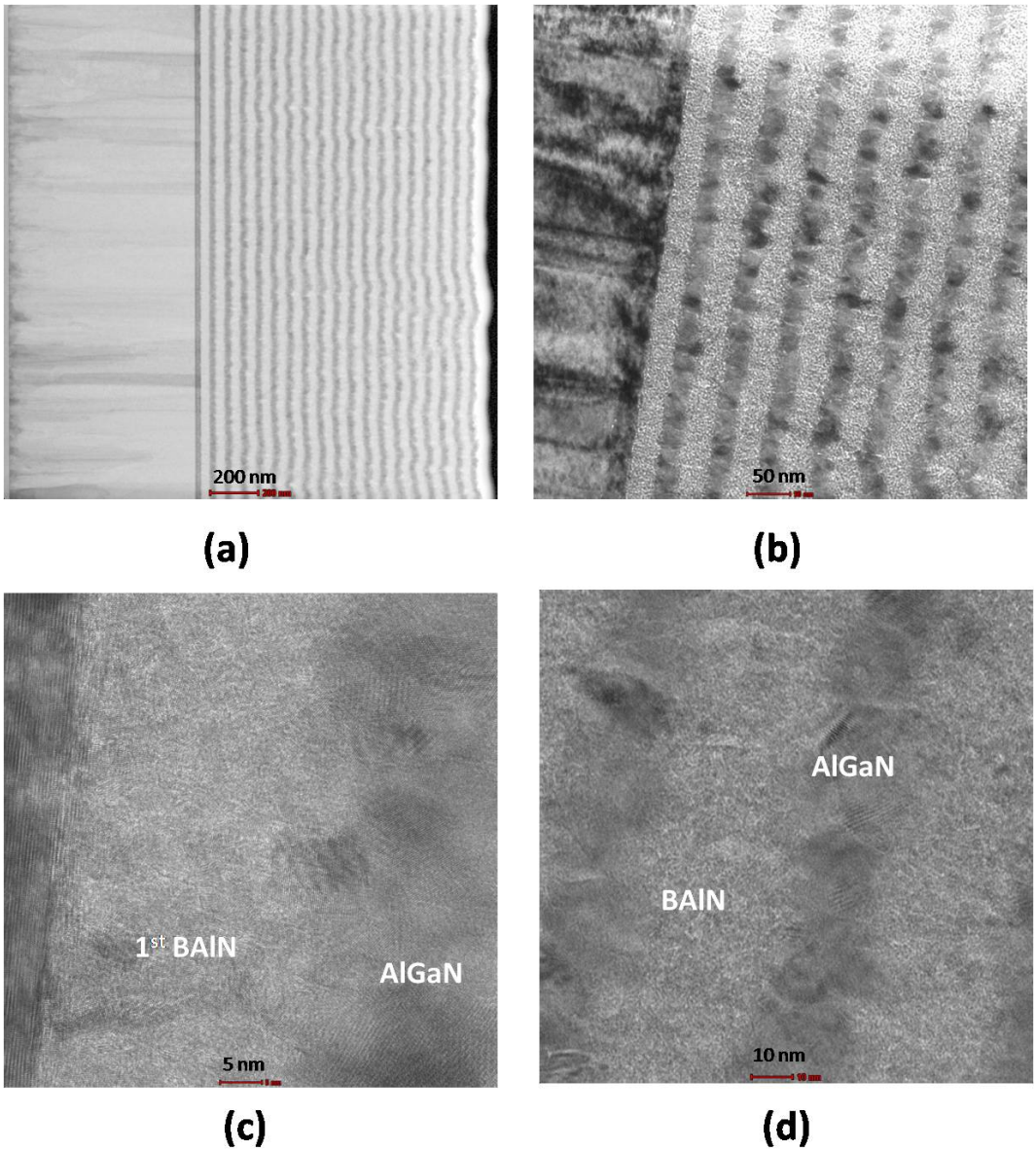

Figure 70: (a) HAADF-STEM (BF) image of 18-pair BAlN/$Al_{0.8}Ga_{0.2}N$ DBRs reflecting at 265 nm. (b), (c) and (d) are TEM images with different magnifications.

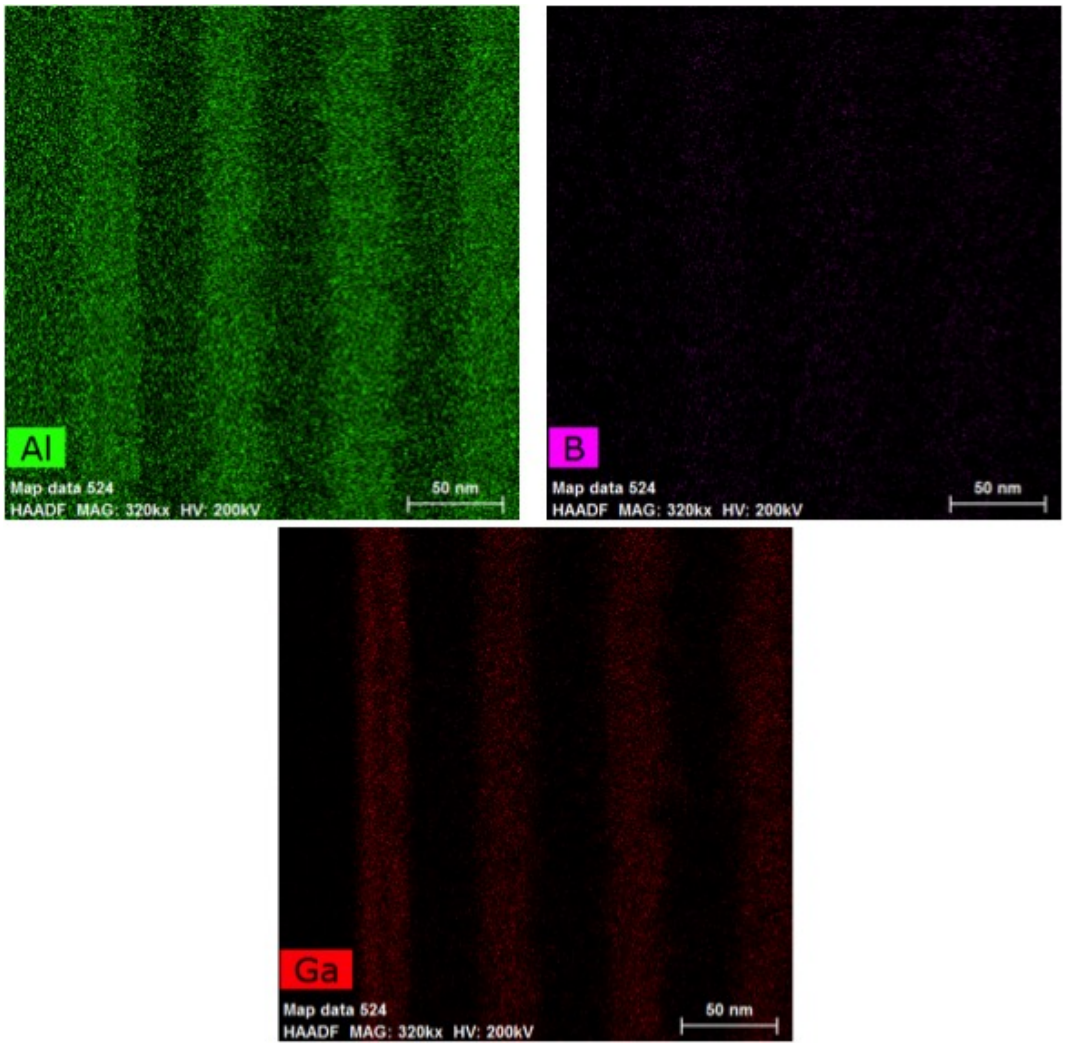

Figure 71: Cross-sectional EDX mapping of 18-pair BAlN/AlGaN DBR reflecting at 265 nm.

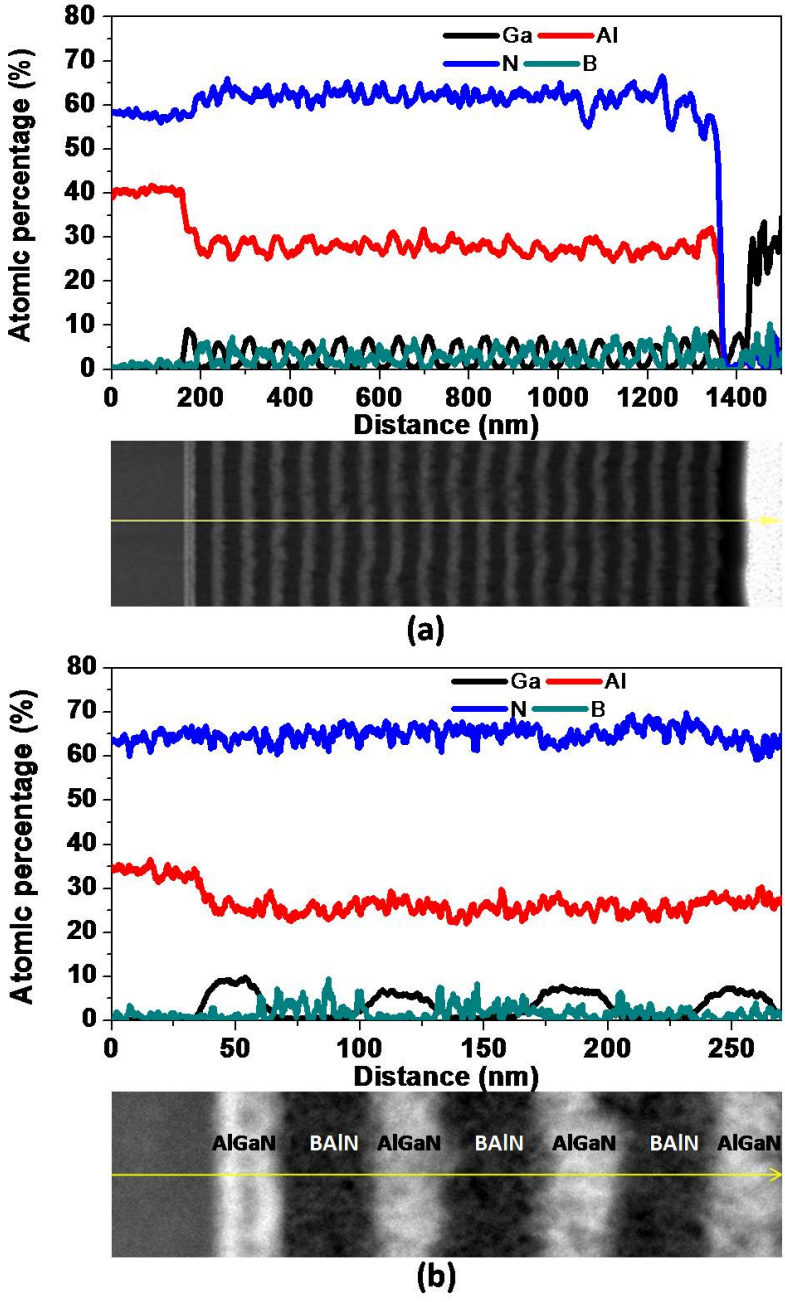

Figure 72: EDX profiles of different elements along the growth direction of 18-pair BAlN/AlGaN DBR structure reflecting at 265 nm with (a) lower and (b) higher magnification.

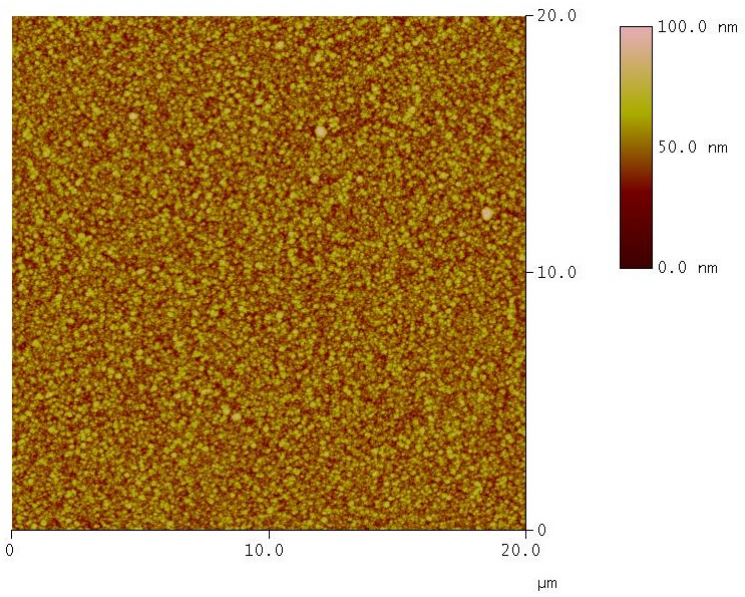

Figure 73: AFM image of 18-pair BAlN/AlGaN DBR reflecting at 265 nm.

DBR is 9.1 nm, and the interface roughness is assumed to be equal to surface roughness. Since BAlN is polycrystalline, the layers are considered to be fully relaxed. Besides, the effect of the strain is pretty weak when compared to the roughness, as discussed in the subsection 5.3.2, so it can also be neglected.

The experimental reflection spectrum and simulations with or without considering quality factors are shown in Fig. 74. The simulations used the compositions and thicknesses determined from characterizations. The theoretical central wavelength of reflection agrees well with the experimental data. The reflection of 70% was obtained experimentally, but the theoretical value for the perfect structure reaches 95%. The quality issues cause this deviation. By considering interface roughness and surface roughness, the reflection peak drops to 75%. The deviation between experimental data and simulation is around 7%.

According to the simulations, the roughness is the main reason which limits the reflectivity. Further studies will be focused on the optimization of BAlN layers to reduce roughness, for example by reducing the boron content in BAlN layers or the possible planarization method. The high quality AlN layers, AlGaN layers with more than 70% Al and BAlN layers with boron content less than 5% will be investigated. The plans are proposed

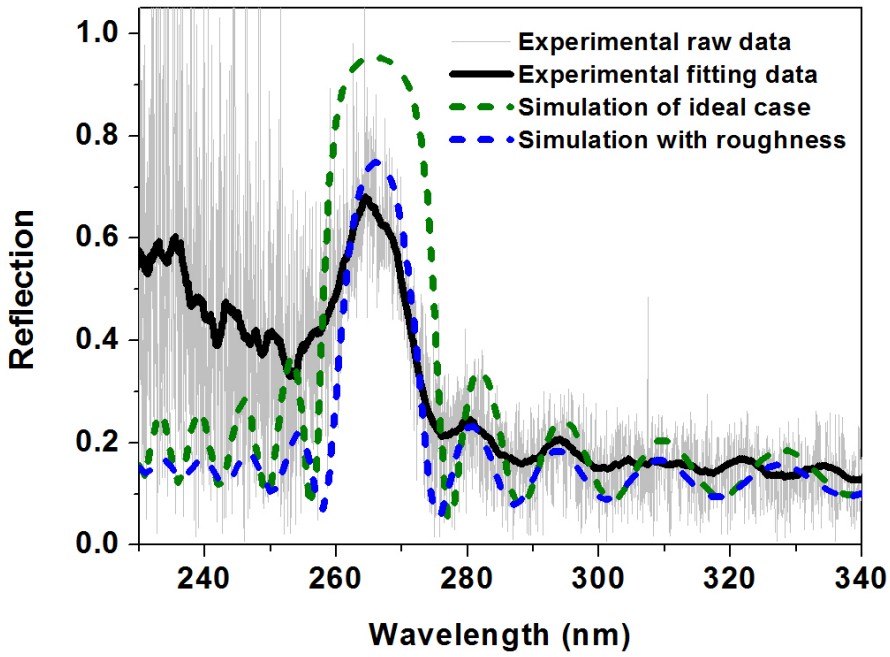

Figure 74: Comparison between experimental reflection spectrum and simulations of 18-pair BAlN/AlGaN DBR reflecting at 265 nm.

in the perspective section in the last chapter.

CHAPTER 6

DEVICE PROCESSING PROGRESS

This chapter presents the progress of the device processing. The time-resolved optical measurements for the active region are shown in the first section. The second section includes the designs of the VCSEL structures, the dielectric DBR properties and the preliminary processing progress with our collaborate lab LPN.

6.1 Time-resolved CL measurements for the active region

10- and 20-period MQWs were planned to be used for device processing. The structural and optical characterizations were analyzed in Section 4.3. The time-resolved cathodoluminescence measurements were performed in École Polytechnique Fédérale de Lausanne (EPFL) and the results are presented in this section. The results of 10-period MQWs are shown in Fig. 75. The mapping of decay time for different wavelengths and the temporally integrated intensity for different wavelengths are in Fig. 75(a) and (b). The main wavelength lies in the range of 270-280 nm.

To describe the carrier dynamics in Fig. 75(c), the bi-exponential decay function was used as in Eq. 62:

$$I(t) = I_0 + A_1 e^{-t/\tau_1} + A_2 e^{-t/\tau_2}, \tag{62}$$

where I is the intensity, t is the time and τ_1, τ_2 are decay carrier lifetimes. In this model, shallow carrier-localization centers and deep carrier localization centers are assumed to exist in AlGaN QWs. A_1 relates to the carrier density captured by shallow ones and A_2 corresponds to deep ones at the initial stage. τ_1 is shorter than τ_2, because the carriers in shallow centers can transfer to deep centers quickly. By fitting the experimental data, the carrier lifetime parameters τ_1 and τ_2 are estimated to be 130 ps and 500 ps, and the faster component takes more than 80% amplitude fraction.

Compared with InGaN MQW structures which usually have decay time in nanosecond

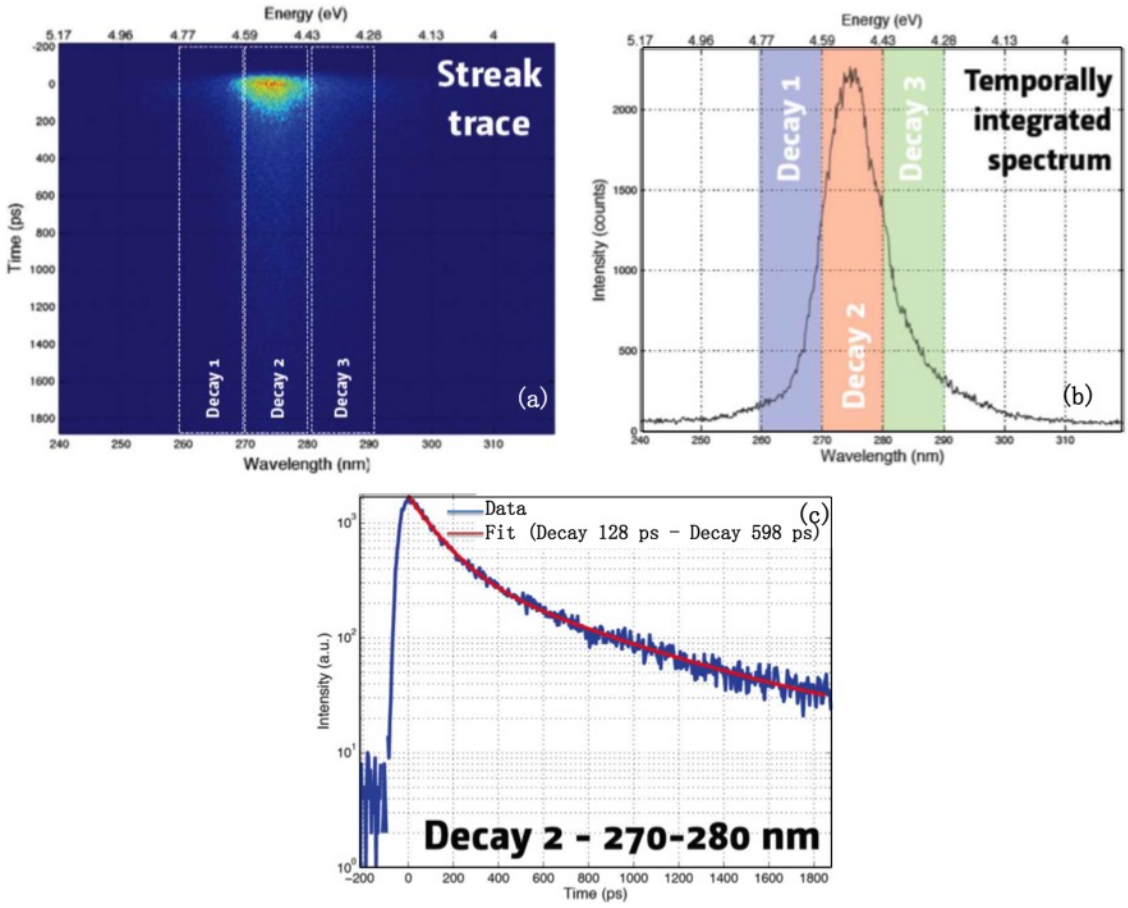

Figure 75: Time-resolved cathodoluminescence measurements at 100 K with excitation of 10 eV (performed in EPFL).

(ns) scale, DUV AlGaN MQWs demonstrate shorter decay time. According to the equation $1/\tau = 1/\tau_{rad}+1/\tau_{non-rad}+1/\tau_{trans}$ (τ_{rad} is radiative lifetime, $\tau_{non-rad}$ is non-radiative lifetime, and τ_{trans} is transfer time toward lower energy levels which can be neglected if the radiative recombination occurs at the bottom of energy levels), one possible reason is the faster non-radiative recombination due to high dislocation density of Al(Ga)N material which decreases $\tau_{non-rad}$. The other possible reasons are the increasing exciton binding energy with increasing Al content and improved oscillator strength which both decrease τ_{rad} [183]. Especially for the case here, the measurements were done at 100 K, and for this sample the IQE is still as high as 90% at this temperature (sample #1 in the Fig. 56). Since the IQE can be described as: $\eta = \frac{\tau_{non-rad}}{\tau_{non-rad} + \tau_{rad}}$, it indicates that the non-radiative process is not significant at this temperature. This gives a hint that the latter reason of decreased radiative lifetime τ_{rad} has dominant contribution.

6.2 Processing progress of device structures

For the device structures, there would be several alternative plans as shown in Fig. 76: (A) AlGaN MQWs sandwiched by dielectric DBRs (Fig. 76(a)); (B) AlGaN active region sandwiched by BAlGaN DBR and dielectric DBR (Fig. 76(b)); (C) if the surface of BAlN/AlGaN is not smooth enough for the following growth of AlGaN active region, the inverted structure can be considered: active region grown directly on the AlN template at first and then BAlN/AlGaN DBR on top of it (Fig. 76(c)), and in this case the cavity would be extended in the substrate.

The device processing has been started with LPN and LASMEA. For DUV lighting, the absorption loss in the sapphire has to be considered. The intracavity loss was estimated based on transmission spectra of KYOCERA c-Al_2O_3 (0 0 01) double-side polished substrates, as summarized in Tab. 10. Therefore, the sapphire substrate of the AlGaN MQW samples has to be partially removed in order to have the cavity length of 30 $\sim$ 100 μm.

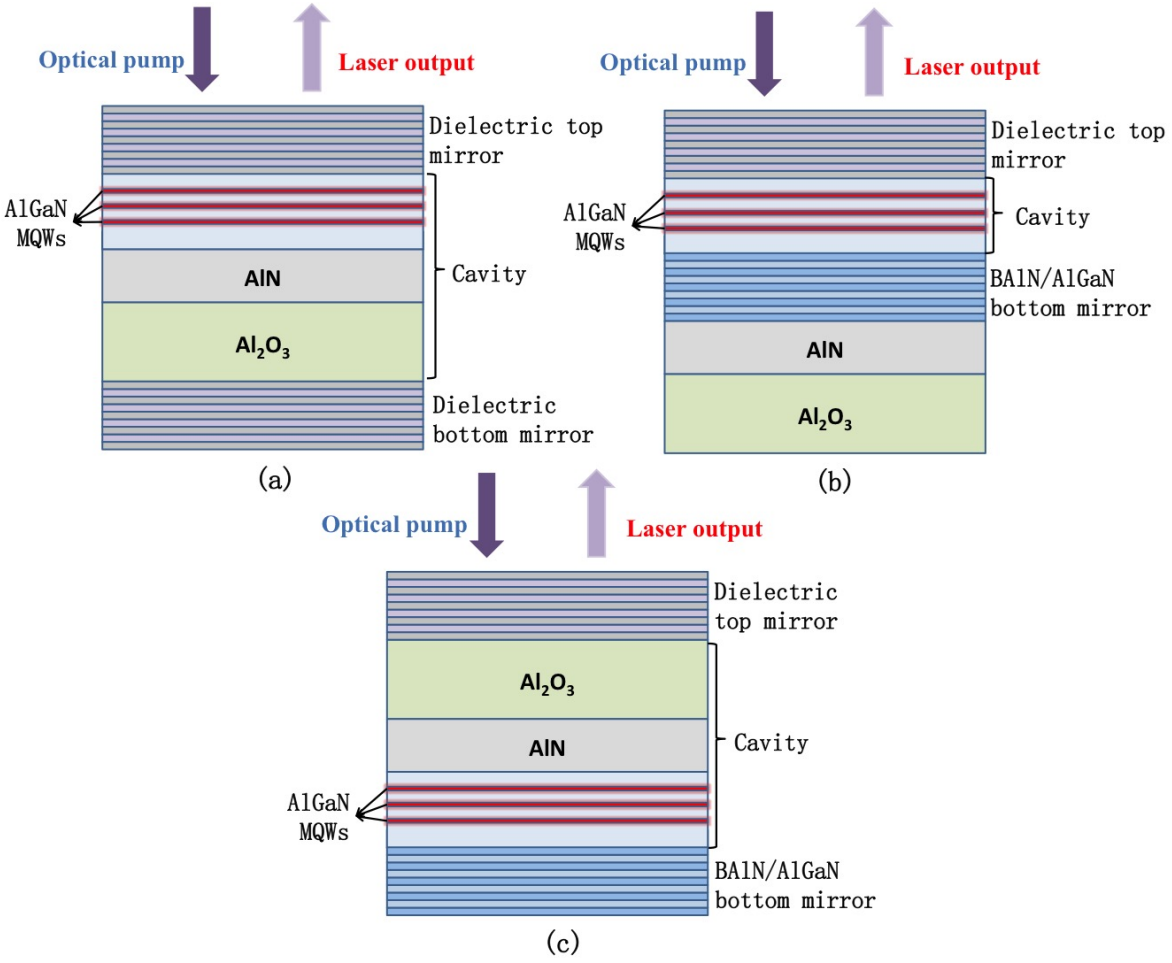

Figure 76: (a) VCSEL design with dielectric top and bottom mirrors; (b) VCSEL design with dielectric top mirror and BAlN/AlGaN bottom mirror; (c) inverted VCSEL structure with BAlN/AlGaN bottom mirror grown on the active region.

Table 10: Experimental absorption loss, critical thickness and cavity free spectra range (FSR) of the sapphire in the cavity.

	Absorption (α)	Critical thickness for intracavity loss < 1%	Cavity FSR
340 nm	0.3 cm^{-1}	100 μm	3 mev
280 nm	0.85 cm^{-1}	30 μm	10 mev

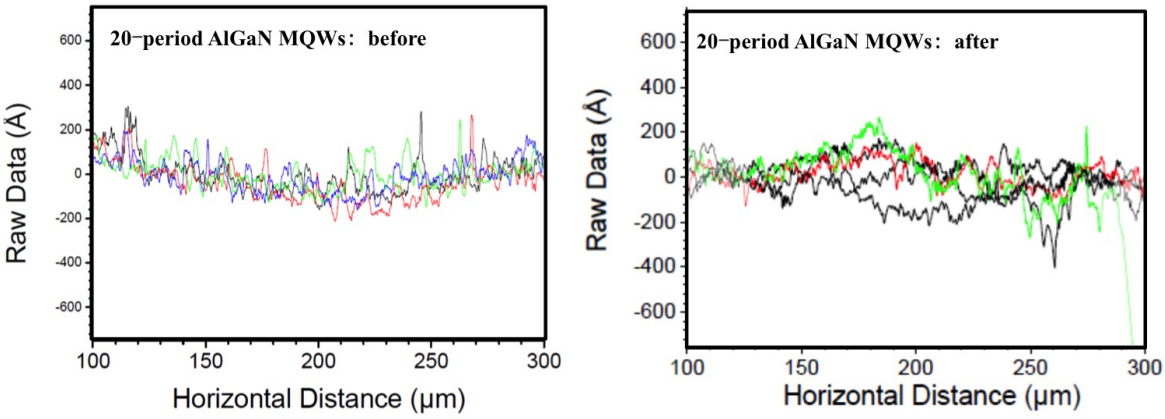

Figure 77: Sapphire thinning down and polishing.

Meanwhile, the backside of the thinned sapphire needs to be polished to reach the roughness below 5 nm.

For the moment, the sample was already thinned to below 100 μm. The large-scale roughness after polishing is 5~7 nm shown in Fig. 77.

For the dielectric DBRs reflecting at DUV region, the halfnium oxid (HfO_2) and silicon oxid (SiO_2) are used for this project. By using this system, a 99% reflection at 250 nm has been reported [184], which indicates it may be adapted to the fabrication of VCSEL at 280 nm. The dielectric DBR deposition is developed and optimized by the group of S. Bouchoule in LPN. The main technique is vacuum (electron beam) evaporation with dual ion beam assistance, Argon (for the control of the material density) and oxygen (for the control of the material stoichiometry). Temperature-controlled deposition is also possible thanks to an IR-lamp in the chamber.

Fig. 78(a) shows the dielectric DBR reflecting in the range from 350 nm to 410 nm fabricated before. The refractive indices were extracted from UV-ellipsometry measurements on thin single layers, and the simulation for the DBR centered at 280 nm using the same HfO_2 / SiO_2 system is demonstrated in Fig. 78(b). Theoretically, 10 pair of alternative layers can achieve 99.3% reflection.

The degrading factor of dielectric DBRs can be the roughness as well as residual absorption. Interface (surface) roughness leads to interface (surface) scattering reducing the

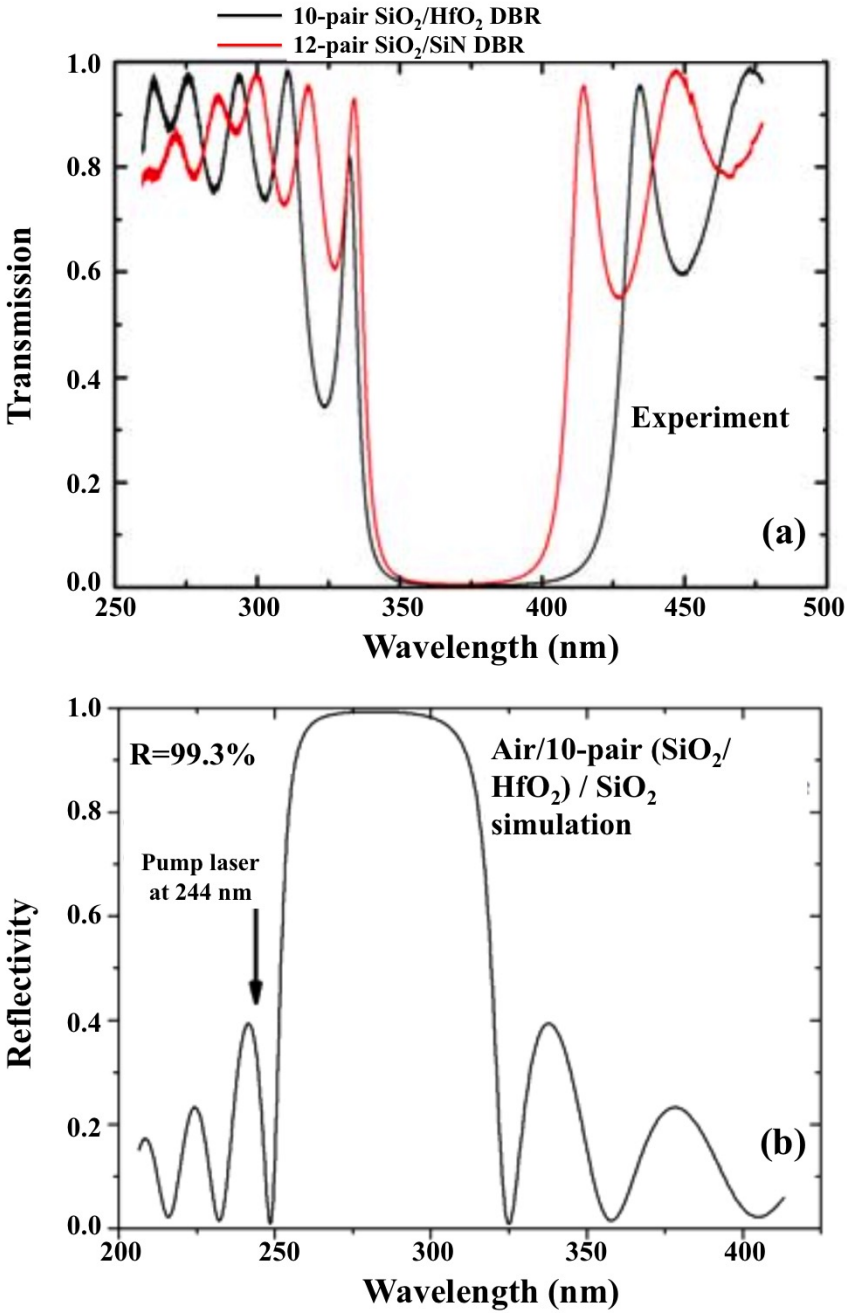

Figure 78: (a) Experimental Transmission spectra of dielectric DBR developed in LPN; (b) Theoretical simulation of dielectric DBR reflecting in DUV region.

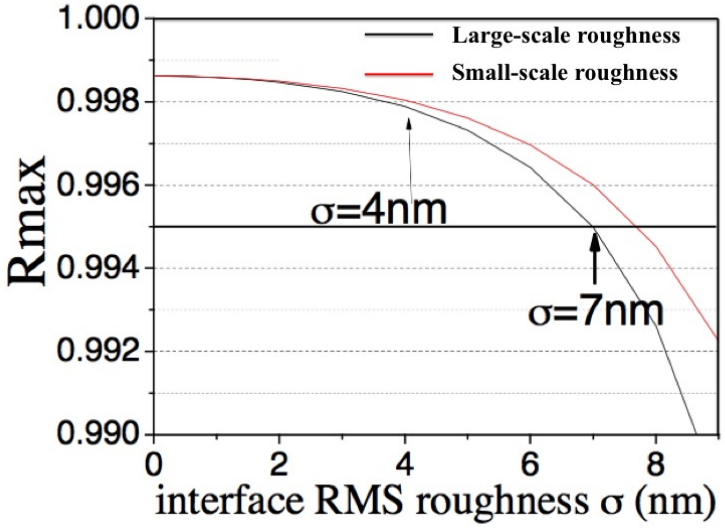

Figure 79: Influence of interface roughness of dielectric DBR.

specular reflection. To evaluate the influence and the critical value of the roughness, the transfer matrix calculation of the reflectivity has been done by including roughness based on both large-scale model considering diffraction loss and small-scale model without considering diffraction loss. As presented in Fig. 79 for 10-pair HfO_2/SiO_2 DBR centered at 300 nm, the roughness effect can be neglected if the root-mean-square (RMS) roughness is controlled to be below 4 nm. AFM characterization of the 10-pair dielectric DBR was performed which is shown in Fig. 80. The accumulated RMS on the surface is below 1 nm over 3 μm $\times$ μm satisfying the requirement.

The cold cavity tests of dielectric DBRs are shown in Fig. 81, and the quality factor (Q factor) is found to be around 500. Since the roughness is not the issue according to the AFM characterization, the low Q factor might be related to the residual absorption. Even though both of the materials are transmissive for the DUV wavelengths up to 250 nm, the extinction coefficient may exceed 10^{-3} due to oxygen vacancies or other sub-band defects. After fitting the experimental data, the extinction coefficient estimated reaches the level of 10^{-3}. In order to achieve Q >1000, the quality of the material can be improved to reduce the extinction coefficient down to 1×10^{-4}.

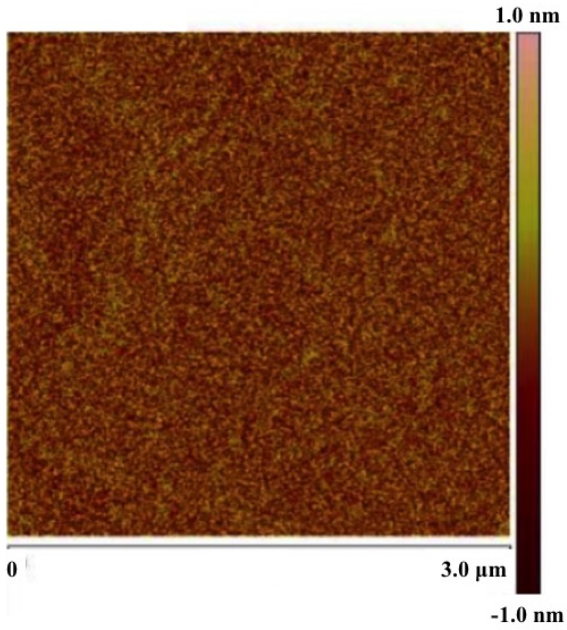

Figure 80: AFM of 10-pair HfO_2 / SiO_2.

The first structure of 20-period AlGaN MQW active region sandwiched by top and bottom dielectric DBRs (8.5-pair HfO_2 / SiO_2) has been done. The reflectivity measurement of the top DBR is shown in Fig. 82. Since the the pumping light goes into the active region through this part, the rule is to maintain a minimum reflectivity at the pumping wavelength (266 nm) and maximum reflectivity at emission wavelength of the MQWs. For this difficulty, the MQWs which have emission close to 300 nm was chosen. The PL spectra in Fig. 82(c) confirm that the emission wavelength of the active region is around 297 nm which can have 98% reflection at the DBR surface, while only around 15% pumping light is reflected. The optical tests will be performed for this structure in LASMEA.

Additionally, an alternative design of the structure in Fig. 76(a) is proposed in Fig. 83, which is a monolithic extended vertical micro-cavity. In this structure, the backside mirror has concave shape in order to compensate the diffraction in the cavity extended in the substrate. The micro-lens patterning in sapphire has been done by inductively coupled plasma (ICP) etching from resist mask using the reflow technique. The AFM image as well as height profile is in Fig. 84. The R_{oc} is 100 ~ 200 μm as designed.

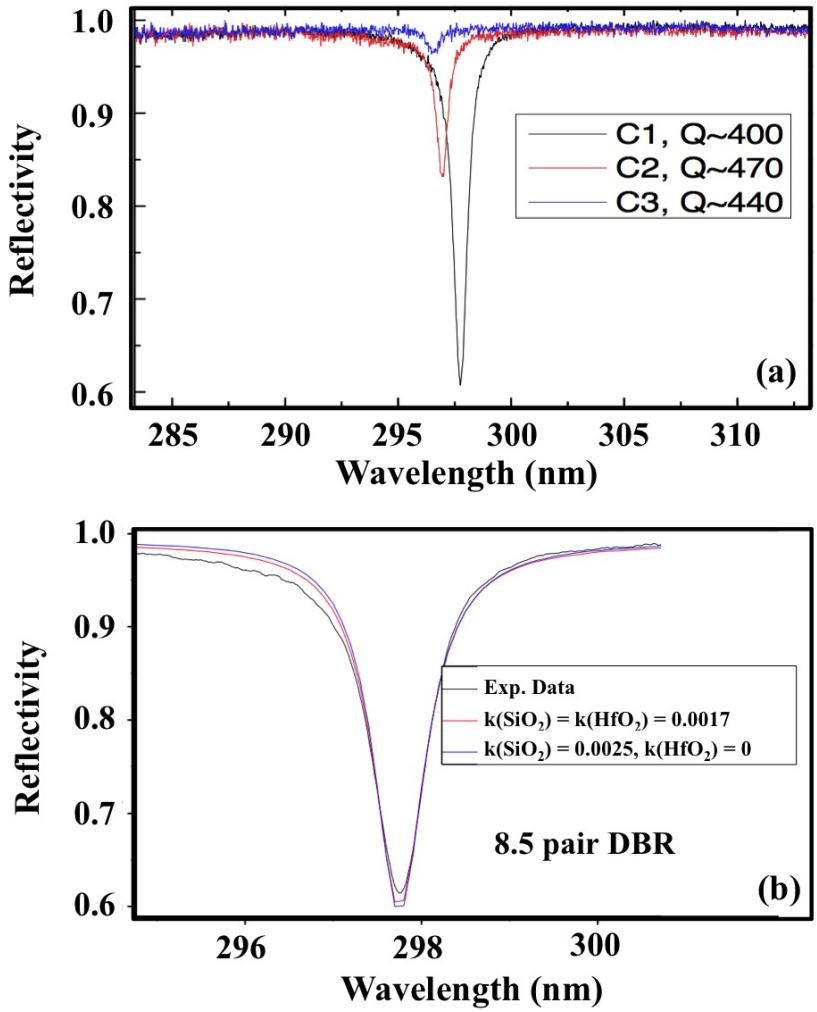

Figure 81: Optical characterization of cold cavity by micro-reflectivity spectrum (C1: 8.5-pair HfO_2 / SiO_2, C2: 10.5-pair HfO_2 / SiO_2, C3: 13.5-pair HfO_2 / SiO_2).

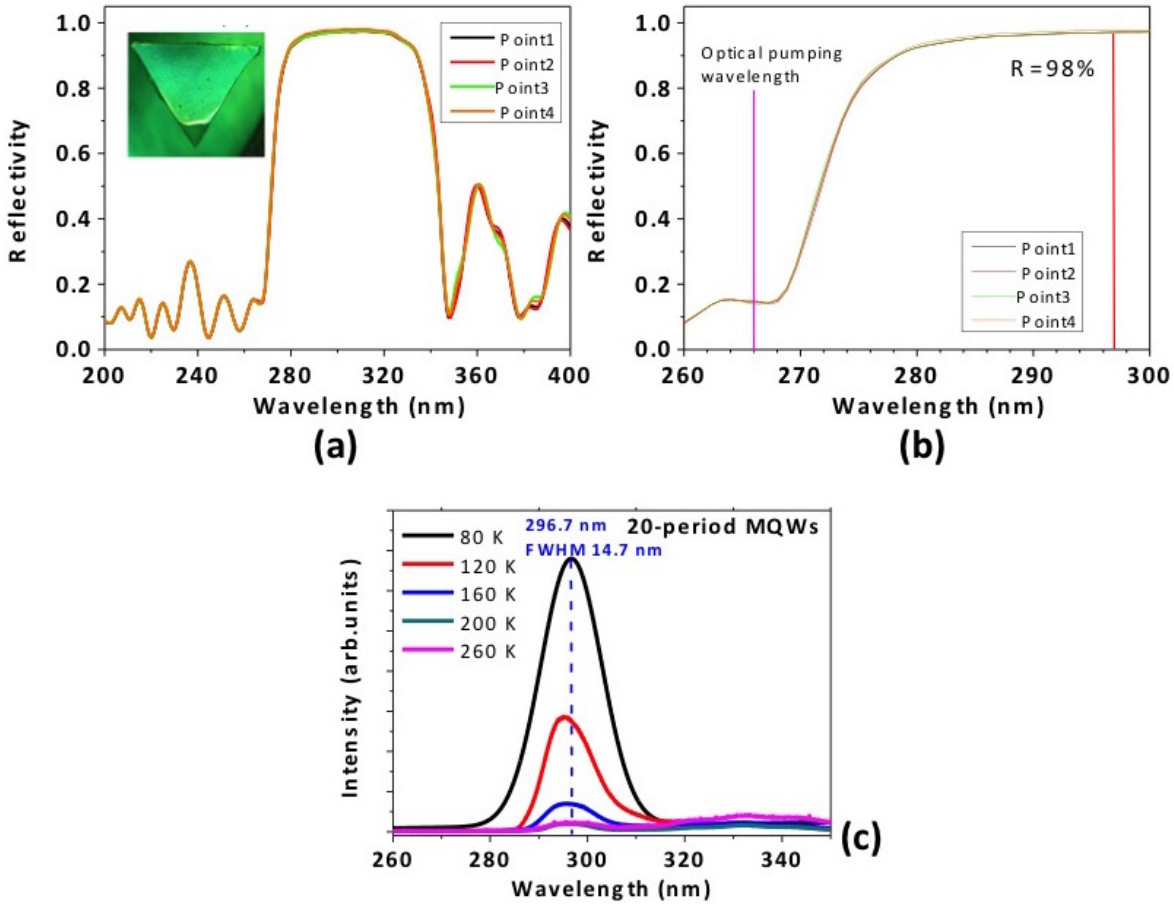

Figure 82: (a) and (b) Reflectivity test of the top dielectric DBR deposited on the 20-period AlGaN MQWs; (c) PL spectra of the AlGaN active region.

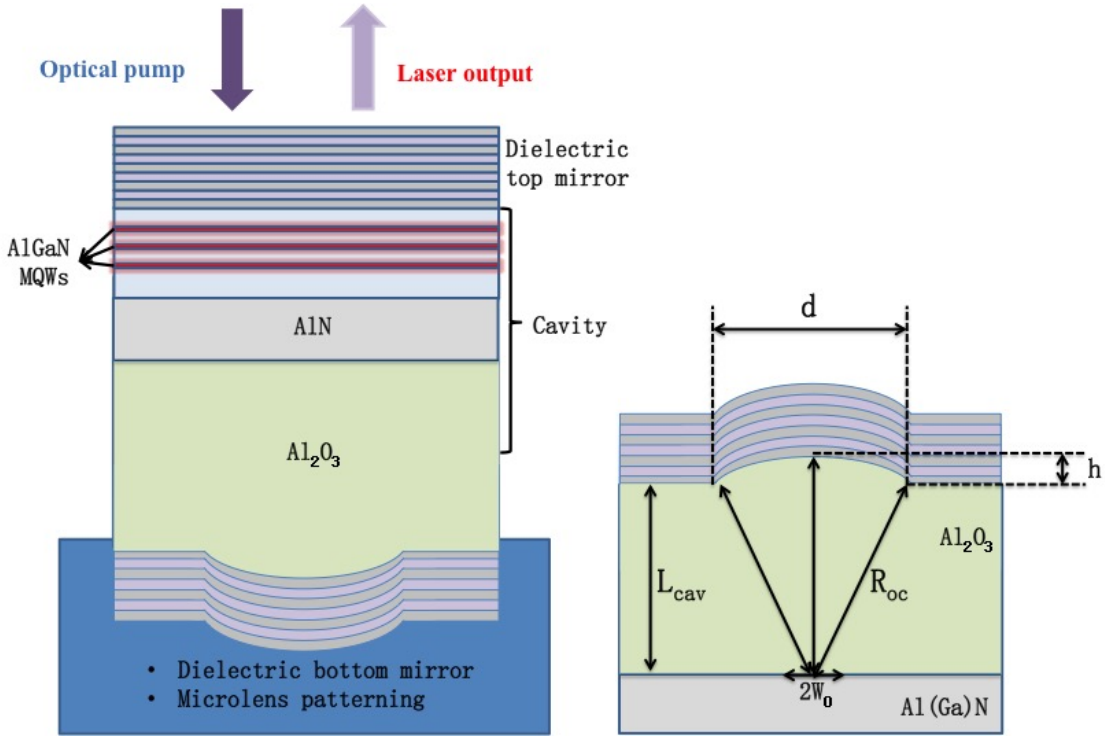

Figure 83: Monolithic extended vertical micro-cavity design.

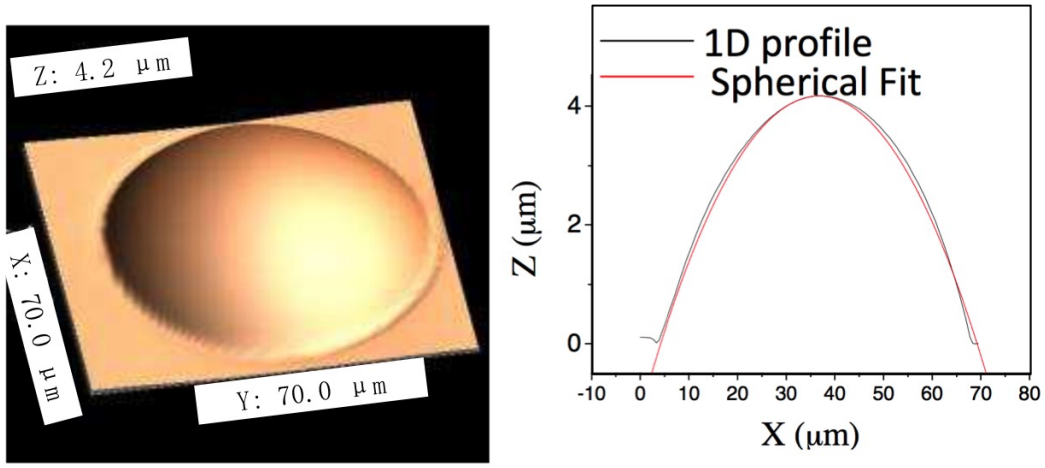

Figure 84: Micro-lens patterning in c-Al_2O_3 by ICP etching from resist mask using the reflow technique.

CHAPTER 7

CONCLUSION AND PERSPECTIVE

7.1 Conclusion

Semiconductor light sources emitting in the deep ultra-violet (DUV) region have numerous applications such as sterilization, water/air purification, optical imaging systems, spectroscopy, and high density storage systems. III-nitride based VCSELs have raised more and more interests in the recent years for the promising properties. However, the realization of VCSELs operating in DUV range needs to satisfy very critical requirements: high emission efficiency of MQWs and highly reflective DBRs which are extremely difficult for the short wavelengths. It means that the AlN substrates should be in good quality with dislocation density less than 10^8 cm^{-2}, QW emission should be TE-polarization dominant (surface emission), two materials constructing DBRs should have high refractive index contrast, and DBR structures should have minimum defects and roughness at the same time. Each of them would be an arduous task.

VCSEL structure has two main blocks: MQWs and DBRs. This work is focused on the MOVPE growth and studies of these two parts for the development of final devices, which includes the growth and characterizations of BAlGaN materials, AlGaN-based DUV MQWs with enhanced TE-polarized emission, and DBRs based on novel BAlN/AlGaN material system.

For AlGaN material, a careful control of composition and relaxation for AlGaN MOVPE growth has been explored. The composition pulling effect in AlGaN grown on AlN templates has been observed and investigated. The critical thickness range of AlGaN under compressive strain grown on AlN is estimated by introducing different methods reported in the literature. Theoretical curves and experimental values have been combined in a chart which can be used as a reference for the experiments. Threading dislocation densities have been calculated based on the XRD measurements and it's an efficient way to quantify the

quality of the layers for comparison without requiring cross-sectional TEM images.

MOVPE growth of BAlN alloys with high boron incorporation has been achieved. The structural and optical properties of 5-period AlN/BAlN heterostructure with 11% boron grown at 1000 °C has been analyzed. Then, growth conditions of low temperature with annealing has been investigated. It was found that low temperature has alleviated boron poisoning during growth under high TEB/III ratio and improved crystallinity to obtain clear XRD peaks corresponding to BAlN, which are very original results concerning this new material. Wurtzite BAlN layers containing as high as 12% boron grown on both GaN and AlN templates exhibit clear XRD peaks. The results for the growth of BAlN material and the study of characteristics can advance prospects for MOVPE-grown boron alloys, which can result in more freedom in bandgap, strain engineering and refractive index engineering for eventual deep-UV sources. The AlN/sapphire templates used for the experiments are from the group of Prof. Dupuis. Recently, the growth of AlN templates has been started by using our new Aixtron CCS reactor. The samples are characterized and analyzed. The dislocation density is reduced to 1.2×10^9 cm^{-2} for the screw component and 3.1×10^{10} cm^{-2} for the edge component with the surface roughness of 0.33 nm. No cracks for visible defects were observed.

For the study of the active region, a 4-period $Al_{0.57}Ga_{0.43}N$ / $Al_{0.38}Ga_{0.62}N$ MQWs structure has been grown on a relaxed $Al_{0.58}Ga_{0.42}N$ buffer on AlN templates. The composition of the quantum wells was optimized so that the strain present in wells is sufficient to enhance TE-polarized (E-field $\perp$ c) emission. The relaxed AlGaN buffer on AlN template serves as pseudo-substrate, and in this way the barriers are almost strain-free which limits the formation of strain-related defects in the quantum wells. The structure exhibits an emission peak at 286 nm with a sharp linewidth at 77 K. Transmission measurements combined with simulations confirm a sufficient oscillator strength leading to an optical absorption coefficient in the wells as high as $3{\times}10^5$ cm^{-1}. The results represent an important step towards the development of DUV light sources, especially surface-emitting LEDs and lasers.

Based on the results of 4-period MQWs, 10- and 20-period MQWs have been grown and characterized, which will be used for the processing of light emission devices by depositing dielectric DBR on the top and at the bottom. Besides, the threading dislocations and V-pits in the QW samples have been characterized and their origin is discussed. The influence of V-pits on the structural quality of the MQWs and on optical emission at 280 nm has also been analyzed. It has been observed that near-surface V-pits were always associated with grain boundaries consisting of edge threading dislocations originating from the AlN/Al_2O_3 interface. Although the high density of V-pits disrupted MQWs growth, it did not affect the internal quantum efficiency which was measured to be ~1% at room temperature even when V-pit density was increased by 30 times. The results help to understand the origin, propagation and effects of the typical defects in AlGaN MQWs grown on AlN/Al_2O_3 templates which may lead to further improvement of the performance of DUV devices.

For the simulation of DUV DBRs, the simulation software based on transfer-matrix methods was developed before in our group, and it assumes that the structure is perfect without any quality degradation. In this work, different quality factors such as surface roughness, interface roughness and strain have been introduced into the simulation and their influence on the performance of DBRs have been discussed. In terms of experiments, different growth conditions for BAlGaN DBRs have been compared and discussed. 70% reflection has been achieved in the DUV region at 260 nm and at 280 nm with stopband width of 19 and 18 nm by using 18-pair BAlN/Al(Ga)N structures. The experimental data are comparable with the simulations considering quality factors. Although it still requires more effort to improve structural quality and surface roughness, the progress achieved can help to develop final DBRs with reflection more than 90% and to apply novel BAlN/AlGaN DBRs for deep UV RC-LEDs and VCSELs.

The alternative designs of VCSEL or RC-LED structures were proposed. The first structure consisting of AlGaN MQWs sandwiched by top and bottom dielectric DBRs was

processed with our collaborate lab LPN. The properties of the MQW active region and dielectric DBRs were characterized. The roughness of the dielectric DBRs was under control while the main problem for this structure lies in the residual absorption of the material, which will be further optimized. The next plans were listed in the perspective section.

In summary, the work of this thesis has made progress on the aspects of MOVPE-grown BAlGaN materials, MQWs emitting at 280 nm and optical investigations, simulation and realization of BAlN/AlGaN DBRs. The work aims at the final DUV devices, and the results obtained can also be helpful and informative for other applications of BAlGaN materials. For the target to realize DUV light sources, on one hand, 10-period and 20-period MQW samples emitting at 280 nm are in the process of depositing highly reflective dielectric DBRs on the top and at the bottom for the vertical cavity. The first tests will be performed after that. At the same time, a new Aixtron 3×2 inch, close coupled showerhead (CCS) MOVPE system has been brought into operation, and the substrate temperature can reach 1300 °C. By this system, AlN/sapphire template and the growth of boron contained material have been initiated. The future research work based on these results has been proposed in the next section.

7.2 Perspective

The perspective of this work covers further improvement of MQW and DBR performances, as well as the processing for final devices. The plans are outlined in this section.

- **Improvement of AlN templates**

The key factor for increasing IQE of DUV MQWs is to reduce dislocation density of AlN substrates. AlN native bulk substrates can be one choice, but it is not commercially available. So it's necessary to grow and optimize AlN/sapphire templates with low dislocation densities and low roughness. The new CCS reactor makes it possible. The preliminary results are shown in the section 3.3. Further improvement can be done by adjusting the strain engineering layers and AlN thickness.

- **Optimization of DBRs**

Based on the optimized AlN layers in CCS reactor, the next steps would be the optimization of AlGaN containing more than 70% Al with minimum pit density and monocrystalline BAlN containing less than 5% B. As explained in Section 3.2.2, low temperature can help to alleviate boron poisoning issue for high boron content. However, for low boron content, the conditions are more close to the AlN conditions and temperature higher than 1100 °C might be favored. By reducing defect density and roughness of both AlGaN and BAlN layers, the performance of BAlN/AlGaN DBRs would be enhanced.

- **Processing of devices**

For the device structures, several alternative plans have been proposed as presented in Section 6.2. The first structure of AlGaN MQWs sandwiched by dielectric DBRs is already finished which will be characterized for its optical properties. The structure can be further improved by reducing the residual absorption in dielectric materials as well as the backside roughness of the sapphire after wafer etching and polishing. Meanwhile, in the aspect of MOVPE growth, after optimizing BAlN/AlGaN DBRs, the following AlGaN active region will be grown and then dielectric DBR will be deposited on the top for the tests of RC-LED and of VCSEL structures. If the surface of BAlN/AlGaN is not smooth enough for the following growth of AlGaN active region, the inverted structure will be considered: active region grown directly on the AlN template at first and then BAlN/AlGaN DBR on top of it.

7.3 Publications and awards

Peer-reviewed articles:

1. X. Li, G. Le Gac, S. Bouchoule, Y. E. Gmili, G. Patriarche, S. Sundaram, P. Disseix, F. Réveret, J. Leymarie, J. Streque, F. Genty, J.-P. Salvestrini, R. D. Dupuis, X.-H. Li, P. L. Voss, and A. Ougazzaden, "Structural and optical investigations of AlGaN

MQWs grown on a relaxed AlGaN buffer on AlN templates emitting at 280 nm," Journal of Crystal Growth, 432: 37-44, 2015.

2. X. Li, S. Sundaram, P. Disseix, G. Le Gac, S. Bouchoule, G. Patriarche, F. Réveret, J. Leymarie, Y. E. Gmili, T. Moudakir, F. Genty, J.-P. Salvestrini, R. D. Dupuis, P. L. Voss, and A. Ougazzaden, "AlGaN-based MQWs grown on a thick relaxed AlGaN buffer on AlN templates emitting at 285 nm," Optical Materials Express, 5(2): 380-392, 2015.

3. X. Li, S. Sundaram, Y. El Gmili, T. Moudakir, F. Genty, S. Bouchoule, G. Patriache, R. Dupuis, P. Voss, J.-P. Salvestrini, and A. Ougazzaden, "BAlN thin layers for deep UV applications," Physica Status Solidi (a), 212(4): 745-750, 2015.

4. X. Li, S. Sundaram, Y. El Gmili, F. Genty, S. Bouchoule, G. Patriache, P. Disseix, F. Réveret, J. Leymarie, J.-P. Salvestrini, R. Dupuis, P. Voss, and A. Ougazzaden, "MOVPE grown periodic AlN/BAlN heterostructure with high boron content," Journal of Crystal Growth, 414: 119-122, 2015.

5. S. Sundaram, X. Li, Y. El Gmili, P. L. Bonanno, R. Puybaret, C. Pradalier, K. Pantzas, G. Patriarche, P. L. Voss, J. P. Salvestrini, and A. Ougazzaden, "Single-crystal nanopyramidal BGaN by nanoselective area growth on AlN/Si(111) and GaN templates," Nanotechnology, 27(11): 115602, 2016.

6. S. Sundaram, R. Puybaret, Y. El Gmili, X. Li, P. L. Bonanno, K. Pantzas, G. Orsal, Z.-H. Cai, G. Patriarche, P. L. Voss, J. P. Salvestrini, and A. Ougazzaden, "Nanoselective area growth and in-depth characterization of dislocation-free InGaN nanopyramids on AlN buffered Si(111) templates," Applied Physics Letters, 107: 113105, 2015.

7. S. Sundaram, R. Puybaret, X. Li, Y. El Gmili, J. Streque, K. Pantzas, G. Orsal, G. Patriarche, P. L. Voss, J. P. Salvestrini, and A. Ougazzaden, "High quality thick InGaN

nanostructures grown by nanoselective area growth for new generation photovoltaic devices," Physica Status Solidi (a), 212(4): 740-744, 2015.

8. S. Sundaram, R. Puybaret, Y. El Gmili, X. Li, P. L. Bonanno, K. Pantzas, G. Orsal, D. Troadec, Z.-H. Cai, G. Patriarche, P. L. Voss, J. P. Salvestrini, and A. Ougazzaden, "Nanoscale selective area growth of thick, dense, uniform, In-rich, InGaN nanostructure arrays on GaN/sapphire template," Journal of Applied physics, 116: 163105, 2014.

Awards:

1. Doctoral Consortium on Photonics, Optics and Lasers Technology 2015 (DCPHOTOPTICS 2015) (Berlin, Germany) - Best Paper Award, 13th March, 2015.

2. European Materials Research Society (E-MRS) 2014 Spring meeting (Lille, France) - Graduate Student Award, 30th May, 2014.

Communications:

1. X. Li, S. Sundaram, Y. El Gmili, S. Bouchoule, G. Patriarche, F. Genty, J-P. Salvestrini, R. D. Dupuis, P.L. Voss, and A. Ougazzaden. "MOVPE growth and characterizations of novel BAlN/AlGaN Bragg mirrors reflecting at 265 nm," 11th International Conference on Nitride Semiconductors (ICNS-11), Beijing, China, 30th August - 4th September 2015. (poster)

2. X. Li, Y. El Gmili, G. Le Gac, S. Sundaram, S. Bouchoule, G. Patriarche, P. Disseix, F. Réveret, J. Leymarie, J. Streque, F. Genty, J-P. Salvestrini, R. D. Dupuis, P.L. Voss, and A. Ougazzaden. "Defects in AlGaN MQWs grown on AlN templates and optical investigations for emission at 280 nm," The European Workshop on Metalorganic Vapour Phase Epitaxy (EWMOVPE 2015), Lund, Sweden, 6th - 10th June 2015. (poster)

3. X. Li, S. Sundaram, P. Disseix, S. Bouchoule, G. Le Gac, G. Patriarche, F. Réveret, J. Leymarie, Y. El Gmili, J. Streque, F. Genty, J-P. Salvestrini, P.L. Voss, R. D. Dupuis, and A. Ougazzaden, "BAlGaN-based Vertical Cavity Surface Emitting Laser Operating in Deep UV Region," Doctoral Consortium of 3rd International Conference on Photonics, Optics and Laser Technology (DCPHOTOPICS2015), Berlin, Germany, 12th - 14th March, 2015. (oral presentation)

4. X. Li, S. Sundaram, Y. El Gmili, F. Genty, S. Bouchoule, G. Patriache, P. Disseix, F. Réveret, J. Leymarie, J.-P. Salvestrini, R. Dupuis, P. Voss, and A. Ougazzaden, "MOVPE grown periodic AlN/BAlN heterostructure with high boron content," 17th International Conference on Metalorganic Vapor Phase Epitaxy (ICMOVPE2014), Lausanne, Switzerland, 13th - 18th July 2014. (poster)

5. X. Li, S. Sundaram, Y.El Gmili, T.Moudakir, P. Disseix, F.Réveret, J. Leymarie, S. Bouchoule, F. Genty, J-P. Salvestrini, R. D. Dupuis, P.L. Voss, A. Ougazzaden, "AlGaN-based multi-quantum wells emitting at 285 nm grown on a thick AlGaN relaxed buffer on AlN template," 17th International Conference on Metalorganic Vapor Phase Epitaxy (ICMOVPE2014), Lausanne, Switzerland, 13th - 18th July 2014. (poster)

6. X. Li, S. Sundaram, Y. El Gmili, T. Moudakir, F. Genty, S. Bouchoule, G. Patriache, R. Dupuis, P. Voss, J.-P. Salvestrini, and A. Ougazzaden, "BAlN thin layers for deep UV applications," European materials society, 2014 SPRING MEETING (E-MRS2014), Lille, France, 26th - 30th May 2014. (oral presentation)

REFERENCES

[1] "http://www.ioffe.ru/SVA/NSM/Semicond/."

[2] "http://www.compoundsemiconductor.net."

[3] "http://en.wikipedia.org/wiki/Wurtzite_crystal_structure."

[4] G. Rakotonanahary, *Spectroscopie des transitions excitoniques dans des puits quantiques GaN/AlGaN*. PhD thesis, Université Blaise-Pascal-Clermont-Ferrand II, 2011.

[5] E. T. Yu, X. Z. Dang, P. M. Asbeck, S. S. Lau, G. J. Sullivan, and I. Introduction, "Spontaneous and piezoelectric polarization effects in III-V nitride heterostructures," *Journal of Vacuum Science & Technology B*, vol. 17, no. 4, pp. 1742–1749, 1999.

[6] R. People and J. C. Bean, "Calculation of critical layer thickness versus lattice mismatch for Ge_xSi_{1-x}/Si strained-layer heterostructures," *Applied Physics Letters*, vol. 47, no. 3, pp. 322–324, 1985.

[7] A. Fischer, H. Kühne, and H. Richter, "New approach in equilibrium theory for strained layer relaxations," *Physical Review Letters*, vol. 73, no. 20, pp. 2712–2715, 1994.

[8] M. Abid, T. Moudakir, Z. Djebbour, G. Orsal, S. Gautier, A. En Naciri, A. Migan-Dubois, and A. Ougazzaden, "Blue-violet boron-based Distributed Bragg Reflectors for VCSEL application," *Journal of Crystal Growth*, vol. 315, pp. 283–287, 2011.

[9] M. ABID, *Design and epitaxial growth of vertical-cavity surface-emitting lasers (VCSEL) emitting at ultraviolet wavelength*. PhD thesis, Georgia Institute of Technology, 2013.

[10] D. Brunner, H. Angerer, E. Bustarret, F. Freudenberg, R. Hopler, R. Dimitrov, O. Ambacher, and M. Stutzmann, "Optical constants of epitaxial AlGaN films and their temperature dependence," *Journal of Applied Physics*, vol. 82, no. 1997, pp. 5090–5096, 1997.

[11] "http://en.wikipedia.org/wiki/Ultraviolet_germicidal_irradiation."

[12] "http://en.wikipedia.org/wiki/Ultraviolet_light_therapy."

[13] "http://en.wikipedia.org/wiki/Ultraviolet_photography."

[14] "http://en.wikipedia.org/wiki/Fluorescence."

[15] "http://en.wikipedia.org/wiki/UV_curing."

[16] "http://en.wikipedia.org/wiki/Optical_storage."

[17] "http://en.wikipedia.org/wiki/Ultraviolet_photography."

[18] H. Hirayama, J. Norimatsu, N. Noguchi, S. Fujikawa, T. Takano, K. Tsubaki, and N. Kamata, "Milliwatt power 270 nm-band AlGaN deep-UV LEDs fabricated on ELO-AlN templates," *Physica Status Solidi (c)*, vol. 6, no. S2, pp. S474–S477, 2009.

[19] K. Nagamatsu, N. Okada, H. Sugimura, H. Tsuzuki, F. Mori, K. Iida, A. Bando, M. Iwaya, S. Kamiyama, H. Amano, and I. Akasaki, "High-efficiency AlGaN-based UV light-emitting diode on laterally overgrown AlN," *Journal of Crystal Growth*, vol. 310, pp. 2326–2329, 2008.

[20] A. Knauer, V. Kueller, U. Zeimer, M. Weyers, C. Reich, and M. Kneissl, "AlGaN layer structures for deep UV emitters on laterally overgrown AlN/sapphire templates," *Physica Status Solidi (a)*, vol. 210, no. 3, pp. 451–454, 2013.

[21] M. Martens, F. Mehnke, C. Kuhn, C. Reich, V. Kueller, A. Knauer, C. Netzel, C. Hartmann, J. Wollweber, J. Rass, T. Wernicke, M. Bickermann, M. Weyers, and M. Kneissl, "Performance characteristics of UV-C AlGaN-Based lasers grown on sapphire and bulk AlN substrates," *IEEE Photonics Technology Letters*, vol. 26, no. 4, pp. 342–345, 2014.

[22] M. E. Hawkridge, Z. Liliental-Weber, H. J. Kim, S. Choi, D. Yoo, J.-H. Ryou, and R. D. Dupuis, "Erratic dislocations within funnel defects in AlN templates for AlGaN epitaxial layer growth," *Applied Physics Letters*, vol. 94, p. 171912, 2009.

[23] L. W. Sang, H. Fang, Z. X. Qin, X. Q. Wang, B. Shen, Z. J. Yang, G. Y. Zhang, X. P. Zhang, L. P. You, and D. P. Yu, "Transmission electron microscopy investigation of inversion domain boundary in $Al_{0.65}Ga_{0.35}N$ grown on AlN/sapphire template," *Applied Physics Letters*, vol. 95, p. 112106, 2009.

[24] F. Mehnke, T. Wernicke, H. Pingel, C. Kuhn, C. Reich, V. Kueller, A. Knauer, M. Lapeyrade, M. Weyers, and M. Kneissl, "Highly conductive n-$Al_xGa_{1-x}N$ layers with aluminum mole fractions above 80%," *Applied Physics Letters*, vol. 103, p. 212209, 2013.

[25] M. L. Nakarmi, K. H. Kim, K. Zhu, J. Y. Lin, and H. X. Jiang, "Transport properties of highly conductive n-type Al-rich $Al_xGa_{1-x}N$ ($x \geq 0.7$)," *Applied Physics Letters*, vol. 85, no. 17, pp. 3769–3711, 2004.

[26] R. Collazo, S. Mita, J. Xie, A. Rice, J. Tweedie, R. Dalmau, and Z. Sitar, "Progress on n-type doping of algan alloys on aln single crystal substrates for uv optoelectronic applications," *Physica Status Solidi (c)*, vol. 8, no. 7-8, pp. 2031–2033, 2011.

[27] D. Nilsson, X. T. Trinh, E. Janzén, N. T. Son, and A. Kakanakova-Georgieva, "On the behavior of silicon donor in conductive $Al_xGa_{1-x}N$ ($0.63 \leq x \leq 1$)," *Physica Status Solidi (b)*, vol. 252, no. 6, pp. 1306–1310, 2015.

[28] T. Kinoshita, T. Obata, H. Yanagi, and S. I. Inoue, "High p-type conduction in high-Al content Mg-doped AlGaN," *Applied Physics Letters*, vol. 102, p. 012105, 2013.

[29] J. Ding, H. Jeon, A. V. Nurmikko, H. Luo, N. Samarth, and J. K. Furdyna, "Laser action in the blue-green from optically pumped (Zn,Cd)Se/ZnSe single quantum well structures," *Applied Physics Letters*, vol. 57, no. 26, pp. 2756–2758, 1990.

[30] B. Gil, *Group III nitride semiconductor compounds*. Series on semiconductor science and technology: 6, Clarendon Press, 1998.

[31] F. G. McIntosh, K. S. Boutros, J. C. Roberts, S. M. Bedair, E. L. Piner, and N. A. El-Masry, "Growth and characterization of AlInGaN quaternary alloys," *Applied Physics Letters*, vol. 68, no. 1, pp. 40–42, 1996.

[32] M. Shatalov, J. Zhang, A. S. Chitnis, S. Member, V. Adivarahan, J. Yang, G. Simin, and M. A. Khan, "Deep ultraviolet light-emitting diodes using quaternary AlInGaN multiple quantum wells," *IEEE Journal of Selected Topics in Quantum Electronics*, vol. 8, no. 2, pp. 302–309, 2002.

[33] "http://www.nobelprize.org/nobel_prizes/physics/laureates/2014/."

[34] I. Akasaki, H. Amano, S. Sota, H. Sakai, T. Tanaka, and M. Koike, "Stimulated emission by current injection from an AlGaN/GaN/GaInN quantum well device," *Japanese Journal of Applied Physics*, vol. 34, pp. 1517–1519, 1995.

[35] J. Han, M. H. Crawford, R. J. Shul, J. J. Figiel, M. Banas, L. Zhang, Y. K. Song, H. Zhou, and A. V. Nurmikko, "AlGaN/GaN quantum well ultraviolet light emitting diodes," *Applied Physics Letters*, vol. 73, no. 12, pp. 1688–1690, 1998.

[36] M. Shatalov, W. Sun, A. Lunev, X. Hu, A. Dobrinsky, Y. Bilenko, J. Yang, M. Shur, R. Gaska, C. Moe, G. Garrett, and M. Wraback, "AlGaN deep-ultraviolet light-emitting diodes with external quantum efficiency above 10%," *Applied Physics Express*, vol. 5, p. 082101, 2012.

[37] M. Ippommatsu, A. Hirano, I. Akasaki, and H. Amano, "Development of AlGaN DUV-LED," in *2013 Conference on Lasers and Electro-Optics Pacific Rim, (Optical Society of America, 2013), paper MH1_3*, 2013.

[38] M. Kneissl, Z. Yang, M. Teepe, C. Knollenberg, O. Schmidt, P. Kiesel, N. M. Johnson, S. Schujman, and L. J. Schowalter, "Ultraviolet semiconductor laser diodes on bulk AlN," *Journal of Applied Physics*, vol. 101, p. 123103, 2007.

[39] H. Tsuzuki, F. Mori, K. Takeda, M. Iwaya, S. Kamiyama, H. Amano, I. Akasaki, H. Yoshida, M. Kuwabara, Y. Yamashita, and H. Kan, "Novel UV devices on high-quality AlGaN using grooved underlying layer," *Journal of Crystal Growth*, vol. 311, no. 10, pp. 2860–2863, 2009.

[40] H. Kim-Chauveau, E. Frayssinet, B. Damilano, P. De Mierry, L. Bodiou, L. Nguyen, P. Vennéguès, J.-M. Chauveau, Y. Cordier, J. Duboz, R. Charash, A. Vajpeyi, J.-M. Lamy, M. Akhter, P. Maaskant, B. Corbett, A. Hangleiter, and A. Wieck, "Growth

optimization and characterization of lattice-matched $Al_{0.82}In_{0.18}N$ optical confinement layer for edge emitting nitride laser diodes," *Journal of Crystal Growth*, vol. 338, no. 1, pp. 20–29, 2012.

[41] H. Yoshida, M. Kuwabara, Y. Yamashita, K. Uchiyama, and H. Kan, "The current status of ultraviolet laser diodes," *Physica Status Solidi (a)*, vol. 208, no. 7, pp. 1586–1589, 2011.

[42] K. H. Li, X. Liu, Q. Wang, S. Zhao, and Z. Mi, "Ultralow-threshold electrically injected AlGaN nanowire ultraviolet lasers on Si operating at low temperature," *Nature Nanotechnology*, vol. 10, pp. 140–144, 2015.

[43] J. Xie, S. Mita, Z. Bryan, W. Guo, L. Hussey, B. Moody, R. Schlesser, R. Kirste, M. Gerhold, R. Collazo, and Z. Sitar, "Lasing and longitudinal cavity modes in photo-pumped deep ultraviolet AlGaN heterostructures," *Applied Physics Letters*, vol. 102, p. 171102, 2013.

[44] N. M. Johnson, B. Cheng, S. Choi, C. L. Chua, C. Knollenberg, J. E. Northrup, M. R. Teepe, T. Wunderer, and Yang Z., "Deep UV AlGaN lasers," in *the 9th International Symposium on Semiconductor Light Emitting Devices, Berlin*, 2012.

[45] H. Hirayama, N. Maeda, S. Fujikawa, S. Toyoda, and N. Kamata, "Recent progress and future prospects of AlGaN-based high-efficiency deep-ultraviolet light-emitting diodes," *Japanese Journal of Applied Physics*, vol. 53, p. 100209, 2014.

[46] H. Hirayama, T. Yatabe, N. Noguchi, T. Ohashi, and N. Kamata, "231-261 nm AlGaN deep-ultraviolet light-emitting diodes fabricated on AlN multilayer buffers grown by ammonia pulse-flow method on sapphire," *Applied Physics Letters*, vol. 91, p. 071901, 2007.

[47] X.-H. Li, T. Detchprohm, T.-T. Kao, M. M. Satter, S.-C. Shen, P. Douglas Yoder, R. D. Dupuis, S. Wang, Y. O. Wei, H. Xie, A. M. Fischer, F. A. Ponce, T. Wernicke, C. Reich, M. Martens, and M. Kneissl, "Low-threshold stimulated emission at 249 nm and 256 nm from AlGaN-based multiple-quantum-well lasers grown on sapphire substrates," *Applied Physics Letters*, vol. 105, p. 141106, 2014.

[48] Y. Tian, J. Yan, Y. Zhang, X. Chen, Y. Guo, P. Cong, L. Sun, Q. Wang, E. Guo, X. Wei, J. Wang, and J. Li, "Stimulated emission at 288 nm from silicon-doped AlGaN-based multiple-quantum-well laser," *Optics Express*, vol. 23, no. 9, p. 11334, 2015.

[49] S. Zhao, A. T. Connie, M. H. T. Dastjerdi, X. H. Kong, Q. Wang, M. Djavid, S. Sadaf, X. D. Liu, I. Shih, H. Guo, and Z. Mi, "Aluminum nitride nanowire light emitting diodes: Breaking the fundamental bottleneck of deep ultraviolet light sources," *Scientific Reports*, vol. 5, p. 8332, 2015.

[50] S. Zhao, X. Liu, S. Y. Woo, J. Kang, G. a. Botton, and Z. Mi, "An electrically injected AlGaN nanowire laser operating in the ultraviolet-C band," *Applied Physics Letters*, vol. 107, p. 043101, 2015.

[51] J. M. Redwing, D. A. Loeber, N. G. Anderson, M. A. Tischler, and J. S. Flynn, "An optically pumped GaN-AlGaN vertical cavity surface emitting laser," *Applied Physics Letters*, vol. 69, no. 1, pp. 1–3, 1996.

[52] I. L. Krestnikov and N. N. Ledentsov, "Photopumped InGaN /GaN/AlGaN Vertical Cavity Surface Emitting Laser Operating at Room Temperature," *Physica Status Solidi (b)*, vol. 216, pp. 511–516, 1999.

[53] Y. Higuchi, K. Omae, H. Matsumura, and T. Mukai, "Room-Temperature CW lasing of a GaN-based vertical-cavity surface-emitting laser by current injection," *Applied Physics Express*, vol. 1, p. 121102, 2008.

[54] B. C. Lin, Y. A. Chang, K. J. Chen, C. H. Chiu, Z. Y. Li, Y. P. Lan, C. C. Lin, P. T. Lee, Y. K. Kuo, M. H. Shih, H. C. Kuo, T. C. Lu, and S. C. Wang, "Design and fabrication of a InGaN vertical-cavity surface-emitting laser with a composition-graded electron-blocking layer," *Laser Physics Letters*, vol. 11, p. 085002, 2014.

[55] D. Kasahara, D. Morita, T. Kosugi, K. Nakagawa, J. Kawamata, Y. Higuchi, H. Matsumura, and T. Mukai, "Demonstration of Blue and Green GaN-Based Vertical-Cavity Surface-Emitting Lasers by Current Injection at Room Temperature," *Applied Physics Express*, vol. 4, p. 072103, 2011.

[56] O. Mitrofanov, S. Schmult, M. J. Manfra, T. Siegrist, N. G. Weimann, A. M. Sergent, and R. J. Molnar, "High-reflectivity ultraviolet AlGaN/AlGaN distributed Bragg reflectors," *Applied Physics Letters*, vol. 88, p. 171101, 2006.

[57] E. Feltin, J. F. Carlin, J. Dorsaz, G. Christmann, R. Butt, M. Laügt, M. Ilegems, and N. Grandjean, "Crack-free highly reflective AlInN/AlGaN Bragg mirrors for UV applications," *Applied Physics Letters*, vol. 88, p. 051108, 2006.

[58] C. G. Moe, Y. Wu, J. Piprek, S. Keller, J. S. Speck, S. P. DenBaars, and D. Emerson, "AlGaN/AlN distributed bragg reflectors for deep ultraviolet wavelengths," *Physica Status Solidi (a)*, vol. 203, no. 8, pp. 1915–1919, 2006.

[59] A. R. Getty, A. David, Y. Wu, C. Weisbuch, and J. S. Speck, "Demonstration of Distributed Bragg Reflectors for Deep Ultraviolet Applications," *Japanese Journal of Applied Physics*, vol. 46, no. 32, pp. 767–769, 2007.

[60] L. Zhang, K. Dong, D. Chen, Y. Liu, J. Xue, H. Lu, R. Zhang, and Y. Zheng, "Solar-blind ultraviolet AlInN/AlGaN distributed Bragg reflectors," *Applied Physics Letters*, vol. 102, p. 242112, 2013.

[61] L. Zhang, Z.-H. Liu, X.-G. Huang, Q.-F. LI, R. Zhang, Z.-L. Xie, and X.-Q. Xiu, "Properties of an AlGaN/AlN distributed-Bragg-reflector structure," *Journal of Korean Physical Society*, vol. 65, no. 7, pp. 1101–1105, 2014.

[62] M. P. Hoffmann, A. Franke, M. Bobea, F. Kaess, R. Kirste, A. Dadgar, A. Strittmatter, M. Gerhold, R. Collazo, and Z. Sitar, "High reflective AlN/AlGaN distributed

Bragg reflectors for UV microcavity lasers," *Gallium Nitride Materials and Devices II, Proc. of SPIE*, vol. 6473, p. 64731G, 2015.

[63] S. Watanabe, T. Takano, K. Jinen, J. Yamamoto, and H. Kawanishi, "Refractive indices of $B_xAl_{1-x}N$ (x= 0-0.012) and $B_yGa_{1-y}N$ (y= 0-0.023) epitaxial layers in ultraviolet region," *Physica Status Solidi (c)*, vol. 0, no. 7, pp. 2691–2694, 2003.

[64] M. Abid, T. Moudakir, G. Orsal, S. Gautier, A. En Naciri, Z. Djebbour, J.-H. Ryou, G. Patriarche, L. Largeau, H. J. Kim, Z. Lochner, K. Pantzas, D. Alamarguy, F. Jomard, R. D. Dupuis, J.-P. Salvestrini, P. L. Voss, and A. Ougazzaden, "Distributed Bragg reflectors based on diluted boron-based BAlN alloys for deep ultraviolet optoelectronic applications," *Applied Physics Letters*, vol. 100, p. 051101, 2012.

[65] Y.kuga, T. Shirai, M. Haruyama, H. Kawanishi, and Y. Suematsu, "Violet and Near-UV Light Emission from $GaN/Al_{0.08}Ga_{0.92}N$ Injection Diode Grown on (0001) 6H-SiC Substrate by Low-Pressure Metal-Organic Vapor Phase Epitaxy," *Japanese Journal of Applied Physics*, vol. 34, pp. 4085–4086, 1995.

[66] A. Y. Polyakov, M. Shin, M. Skowronski, D. W. Greve, R. G. Wilson, A. V. Govorkov, and R. M. Desrosiers, "Growth of GaBN ternary solutions by organometallic vapor phase epitaxy," *Journal of Electronic Materials*, vol. 26, no. 3, pp. 237–242, 1997.

[67] A. Nakajima, Y. Furukawa, H. Yokoya, and H. Yonezu, "Growth of $B_xAl_{1-x}N$ layers using decaborane on SiC substrates," *Journal of Crystal Growth*, vol. 278, pp. 437–442, 2005.

[68] A. Y. Polyakov, M. Shin, W. Qian, M. Skowronski, D. W. Greve, and R. G. Wilson, "Growth of AlBN solid solutions by organometallic vapor-phase epitaxy," *Journal of Applied Physics*, vol. 81, no. 4, pp. 1715–1719, 1997.

[69] M. Shibata, M. Kurimoto, J. Yamamoto, T. Honda, and H. Kawanishi, "GaN/BAlN heterostructure grown on a (0001) 6H-SiC substrate by metalorganic vapor phase epitaxy," *Journal of Crystal Growth*, vol. 189-190, pp. 445–447, 1998.

[70] C. H. Wei, Z. Y. Xie, J. H. Edgar, K. C. Zeng, J. Y. Lin, H. X. Jiang, J. Chaudhuri, C. Ignatiev, and D. N. Braski, "MOCVD growth of GaBN on 6H-SiC (0001) substrates," *Journal of Electronic Materials*, vol. 29, no. 4, pp. 452–456, 2000.

[71] T. Takano, M. Kurimoto, J. Yamamoto, and H. Kawanishi, "Epitaxial growth of high quality BAlGaN quaternary lattice matched to AlN on 6H-SiC substrate by LP-MOVPE for deep-UV emission," *Journal of Crystal Growth*, vol. 237-239, pp. 972–977, 2002.

[72] T. Akasaka and T. Makimoto, "Flow-rate modulation epitaxy of wurtzite AlBN," *Applied Physics Letters*, vol. 88, p. 041902, 2006.

[73] S. Gautier, C. Sartel, S. Ould Saad Hamady, N. Maloufi, J. Martin, F. Jomard, and A. Ougazzaden, "MOVPE growth study of $B_xGa_{(1-x)}N$ on GaN template substrate," *Superlattices and Microstructures*, vol. 40, pp. 233–248, 2006.

[74] A. Ougazzaden, S. Gautier, T. Moudakir, Z. Djebbour, Z. Lochner, S. Choi, H. J. Kim, J.-H. Ryou, R. D. Dupuis, and A. A. Sirenko, "Bandgap bowing in BGaN thin films," *Applied Physics Letters*, vol. 93, p. 083118, 2008.

[75] H. Kawanishi and T. Honda, "Fabrications of BAlGaInN multi-Layer or quantum well structure for blue to UV Light emitter and its applications to optical devices," *Photonics Based on Wavelength Integration and Manipulation*, vol. 2, pp. 19–24, 2005.

[76] J. Edgar, D. Smith, C. Eddy, C. Carosella, and B. Sartwell, "c-Boron-aluminum nitride alloys prepared by ion-beam assisted deposition," *Thin Solid Films*, vol. 298, no. 1-2, pp. 33–38, 1997.

[77] V. K. Gupta, C. C. Wamsley, M. W. Koch, and G. W. Wicks, "Molecular beam epitaxy growth of boron-containing nitrides," *Journal of Vacuum Science & Technology B: Microelectronics and Nanometer Structures*, vol. 17, no. 3, pp. 1246–1248, 1999.

[78] L. Liljeholm, M. Junaid, T. Kubart, J. Birch, L. Hultman, and I. Katardjiev, "Synthesis and characterization of (0001)-textured wurtzite $Al_{1-x}B_xN$ thin films," *Surface and Coatings Technology*, vol. 206, no. 6, pp. 1033–1036, 2011.

[79] J.-H. Song, J.-L. Huang, J. C. Sung, S.-C. Wang, H.-H. Lu, and D.-F. Lii, "Interfacial microstructure evolution of (B, Al)N films grown on diamond substrates," *Thin Solid Films*, vol. 519, no. 13, pp. 4212–4215, 2011.

[80] C. Wei and J. Edgar, "Unstable composition region in the wurtzite $B_{1-x-y}Ga_xAl_yN$ system," *Journal of Crystal Growth*, vol. 208, pp. 179–182, 2000.

[81] T. Akasaka, Y. Kobayashi, and T. Makimoto, "Nonpolar AlBN (1120) and (1100) films grown on SiC substrates," *Applied Physics Letters*, vol. 91, p. 041914, 2007.

[82] A. R. Denton and N. W. Ashcroft, "Vegards law," *Physical Review A*, vol. 43, no. 6, pp. 3161–3164, 1991.

[83] S. Nakamura, "GaN Growth Using GaN Buffer Layer," *Japanese Journal of Applied Physics*, vol. 30, no. Part 2, No. 10A, p. L1705, 1991.

[84] S. R. Lee, A. F. Wright, M. H. Crawford, G. a. Petersen, J. Han, and R. M. Biefeld, "The band-gap bowing of Al_xGa_{1-x} N alloys," *Applied Physics Letters*, vol. 74, no. 22, pp. 3344–3346, 1999.

[85] W. Shan, J. W. Ager, W. Walukiewicz, E. E. Haller, B. D. Little, J. J. Song, M. Schurman, Z. C. Feng, R. A. Stall, and B. Goldenberg, "Near-band-edge photoluminescence emission in $Al_xGa_{1-x}N$ under high pressure," *Applied Physics Letters*, vol. 72, pp. 2274–2276, 1998.

[86] S. Azzi, A. Zaoui, and M. Ferhat, "On the importance of the band gap bowing in Boron-based III¢V ternary alloys," *Solid State Communications*, vol. 144, pp. 245–248, 2007.

[87] I. Vurgaftman, J. R. Meyer, and L. R. Ram-Mohan, "Band parameters for III-V compound semiconductors and their alloys," *Journal of Applied Physics*, vol. 89, no. 11, pp. 5815–5875, 2001.

[88] K. B. Nam, J. Li, M. L. Nakarmi, J. Y. Lin, and H. X. Jiang, "Unique optical properties of AlGaN alloys and related ultraviolet emitters," *Applied Physics Letters*, vol. 84, no. 25, pp. 5264–5266, 2004.

[89] M. Leroux, F. Semond, F. Natali, D. Byrne, F. Cadoret, B. Damilano, A. Dussaigne, N. Grandjean, A. Le Louarn, S. Vézian, and J. Massies, "About some optical properties of $Al_xGa_{1-x}N$ /GaN quantum wells grown by molecular beam epitaxy," *Superlattices and Microstructures*, vol. 36, pp. 659–674, 2004.

[90] H.-Y. Ryu, I.-G. Choi, H.-S. Choi, and J.-I. Shim, "Investigation of light extraction efficiency in AlGaN deep-ultraviolet light-emitting diodes," *Applied Physics Express*, vol. 6, p. 062101, 2013.

[91] T. Kolbe, A. Knauer, C. Chua, Z. Yang, S. Einfeldt, P. Vogt, N. M. Johnson, M. Weyers, and M. Kneissl, "Optical polarization characteristics of ultraviolet (In)(Al)GaN multiple quantum well light emitting diodes," *Applied Physics Letters*, vol. 97, p. 171105, 2010.

[92] M. Leroux, S. Dalmasso, F. Natali, S. Helin, C. Touzi, S. Laügt, M. Passerel, F. Omnes, F. Semond, J. Massies, and P. Gibart, "Optical characterization of $Al_xGa_{1-x}N$ alloys (x<0.7) grown on sapphire or silicon," *Physica Status Solidi (b)*, vol. 234, no. 3, pp. 887–891, 2002.

[93] F. Bernadini, V. Fiorentini, and D. Vanderbilt, "Spontaneous polarization and piezoelectric constants of III-V nitrides," *Physical Revew B*, vol. 56, pp. 10024–10027, 1997.

[94] O. Ambacher, "Growth and applications of Group III-nitrides," *Journal of Physics D: Applied Physics*, vol. 31, pp. 2653–2710, 1998.

[95] H. M. Ng, R. Harel, S. N. G. Chu, and A. Y. Cho, "The effect of built-in electric field in GaN / AlGaN quantum wells with high AlN mole fraction," *Journal of Electronic Materials*, vol. 30, no. 3, pp. 134–137, 2001.

[96] V. Fiorentini, F. Bernardini, F. D. Sala, A. D. Carlo, and P. Lugli, "Effects of macroscopic-polarization built-in electrostatic fields in III-V nitrides multi-quantum-wells," *Physical Revew B*, vol. 60, no. 12, pp. 8849–8858, 1999.

[97] K. Tsubouchi and N. Mikoshib, "Zero-Temperature-Coefficient SAW Devices on A1N Epitaxial Films," *IEEE Transactions on Sonics and Ultrasonics*, vol. SU-32, pp. 634–644, 1985.

[98] A. Barker and M. Ilegems, "Infrared lattice vibrations and free-electron dispersion in GaN," *Physical Revew B*, vol. 7, no. 2, pp. 734–750, 1973.

[99] V. W. L. Chin, T. L. Tansley, and T. Osotchan, "Electron mobilities in gallium, indium and aluminum nitrides," *Journal of Applied Physics*, vol. 75, no. 11, pp. 7365–7372, 1994.

[100] F. Bernardini, V. Fiorentini, and D. Vanderbilt, "Accurate calculation of polarization-related quantities in semiconductors," *Physical Review B*, vol. 63, p. 193201, 2001.

[101] N. Grandjean, B. Damilano, S. Dalmasso, M. Leroux, M. Laügt, and J. Massies, "Built-in electric-field effects in wurtzite AlGaN/GaN quantum wells," *Journal of Applied Physics*, vol. 86, no. 7, pp. 3714–3720, 1999.

[102] "http://en.wikipedia.org/wiki/Quantum-confined_Stark_effect."

[103] G. B. Stringfellow, *Organometallic Vapor-Phase Epitaxy*. Academic Press, 1999.

[104] A. Mircea, A. Ougazzaden, and R. Mellet, "Very uniform epitaxy," *Progress in Crystal Growth and Characterization of Materials*, vol. 19, no. 1-2, pp. 39–49, 1989.

[105] S. Gautier, C. Sartel, S. Ould-Saad, J. Martin, A. Sirenko, and A. Ougazzaden, "GaN materials growth by MOVPE in a new-design reactor using DMHy and NH3," *Journal of Crystal Growth*, vol. 298, pp. 428–432, 2007.

[106] M. A. Moram and M. E. Vickers, "X-ray diffraction of III-nitrides," *Reports on Progress in Physics*, vol. 72, p. 036502, 2009.

[107] "http://en.wikipedia.org/wiki/Secondary_ion_mass_spectrometry."

[108] "http://www.probion.fr/fr/86-accueil/139-physical-description-of-sims-analysis."

[109] "http://en.wikipedia.org/wiki/Scanning_transmission_electron_microscopy."

[110] K. Pantzas, G. Patriarche, D. Troadec, S. Gautier, T. Moudakir, S. Suresh, L. Largeau, O. Mauguin, P. L. Voss, and A. Ougazzaden, "Nanometer-scale, quantitative composition mappings of InGaN layers from a combination of scanning transmission electron microscopy and energy dispersive x-ray spectroscopy," *Nanotechnology*, vol. 23, p. 455707, 2012.

[111] "http://en.wikipedia.org/wiki/Energy-dispersive_X-ray_spectroscopy."

[112] "http://en.wikipedia.org/wiki/Atomic_force_microscopy."

[113] Veeco Instruments Inc., "A Practical Guide to Scanning Probe Microscopy (SPM)," tech. rep., 2005.

[114] "http://en.wikipedia.org/wiki/Scanning_electron_microscope."

[115] "http://en.wikipedia.org/wiki/Cathodoluminescence."

[116] "http://en.wikipedia.org/wiki/Photoluminescence."

[117] "http://en.wikipedia.org/wiki/Fourier_transform_infrared_spectroscopy."

[118] X.-H. Li, Y. O. Wei, S. Wang, H. Xie, T.-T. Kao, M. M. Satter, S.-C. Shen, P. Douglas Yoder, T. Detchprohm, R. D. Dupuis, A. M. Fischer, and F. A. Ponce, "Temperature dependence of the crystalline quality of AlN layer grown on sapphire substrates by metalorganic chemical vapor deposition," *Journal of Crystal Growth*, vol. 414, pp. 76–80, 2015.

[119] X.-H. Li, S. Wang, H. Xie, Y. O. Wei, T.-T. Kao, M. M. Satter, S.-C. Shen, P. Douglas Yoder, T. Detchprohm, R. D. Dupuis, A. M. Fischer, and F. A. Ponce, "Growth of high-quality AlN layers on sapphire substrates at relatively low temperatures by metalorganic chemical vapor deposition," *Physica Status Solidi (b)*, vol. 252, no. 5, pp. 1089–1095, 2015.

[120] Y. L. Tsai, C. L. Wang, P. H. Lin, W. T. Liao, and J. R. Gong, "Observation of compositional pulling phenomenon in $Al_xGa_{1-x}N$ (0.4<x<1.0) films grown on (0001) sapphire substrates," *Applied Physics Letters*, vol. 82, no. 1, pp. 31–33, 2003.

[121] B. Liu, R. Zhang, J. G. Zheng, X. L. Ji, D. Y. Fu, Z. L. Xie, D. J. Chen, P. Chen, R. L. Jiang, and Y. D. Zheng, "Composition pulling effect and strain relief mechanism in AlGaN/AlN distributed Bragg reflectors," *Applied Physics Letters*, vol. 98, p. 261916, 2011.

[122] Z. Chen, Y. Pei, S. Newman, D. Brown, R. Chung, S. Keller, S. P. DenBaars, S. Nakamura, and U. K. Mishra, "Growth of AlGaN/GaN/AlGaN double heterojunction field-effect transistors and the observation of a compositional pulling effect," *Applied Physics Letters*, vol. 94, p. 171117, 2009.

[123] G.B.Stringfellow, "Compositional ordering in semiconductor alloys," *Mater. Res. Soc. Symp. Proc.*, vol. 312, pp. 35–46, 1993.

[124] J. Tersoff, "Stress-driven alloy decomposition during step-flow growth," *Physical Review Letters*, vol. 77, no. 10, pp. 2017–2020, 1996.

[125] P. Venezuela, J. Tersoff, J. Floro, E. Chason, D. Follstaedt, F. Liu, and M. Lagally, "Self-organized growth of alloy superlattices," *Letters to nature*, vol. 397, pp. 678–681, 1999.

[126] B. Reuters, M. Finken, A. Wille, B. Holländer, M. Heuken, H. Kalisch, and A. Vescan, "Relaxation and critical strain for maximum In incorporation in AlInGaN on GaN grown by metal organic vapour phase epitaxy," *Journal of Applied Physics*, vol. 112, p. 093524, 2012.

[127] P. Bogusławski, K. Rapcewicz, and J. Bernholc, "Surface segregation and interface stability of AlN/GaN , GaN/InN , and AlN/InN {0001} epitaxial systems," *Physical Review B*, vol. 61, no. 16, pp. 820–826, 2000.

[128] J. H. van der Merwe, "Crystal interfaces. Part II. Finite overgrowth," *Journal of Applied Physics*, vol. 34, pp. 123–127, 1962.

[129] J. H. Van Der Merwe and W. A. Jesser, "An exactly solvable model for calculating critical misfit and thickness in epitaxial superlattices: Layers of equal elastic constants and thicknesses," *Journal of Applied Physics*, vol. 63, no. 5, pp. 1509–1517, 1988.

[130] J. Matthews and A. Blakeslee, "Defects in epitaxial multilayers I. Misfit dislocations," *Journal of Crystal Growth*, vol. 27, pp. 118–125, 1974.

[131] Hutchinson, J. W. and Z., Suo, "Mixed mode cracking in layered materials," *Advances in Applied Mechanics*, vol. 29, pp. 64–191, 1992.

[132] Z. Wu, K. Nonaka, Y. Kawai, T. Asai, F. a. Ponce, C. Chen, M. Iwaya, S. Kamiyama, H. Amano, and I. Akasaki, "Strain Relaxation Mechanisms in AlGaN Epitaxy on AlN Templates," *Applied Physics Express*, vol. 3, p. 111003, 2010.

[133] Z. Ren, Q. Sun, S.-Y. Kwon, J. Han, K. Davitt, Y. K. Song, a. V. Nurmikko, H.-K. Cho, W. Liu, J. a. Smart, and L. J. Schowalter, "Heteroepitaxy of AlGaN on bulk AlN substrates for deep ultraviolet light emitting diodes," *Applied Physics Letters*, vol. 91, p. 051116, 2007.

[134] J. Tersoff and F. K. LeGoues, "Competing relaxation mechanisms in strained layers," *Physical Review Letters*, vol. 72, no. 22, pp. 3570–3574, 1994.

[135] B. N. Pantha, R. Dahal, M. L. Nakarmi, N. Nepal, J. Li, J. Y. Lin, H. X. Jiang, Q. S. Paduano, and D. Weyburne, "Correlation between optoelectronic and structural properties and epilayer thickness of AlN," *Applied Physics Letters*, vol. 90, p. 241101, 2007.

[136] X. Li, S. Sundaram, Y. El Gmili, F. Genty, S. Bouchoule, G. Patriache, P. Disseix, F. Réveret, J. Leymarie, J.-P. Salvestrini, R. Dupuis, P. Voss, and A. Ougazzaden, "MOVPE grown periodic AlN/BAlN heterostructure with high boron content," *Journal of Crystal Growth*, vol. 414, pp. 119–122, 2015.

[137] J. Kim, Z. Lochner, M.-H. Ji, S. Choi, H. J. Kim, J. S. Kim, R. D. Dupuis, A. M. Fischer, R. Juday, Y. Huang, T. Li, J. Y. Huang, F. a. Ponce, and J.-H. Ryou, "Origins of unintentional incorporation of gallium in InAlN layers during epitaxial growth, part II: Effects of underlying layers and growth chamber conditions," *Journal of Crystal Growth*, vol. 388, pp. 143–149, 2014.

[138] X. Li, S. Sundaram, Y. E. Gmili, T. Moudakir, F. Genty, O. Legrani, R. D. Dupuis, P. L. Voss, J. P. Salvestrini, and A. Ougazzaden, "BAlN thin layers for deep UV applications," *Physica Status Solidi (a)*, vol. 212, no. 4, pp. 745–750, 2015.

[139] X.-H. Li, Y. O. Wei, S. Wang, H. Xie, T.-T. Kao, M. M. Satter, S.-C. Shen, P. Douglas Yoder, T. Detchprohm, R. D. Dupuis, A. M. Fischer, and F. A. Ponce, "Temperature

dependence of the crystalline quality of AlN layer grown on sapphire substrates by metalorganic chemical vapor deposition," *Journal of Crystal Growth*, vol. 414, pp. 76–80, 2015.

[140] X.-H. Li, S. Wang, H. Xie, Y. O. Wei, T.-T. Kao, M. M. Satter, S.-C. Shen, P. Douglas Yoder, T. Detchprohm, R. D. Dupuis, A. M. Fischer, and F. A. Ponce, "Growth of high-quality AlN layers on sapphire substrates at relatively low temperatures by metalorganic chemical vapor deposition," *Physica Status Solidi (b)*, vol. 252, no. 5, pp. 1089–1095, 2015.

[141] S. Chuang and C. Chang, "K·P Method for strained wurtzite semiconductors," *Physical Review B*, vol. 54, no. 4, pp. 2491–2504, 1996.

[142] J. E. Northrup, C. L. Chua, Z. Yang, T. Wunderer, M. Kneissl, N. M. Johnson, and T. Kolbe, "Effect of strain and barrier composition on the polarization of light emission from AlGaN/AlN quantum wells," *Applied Physics Letters*, vol. 100, p. 021101, 2012.

[143] S. Ivanov, D. Nechaev, A. Sitnikova, V. Ratnikov, M. Yagovkina, N. Rzheutskii, E. Lutsenko, and V. Jmerik, "Plasma-assisted molecular beam epitaxy of Al(Ga)N layers and quantum well structures for optically pumped mid-UV lasers on c-Al_2O_3," *Semiconductor Science and Technology*, vol. 29, p. 084008, 2014.

[144] H. Murotani, Y. Yamada, H. Miyake, and K. Hiramatsu, "Silicon concentration dependence of optical polarization in AlGaN epitaxial layers," *Applied Physics Letters*, vol. 98, p. 021910, 2011.

[145] Z. Bryan, I. Bryan, S. Mita, J. Tweedie, Z. Sitar, and R. Collazo, "Strain dependence on polarization properties of AlGaN and AlGaN-based ultraviolet lasers grown on AlN substrates," *Applied Physics Letters*, vol. 106, p. 232101, 2015.

[146] J. Baur, K. Maier, M. Kunzer, U. Kaufmann, and J. Schneider, "Determination of the GaN/AlN band offset via the (-/0) acceptor level of iron," *Applied Physics Letters*, vol. 65, no. 17, pp. 2211–2213, 1994.

[147] M. B. Nardelli, K. Rapcewicz, and J. Bernholc, "Strain effects on the interface properties of nitride semiconductors," *Physical Revew B*, vol. 55, no. 12, p. R7323, 1997.

[148] N. Binggeli, P. Ferrara, and A. Baldereschi, "Band-offset trends in nitride heterojunctions," *Physical Review B*, vol. 63, p. 245306, 2001.

[149] F. Bernardini and V. Fiorentini, "Macroscopic polarization and band offsets at nitride heterojunctions," *Physical Revew B*, vol. 57, p. R9427, 1998.

[150] G. Martin, A. Botchkarev, A. Rockett, and H. Morkoc, "Valence-band discontinuities of wurtzite GaN, AlN, and InN heterojunctions measured by x-ray photoemission spectroscopy," *Applied Physics Letters*, vol. 68, no. 18, pp. 2541–2453, 1996.

[151] J. Hopfield, "Fine structure in the optical absorption edge of anisotropic crystals," *Journal of Physics and Chemistry of Solids*, vol. 15, pp. 97–107, 1960.

[152] X. Li, S. Sundaram, P. Disseix, G. Le Gac, S. Bouchoule, G. Patriarche, F. Réveret, J. Leymarie, Y. E. Gmili, T. Moudakir, F. Genty, J.-P. Salvestrini, R. D. Dupuis, P. L. Voss, and A. Ougazzaden, "AlGaN-based MQWs grown on a thick relaxed AlGaN buffer on AlN templates emitting at 285 nm," *Optical Materials Express*, vol. 5, no. 2, pp. 380–392, 2015.

[153] M. Shiojiri, C. C. Chuo, J. T. Hsu, J. R. Yang, and H. Saijo, "Structure and formation mechanism of V defects in multiple InGaN/GaN quantum well layers," *Journal of Applied Physics*, vol. 99, p. 073505, 2006.

[154] H.-L. Tsai, T.-Y. Wang, J.-R. Yang, C.-C. Chuo, J.-T. Hsu, Z.-C. Feng, and M. Shiojiri, "Observation of V Defects in Multiple InGaN/GaN Quantum Well Layers," *Materials Transactions*, vol. 48, no. 5, pp. 894–898, 2007.

[155] L. C. Le, D. G. Zhao, D. S. Jiang, L. Li, L. L. Wu, P. Chen, Z. S. Liu, Z. C. Li, Y. M. Fan, J. J. Zhu, H. Wang, S. M. Zhang, and H. Yang, "Carriers capturing of V-defect and its effect on leakage current and electroluminescence in InGaN-based light-emitting diodes," *Applied Physics Letters*, vol. 101, p. 252110, 2012.

[156] F. Lin, N. Xiang, P. Chen, S. Y. Chow, and S. J. Chua, "Investigation of the V-pit related morphological and optical properties of InGaNGaN multiple quantum wells," *Journal of Applied Physics*, vol. 103, p. 043508, 2008.

[157] A. M. Armstrong, M. H. Crawford, and D. D. Koleske, "Contribution of deep-level defects to decreasing radiative efficiency of InGaN/GaN quantum wells with increasing emission wavelength," *Applied Physics Express*, vol. 7, p. 032101, 2014.

[158] X. A. Cao, K. Topol, F. Shahedipour-Sandvik, J. Teetsov, P. M. Sandvik, S. E. LeBoeuf, A. Ebong, J. W. Kretchmer, E. B. Stokes, S. Arthur, A. E. Kaloyeros, and D. Walker, "Influence of defects on electrical and optical characteristics of GaN/InGaN-based light-emitting diodes," *Solid State Lighting II, Proceedings of SPIE*, vol. 4776, pp. 105–113, 2002.

[159] S.-R. Jeon, S.-J. Lee, S. H. Jung, S. H. Lee, J. H. Baek, H. Jeong, O. H. Cha, E.-K. Suh, and M. S. Jeong, "Effect of V-shaped defects on structural and optical properties of AlGaN/InGaN multiple quantum wells," *Journal of Physics D: Applied Physics*, vol. 41, p. 132006, 2008.

[160] M. Moseley, A. Allerman, M. Crawford, J. J. Wierer, M. Smith, and L. Biedermann, "Electrical current leakage and open-core threading dislocations in AlGaN-based deep ultraviolet light-emitting diodes," *Journal of Applied Physics*, vol. 116, p. 053104, 2014.

[161] M. Shatalov, W. Sun, R. Jain, A. Lunev, X. Hu, A. Dobrinsky, Y. Bilenko, J. Yang, G. a. Garrett, L. E. Rodak, M. Wraback, M. Shur, and R. Gaska, "High power AlGaN

ultraviolet light emitters," *Semiconductor Science and Technology*, vol. 29, no. 8, p. 084007, 2014.

[162] N. Kamata, A. Z. M. Touhidul Islam, M. Julkarnain, N. Murakoshi, T. Fukuda, and H. Hirayama, "Nonradiative centers in deep-UV AlGaN-based quantum wells revealed by two-wavelength excited photoluminescence," *Physica Status Solidi (b)*, vol. 252, no. 5, pp. 936–939, 2015.

[163] X. Li, G. Le Gac, S. Bouchoule, Y. El Gmili, G. Patriarche, S. Sundaram, P. Disseix, F. Réveret, J. Leymarie, J. Streque, F. Genty, J.-P. Salvestrini, R. Dupuis, X.-H. Li, P. Voss, and A. Ougazzaden, "Structural and optical investigations of AlGaN MQWs grown on a relaxed AlGaN buffer on AlN templates for emission at 280 nm," *Journal of Crystal Growth*, vol. 432, pp. 37–44, 2015.

[164] Z. Liliental-Weber, "Derivation of growth mechanism of nano-defects in GaN from TEM data," *Journal of Electron Microscopy*, vol. 49, no. 2, pp. 339–348, 2000.

[165] Z. Liliental-Weber, Y. Chen, S. Ruvimov, and J. Washburn, "Formation mechanism of nanotubes in GaN," *Physcal Review Letters*, vol. 79, no. 15, pp. 2835–2838, 1997.

[166] M. Leroux, N. Grandjean, B. Beaumont, G. Nataf, F. Semond, J. Massies, and P. Gibart, "Temperature quenching of photoluminescence intensities in undoped and doped GaN," *Journal of Applied Physics*, vol. 86, pp. 3721–3728, 1999.

[167] J. Bai, Q. Wang, and T. Wang, "Greatly enhanced performance of InGaN/GaN nanorod light emitting diodes," *Physica Status Solidi (a)*, vol. 209, no. 3, pp. 477–480, 2012.

[168] P. Dong, J. Yan, Y. Zhang, J. Wang, C. Geng, H. Zheng, X. Wei, Q. Yan, and J. Li, "Optical properties of nanopillar AlGaN/GaN MQWs for ultraviolet light-emitting diodes," *Optics Express*, vol. 22, no. S2, pp. A320–A327, 2014.

[169] M. A. Reshchikov and H. Morko, "Luminescence properties of defects in GaN," *Journal of Applied Physics*, vol. 97, p. 061301, 2005.

[170] A. Y. Polyakov and I.-H. Lee, "Deep traps in GaN-based structures as affecting the performance of GaN devices," *Materials Science and Engineering: R: Reports*, vol. 94, pp. 1–56, 2015.

[171] M. Kneissl, T. Kolbe, C. Chua, V. Kueller, N. Lobo, J. Stellmach, a. Knauer, H. Rodriguez, S. Einfeldt, Z. Yang, N. M. Johnson, and M. Weyers, "Advances in group III-nitride-based deep UV light-emitting diode technology," *Semiconductor Science and Technology*, vol. 26, p. 014036, 2010.

[172] A. V. Tikhonravov, M. K. Trubetskov, A. A. Tikhonravov, and A. Duparré, "Effects of interface roughness on the spectral properties of thin films and multilayers.," *Applied Optics*, vol. 42, no. 25, pp. 5140–5148, 2003.

[173] A. Hafaiedh and N. Bouarissa, "Energy gaps and optical properties for the quaternary $Al_xGa_yIn_{1-x-y}N$ matched to GaN substrate," *Materials Chemistry and Physics*, vol. 115, no. 1, pp. 122–125, 2009.

[174] P. Hervé and L. Vandamme, "General relation between refractive index and energy gap in semiconductors," *Infrared Physics & Technology*, vol. 35, no. 4, pp. 609–615, 1994.

[175] S. Krishnankutty, R. M. Kolbas, M. A. Khan, J. N. Kuznia, J. M. V. Hove, and D. T. Olson, "Photoluminescence Characterization of AIGaN-GaN Pseudomorphic Quantum Wells and Calculation of Strain Induced Bandgap Shifts," *Journal of Electronic Materials*, vol. 21, no. 6, pp. 5–8, 1992.

[176] "http://www.ioffe.ru/SVA/NSM/Semicond/BN/mechanic.html."

[177] "http://accuratus.com/alumni.html."

[178] R. M. Wentzcovitch, K. J. Chang, and M. L. Cohen, "Electronic and structural properties of BN and BP," *Physical Review B*, vol. 34, pp. 1071–1079, 1986.

[179] H. Akamaru, A. Onodera, T. Endo, and O. Mishima, "Pressure dependence of the optical-absorption edge of AlN and graphite-type BN," *Journal of Physics and Chemistry of Solids*, vol. 63, no. 5, pp. 887–894, 2002.

[180] P. Perlin, I. Gorczyca, N. E. Christensen, I. Grzegory, H. Teisseyre, and T. Suski, "Pressure studies of gallium nitride: Crystal growth and fundamental electronic properties," *Physical Review B*, vol. 45, no. 23, pp. 13307–13313, 1992.

[181] S. Kim, I. P. Herman, J. A. Tuchman, K. Doverspike, L. B. Rowland, and D. K. Gaskill, "Photoluminescence from wurtzite GaN under hydrostatic pressure," *Applied Physics Letters*, vol. 67, no. 3, pp. 380–382, 1995.

[182] V. Tasco, I. Tarantini, A. Campa, A. Massaro, T. Stomeo, G. Epifani, A. Passaseo, M. Braccini, M. C. Larciprete, C. Sibilia, and F. a. Bovino, "GaN/AlGaN microcavities for enhancement of non linear optical effects," in *Photonic Crystal Materials and Devices IX, Proc. of SPIE*, vol. 7713, p. 77131Q, 2011.

[183] G. A. Garrett, A. V. Sampath, H. Shen, M. Wraback, W. Sun, M. Shatalov, X. Hu, J. Yang, Y. Bilenko, A. Lunev, M. S. Shur, R. Gaska, J. R. Grandusky, and L. J. Schowalter, "Evaluation of AlGaN-based deep ultraviolet emitter active regions by temperature dependent time-resolved photoluminescence," *Physica Status Solidi (c)*, vol. 7, no. 10, pp. 2390–2393, 2010.

[184] P. Torchio, A. Gatto, M. Alvisi, and N. Kaiser, "High-reflectivity HfO_2/SiO_2 ultraviolet mirrors," *Applied Optics*, vol. 41, no. 16, pp. 3256–3261, 2002.